Application of laser trapping to study the Radio-sensitivity of Chemo treated 4T1 breast cancer cells and the elasticity of human red blood cells in Sickle Cell Anemia and Sickle cell Trait.

By

Endris Mohammed

A dissertation submitted to graduate programs of Addis Ababa University in partial fulfillment of the requirements for the Degree of Doctoral of Philosophy in physics

Addis Ababa University
Addis Ababa, Ethiopia

January, 2020

Addis Ababa University
Graduate Studies

This is to certify that the dissertation prepared by Endris Mohammed, entitled **Application of laser trapping to study the** R**adio-sensitivity of Chemo treated 4T1 breast cancer cells and the elasticity of human red blood cells in Sickle Cell Anemia and Sickle cell Trait** and in fulfillment of the requirements for the degree of doctor of Philosophy (Physics) complies with the regulation of the university and meets the accepted standards with respect to originality and quality

January, 2020

External Examiner:
Dr. Tesfaye Kidane

Internal Examiner:
Prof.Awadhesh K. Rai

Research Supervisor:
Prof D. B. Erenso

Research Supervisor:
Prof. A. V. Gholap

Chair person of the department:
Dr. Teshome Senbeta

Addis Ababa University

Author: **Endris Mohammed**

Title: **Application of laser trapping to study the** Radio**-sensitivity of Chemo treated 4T1 breast cancer cells and the elasticity of human red blood cells in Sickle Cell Anemia and Sickle cell Trait.**

Department: **Physics**

Degree: Ph.D. Convocation 2020

Declaration

I, the undersigned, declare that this Dissertation is my original work and its composition has never been submitted elsewhere for any other award. All sources of materials used for the Dissertation have been duly acknowledged.

Name: Endris Mohammed Signature: ______________. Date: 27-01-2020

This PhD dissertation has been submitted for examination with our approval as a University advisor.

Research Supervisor:______________________________.

Prof D. B. Erenso

Research Supervisor:______________________________

Prof. A. V. Gholap

Acknowledgments

Above all, I thank the Almighty Allah (GOD) for his guidance and giving me the encourage and the strength throughout my study.

I am highly indebted to express my deepest and genuine appreciation to my advisors: Prof. A.V Gholap at Addis Ababa University (AAU) and Prof. D.B Erenso at Middle Tennessee State University (MTSU) for their follow-up, and support.

This work would have not been possible without the sponsorship of MTSU, AAU, and Mizan-Tepi University (MTU). I am grateful to Prof. D.B Erenso who invited me for a three-month research fellowship to use the biomedical optics research facility at the department of Physics and Astronomy at MTSU, USA. I am also very thankful to Dr. Ron Henderson (the department chair) and Dr. Ying Gao at the International Ginseng Institute, Tennessee Center for Botanical Medicine Research, Department of Agriculture at MTSU. From day one, Dr. Henderson had welcomed and provided us all the support we needed to successfully achieve our objectives in such a very short period. I am very grateful to Dr. Gao and her visiting scholar from China, Dr. Li Chen for culturing and treatment of 4T1 breast cancer cells that the project depended upon. I am also very indebted to the generous funding from AAU and MTU that made my three-month fellowship at MTSU and my entire graduate study at AAU be a reality.

During my five years as a graduate student, I have met several people who have made significant impact to achieve the goals I set as a PhD candidate. Among these, my appreciation to Dr. Teshome, Chair of the department of physics and Weyzero Tselate Adinewu, secretary of the department, is the greatest. I would also like to extend my appreciation to science faculty Graduate Program Office Dr. Teleye Feyissa for their coherent and transparency. I thank all my friends for their support in my work.

At last but not least, without the encouragement of my mother, father, sisters and brothers and the loving support of my wife Habiba Mohammed and my children (Ayisha Endris, Abdulwahid Endris and Zubeyir Endris) none of these would have been possible.

List of Contents

List of Figures

LIST OF TABLES

List of Abbreviations

A_{beam}	Area of the beam spot
A_{cell}	Area of single cell
A_{focus}	Area exposed to the laser
P_I	Incident Power
P_T	Transmitted power
T	Ionization period
TIE	Threshold ionization energy
TRD	Threshold radiation dose
%DF	Percentage difference
RBC	Red blood cell
LT	Laser trap
SCT	Sickle cell trait
SCA	Sickle cell anemia
PS	Piezo-driven stage
GAG	Guanine Adenine Guanine
GTG	Guanine Thymine Guanine
Hb	Hemoglobin
Hb F	Fetal hemoglobin
Hb S	Sickled hemoglobin
Hb A	Normal hemoglobin
IARC	International Agency for Research on Cancer
4T1	Breast cancer cell line
GSN	Gold silica nanoshells
PTX	pacilitaxel
TCM	Traditional Chinese Medicines
DMDD	2-Dodecyl-6-methoxycyclohexa-2,5-diene-1,4-dione
ATP	Adenosine tri-phosphate
DOX	doxorubicin
DITSL	DOX/IR-780-loaded temperature-sensitive-liposome
CW	Continuous Wave
ITSL	IR780-loaded temperature-sensitive-liposome
LLLT	Low Level Laser Therapy
SCD	sickle cell disease
HbAA	normal adult
HbFF	normal infant
HbAS	SCT
HbSS	SCA
T2DM	Type 2 diabetes mellitus
DR	diabetic retinopathy
RPMI1640	Roswell Park Memorial Institute 1640 Medium
FBS	fetal bovine serum
MSCC	Meharry Sickle Cell Center
EDTA	Ethylene Diaminet Tracetic Acid

NdYVO4	Neodymium yttrium vanadate laser
PS	Piezo-driven stage
B	magnetic field
E	Electric field
c	Speed of light
D	Electric displacement
w_o	Radius of spot size
q_o	Charge
n_a	Refractive index of the cell
n_b	Refractive index of the medium
R	Radius
r	Displacement
ε_o	permitivity of free space
$\vec{F}_e$	electrostatic force
$\vec{F}_T$	Trapping force
$\vec{F}_d$	Drag force
$\hat{S}_o$	Direction of polarization
w_a	electromagnetic energy before trapping
w_b	electromagnetic energy after trapping
ω	Laser frequency
k	wave vector
$\rho(\vec{r}+\vec{r}',t)$	dencity of charge developed on the cell
$\delta(\vec{r}^{'}-\vec{r})$	derac delta function for displacement
$\delta(t-t_0)$	derac delta function for displacement

Abstract

The study presents a new method that uses laser trapping (LT) technique for measurement of radiation sensitivity of untreated and chemo-treated cancer cells. A human mammary tumor cell line (4T1) treated by herbal extract from traditional Chinese medicines (TCMs) were studied. We used an anti-tumor compound, 2-Dodecyl-6-methoxycyclohexa-2, 5-diene-1,4-dione (DMDD), which was extracted from the root of AverrhoacarambolaL. A control group of 4T1 breast cancer cells and a two hour and a twenty four hour treated (by DMDD compound) groups of 4T1 cells were used in this study. A high power infrared laser at 1064nm is used to trap single and multiple 4T1 cells from the control and treated groups. The absorbed threshold ionization energy (TIE) and threshold radiation dose (TID) were determined and analyzed using descriptive and t-statistics. The relation of the TIE and TRD to the mass of the individual cells were also analyzed for different hours of treatment in comparison with the control group. The results showed both TIE (81.28mJ, 48.82mJ, and 23.76mJ) and TRD (32.62J/μg, 22.42Jμg, and 9.35μg) –decrease with increasing treatment period. On the other hand, as the mass increases the TIE increases but the TRD decreases regardless of treatment by DMDD. Analyses of the TIE and TRD for single vs multiple cells ionizations within each group has also consistently showed this same behavior for both TIE and TRD regardless of the treatment. The underlying factors for these observed relations are explained in terms radio and hypothermia effects resulting from the laser trap and chemo effects resulting from the treatment by the DMDD. The charges developed on untreated, 2-h and 24-h treated cancer cell were $3.28x10^{-17}c$*,* $4.31x10^{-17}c$*, and* $4.93x10^{-17}c$*. The period of ionization, charge, and charge per unit mass increase as the time of DMDD treatment increase. When the cell ejected from the trap the charge decreases as it is away from the trap.*

The elastic property of sickle and sickle cell trait cell were analyzed for 49 red blood cell (RBC) samples from each HbAS and HbSS groups. Laser trapping technique with computer controlled piezo-driven stage (PS) was used to trap and stretch both HbAS and HbSS red blood cells. Laser trapping force was formulated in a cylindrical model. Using this trapping force relative percent difference, stiffness and the ratio of maximum (longitudinal) and minimum (transverse) radius was taken to study the elasticity. The result shows that HbAS have higher elastic property than the HbSS red blood cell samples.

Chapter One

1 Introduction

4T1 is a breast cancer cell line derived from the mammary gland tissue of a mouse BALB/c. In preclinical research, 4T1 cells have been used to study breast cancer metastasis. 4T1 breast cancer cells are known to be highly aggressive in live tissues [1].

Since its discovery in the early 80's by Ashkin [2-3], Laser trapping (LT) technique has become one of the great inventions of the 20th century. In fact, this novel optical technique has recently be recognized by the Nobel Prize in physics in 2018 [3]. LT technique combined with the advancement of high resolution imaging techniques have created a wide range of novel applications in experimental physics and biomedical research that included transporting a gaseous Bose-Einstein condensate [4], elastic properties of the human red blood cells (RBCs) [5-9] and cancer cells [10], protein unfolding and uncoiling of DNA strands [11-14]. The application of LT technique in biomedical research primarily focused on the study of the mechanical properties of micron or submicron size biological systems by creating Pico-Newton magnitude force using single or dual laser trap either directly or indirectly via micron-size dielectric force probes such as silica and polystyrene beads attached to the biological systems using Biotinylation method.

The use of LT techniques in the study of the mechanical properties of the human RBCs is primarily motivated by the significance of the mechanical properties of RBCs for its biological functioning and the associated health crisis resulting from the abnormality of these cells. One of the major health crisis that result from abnormality of the RBCs is sickle cell anemia (SCA). Since its discovery in the western world by James B. Herrick [15] in the year 1910, SCA has been identified as a genetic disease in which a point mutation in the β-globin gene located on chromosome 11 has one original nucleotide, adenine, replaced with thymine. This single nucleotide substitution changes the codon from a GAG to a GTG, resulting in the substitution of the amino acid valine for glutamic acid at the sixth position of the β-globin chain producing the sickle hemoglobin (Hb S) [16-17]. This genetic mutation produces two distinct genotypes; heterozygotes (AS) resulting in sickle cell trait (SCT) and homozygotes (SS) resulting in SCA. In SCA, the normally round red blood cells (RBCs), change their shape and deformability under deoxygenating conditions which occlude the blood vessels in the microcirculation [18]. As a result, patients with SCA suffer with acute, painful vaso-occlusive crises that could lead to a central nervous system vasculopathy causing impaired intellectual development and, in some patients, devastating strokes [29-20]. Acute vaso-occlusive episodes cause tissue ischemia and excruciating pain, while the resulting chronic multi-organ damage leads to disability and early death [21]. These symptoms do not appear until after six months of age when the γ−globin gene expression has primarily switched to βS-globin gene expression resulting in the conversion from predominantly fetal hemoglobin (Hb F) to sickle hemoglobin (Hb S) instead of to normal adult hemoglobin (Hb A) [22].

Beside the common biomedical application of LT technique to study the mechanical properties of the human RBCs, recently, it has been demonstrated that LT technique can be a promising a more accurate optical tool in Radiotherapy to measure ionization radiation dose and charge at a single cell level [23-25].

Recent studies have shown that LT can also be used as a technique for measuring ionization radiation dose at a single cell level [23-25]. That could have a potential application in the treatment of cancer in radiotherapy. Cancer is one of the leading causes of death in both developing and developed nations in the world. According to the International Agency for Research on Cancer (IARC) 2018 report, there are nearly 2.1 million new cases and 0.5 million deaths of breast cancer worldwide [26-27] annually. As the main focus of this dissertation is on breast cancer, we narrow our focus on this particular type of cancer that predominantly affecting woman. Although breast cancer ranks second, behind lung cancer, in the number of new cancer cases (12%), it has a relatively low death rate (7%), ranking fifth next to liver cancer. This higher survival rate might be due all cancer diagnosis among women more than 40% at the age 40> year and also might be credited to the advancement of traditional therapies such as radiotherapy [28-29] chemotherapy [30-33], surgery [34] and to the development of relatively newer therapies such as hypothermia and hyperthermia that uses nanotechnology [35-38] and immunotherapy [39].

Radiotherapy (RT) is one of the effective tools used for different malignant tumors. It is used to kill all the cancer cells in a tumor with a radiation energy that is enough to overcome the electron binding energy in an atom or a molecule. In RT when such radiation energy to treat a patient, it can cause unintended damage to the normal cells surrounding the tumor. Therefore, the goal of RT must then be to maximize the radiation damage to the cancer cells with no or minimized compromise to the integrity of the normal cells. It is well known that a combined modality treatment, such as radiation and chemo therapies is better than RT alone as such treatment enhances death of tumor cells through an inhibition of DNA repair processes [33]. Some chemotherapeutic drugs can make tumor cell clonogens to be more susceptible to ionization energy so that a reduced radiation dose is needed to kill the tumor cells. Cisplatinum and taxanes are the standard chemotherapeutic agents that have been used for such improved therapeutic outcomes in radiation and chemo combined modalities. However, using these agents in radiation and chemo combined modalities limits the radiation dose as these agents are commonly associated with considerable toxicity to normal tissues [33]. Other recently developed combined modalities of treatment involve hypothermia, hyperthermia, and biocompatible nanoparticles. Studies in 4T1 breast cancer cells in mice have shown hypothermia and hypoperfusion effects induced by pacilitaxel (PTX) that maintain reduced body temperature may prevent tumor relapse or metastasis after chemotherapy [36]. It has also been shown that biocompatible nanoparticles, such as gold silica nanoshells (GSNs) designed to absorb light in the infrared which has a high tissue transparency, have been used to treat prostate cancer [38]. Particles such as GSNs have the ability to absorb the infrared light and to generate heat which induces highly localized hyperthermia, a modality shown to be highly effective for photothermal cancer therapy. Thus, strategies for combined modalities of cancer treatment that utilize radiotherapy, chemo, and possibly hyperthermia effects could provide a new approach for better efficacy of such treatments. Some recent studies have shown that Traditional Chinese Medicines (TCMs) used to treat various types of cancer carry antitumor agents that increase the radio-sensitivity of tumor cells [40-46] and protection against radiation induced damage in normal tissues [47-48]. We have access to the resource of over 100 species of TCM that have antitumor, antioxidant, or immune modulating agents that have traditional use. Testing the radio-sensitivity of some of these compounds is significantly important for screening of natural bioactive components that could be used as radio-sensitizer or radio-protector in developing effective drugs for chemo-radiotherapy. It is well established that commonly used radio-therapeutic drugs influence tumor outcome through reactive oxygen species (ROS) modulation. Testing how these compounds affect ROS generation in cancer and normal cells will cast light on the mechanism of their function in radiotherapy.

The biomedical application of LT technique to study the radio-sensitivity of cancer cells treated with antitumor agents extracted from TCM and the elasticity of human RBCs from SCT and SCA patients is the objective of this study. The study is divided into two parts. In the first part, the study focuses on the radio sensitivity of 4T1 breast carcinoma cells treated by antitumor agents, 2-Dodecyl-6-methoxycyclohexa-2,5-diene-1,4-dione (DMDD), which was extracted from the root of *Averrhoacarambola*L. *AverrhoacarambolaL* known as Star-fruit plant used for nutritional, medicinal and toxicology. This plant used for preparation of juice, pickles and salads. In Brazil, china, India and Taiwan used as fever, sore throat, cough, asthma, chronic headache, and skin inflammations (Narmataa Muthu 2016). The radiosensitivity measurement is conducted by singly ionizing 4T1 cells using infrared LT at high power. In the second part, we studied the difference in elasticity of RBCs from two blood samples drawn from SCT and SCA patients. The elasticity is measured by exerting a oppositely directed drag and trap forces. For the trap force, we used same infrared LT but at a low power, that has minimal effect in compromising the integrity of the cells.

1.1 Hypothesis

1.1.1 Part I

We form three groups of 4T1 breast carcinoma cells. The second and the third groups are made up from 4T1 cells treated by the antitumor agent 2-Dodecyl-6-methoxycyclohexa-2,5-diene-1,4-dione (DMDD) for shorter and longer durations, respectively. The first group is a control group, which consists of untreated 4T1 cells. Statistically significant numbers of 4T1 cells, from each of these groups, are single trapped and ionized. The threshold ionization energy (TIE), the threshold radiation dose (TRD), and the charge for each cells is determined. We hypothesize that:

1. The average TIE and the average TRD are different for the three groups.

2. The radiosensitivity of the treated groups is higher and therefore the average TIE and TRD for the second and third group should be less than the control group.
3. The radiosensitivity of the group treated for longer duration is higher than the group treated for shorter duration and therefore the average TIE and TRD for the third group should be less than the second group.

1.1.2 Part II

We have two types of RBCs which are SCT and SCA. SCT is one sickle cell RBC gene (HbAS) and SCA two sickle cell RBC genes (HbSS).

1. The elastic property of SCT should be higher than the SCA.

1.2 General objectives

Measuring the radio sensitivity of chemo treated 4T1 cancer cell and elasticity property of the SCT and SCA red blood cells using laser trapping technique.

1.2.1 Part I specific objectives

a) To study the effect of DMDD treatment using LT single cell ionization.

b) To measure the charge developed on single cell ionization using Newtonian mechanics.

c) To study the effect of electro-mechanical interaction on radiation dose in multi cell ionization.

1.2.2 Part II specific objectives

a) To study the elastic property of RBCs from blood samples drawn from SCT and SCA patients.

b) To determine the stiffness of these cells by creating reversible elastic deformation using low power LT and drag force.

c) To develop a theoretical model in cylindrical to determine the trapping force.

d) To compare and contrast the stiffness of the RBCs from the SCT and SCA.

1.3 Outline of the thesis

In chapter 2, we explain the background of cell biology and its electrical properties with or without an external electric field. In chapter 3, we describe the experimental methods for cell culturing and treatment, experimental setup, materials used, mechanism of cell membrane breakdown. In chapter 4, the single cell ionization, radiation dose energy density and the hypothesis testing are described and also multi cell ionization and radiation dose for two, three, four and five cells are analyzed and discussed. Single 4T1 cancer cell dynamics is also discussed in two types of model in this chapter. Chapter 5 will be devoted to the second part of the study which is the elastic property of RBCs in SCA and SCT. Finally, we conclude with the summary and the major outcomes of the study in chapter 6.

Chapter Two

2 General back ground and Literature review

2.1 General back ground

The content of this chapter deals with the interaction of near infrared laser with biological cells and the effect of electric field on them. A cell is the basic unit of life. Human cells are surrounded by a cell membrane, which separates the intracellular compartment or cytoplasm from the extracellular medium.

2.1.1 Normal cell

In our body cells are being born; grow, divide and being destroyed to maintain a healthy balance called homeostasis [49]. Normal cell stops proliferating when enough cells are present. Normal cells carry characteristics that are essential for normal body functions since the DNA and RNA have normal function [50]. For example, if cells are being produced to repair an endured body, new cells are no longer divide when enough cells are produced to fill the space. Normal cells are constantly subject to signals that dictate whether the cell should divide, differentiate into another cell or die. Normal cells have predetermined structure and they perform various functions such as delivering nutrients like amino acids, carbohydrates, fats, vitamins, and minerals [50]. They have large cytoplasm, single nucleus and single nucleolus. Each cell matures and performs a particular function, they have not the ability to influence anything, have lower mutations and genetic changes, operate at a normal metabolic level and reproduce themselves at a regulated pace.

2.1.2 Cancer cells

Cancer can be defined as a disease in which a group of abnormal cells grow uncontrollably by disregarding the normal rules of cell division. Cancer is a multi-gene, multi-step disease originating from a single abnormal cell with an altered DNA sequence (mutation). Cancer cells develop a degree of autonomy from these signals, resulting in uncontrolled growth and proliferation [51].

Breast cancer like other cancer cells produced and spread without control. Breast cancers can start from different parts of the breast. Most breast cancers start in the ducts that carry milk to the nipple (ductal cancers) [52]. Some start in the glands that make breast milk (lobular cancers). Breast cancer can spread when the cancer cells get into the blood or lymph system carried to other parts of the body. The lymph system is a network of lymph vessels which carry lymph fluid away from the breast. Lymph vessels found throughout the body that connects lymph nodes [52]. The clear fluid inside the lymph vessels is known as lymph that contains tissue by-products and waste material, as well as immune system cells. In the case of breast cancer, cancer cells can enter those lymph vessels and start to grow in lymph nodes. Most of the lymph vessels of the breast drain into lymph nodes under the arm, lymph nodes around the collar bone and Lymph nodes inside the chest near the breast bone [53]

2.1.3 Cell Membrane

Cells are separated from the external environment by a thin, fragile structure called the plasma membrane that is only 5 to 10 nm. Membranes are complex structures composed of lipids, proteins, and carbohydrates [54].

The intra and extracellular compartments are mostly aqueous saline solutions which are body water, covers 45-75 % of the total body weight. About two thirds of body water corresponds to cellular water (cytosol), which is the aqueous solution in the cytoplasm. The remaining 30 % of body water correspond to extracellular fluid, which is further divided into interstitial fluid and plasma [55]. The interstitial fluid bathes all cells and serves as an interface between blood and cells necessary to carry out nutrients and waste materials interchange. Plasma in contrast corresponds to the liquid content of blood. The saline content of these solutions is specified by the presence of inorganic salts and charged ions, the most important of which are sodium (Na^+), potassium (K^+), chloride (Cl^-) and calcium (Ca^{2+}) (56). Membrane lipids are amphipathic that contain both hydrophobic and hydrophilic regions. The hydrophilic (polar) region is their globular head and the hydrophobic (non-polar) regions are their fatty acid tails [56]. The membrane lipids are organized into a continuous bi-layer (Fig.2.2**)** in which the hydrophobic regions of the phospholipids are shielded from the aqueous environment, while the hydrophilic regions are immersed in water. Proteins are found inserted into this lipid bi-layer and are classified into integral proteins and peripheral proteins.

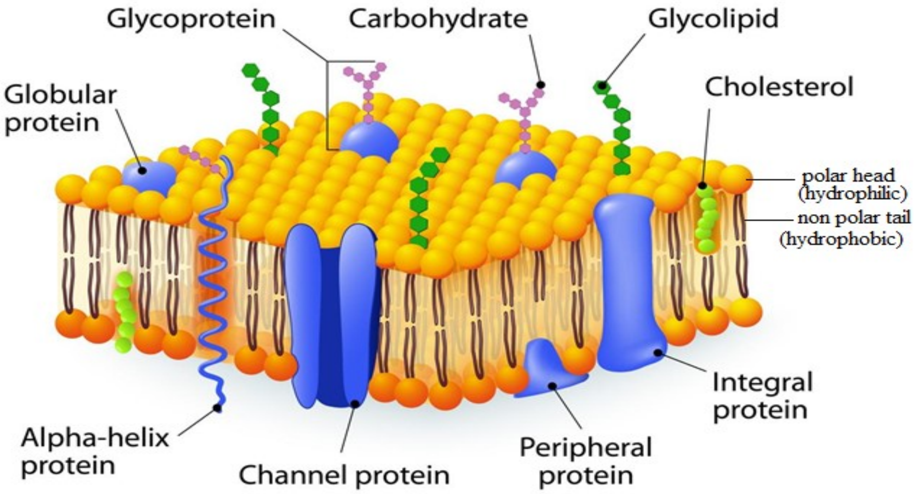

Figure 2.1 Mosaic model of membrane structure and lipid bi-layer [57].

Integral proteins are anchored to membranes through a direct interaction with the lipid bi-layer. Some of them span the entire thickness of the membrane, often traversing the membrane several times [58]. Others are located more on the outside or inside of the membrane. Integral proteins are amphipathic which consists of two hydrophilic ends separated by an intervening hydrophobic region that traverses the hydrophobic core of the bi-layer. The hydrophilic ends of the integral protein are found outside the membrane on both sides of external or internal surface. Integral proteins serve as channels which permit the passage of selected ions through the membrane [59].

Peripheral proteins do not interact directly with the phospholipids in the bi-layer. They are associated with integral proteins via electrostatic interactions. They are located on both surfaces of the membrane. Peripheral proteins serve as cell adhesion molecules that anchor cells to neighboring cells and to the basal lamina [58].

2.1.4 Membrane transport

There are two types of membrane transport proteins: (i) carrier proteins which carry specific molecules across the membrane. (ii) Channel proteins, which form a narrow pore through which ions can pass. Channel proteins carry out passive transport**,** in which ions travel spontaneously down their gradients. Some carrier proteins mediate passive transport, while others can be coupled to a source of energy Adenosine tri-phosphate (ATP) to carry out active transport [60]. Active transport in which a molecule is transported against its concentration gradient to maintain concentration gradient across the membrane which helps to balance the osmotic pressure on either side of the membrane [61]. Active transport uses metabolic energy to transport molecule across the membrane. Carrier protein binds with ATP, and uses the energy of ATP to pump ions across the cell membrane in opposite directions and transporting large molecule such as sugar and fat in and out of the cells [62].

The interior plasma membrane is negatively charged relatively to the exterior part of the cell. This membrane potential determines the movement of charged particles. Potassium ion (K^+) is attracted Cl^- and force out of the cell by the negatively charged interior part of the membrane [63].

The membrane permeability to a substance depends on the molecule's size, lipid solubility, and electrical charge. Gases such as oxygen (O_2), carbon dioxide (CO_2), and nitrogen (N_2) and hydrophobic molecules such as steroid hormones and weak organic acids and bases readily diffuse through the cell membrane. Small uncharged polar molecules like water and urea can diffuse across the lipid bi-layer. Charged particles, whether large (amino acids) or small (Na^+, K^+, Cl^- and Ca^{2+}ions), cannot diffuse across the lipid bi-layer. Ions cross the membranes, often in large amounts, through membrane channels [63].

2.1.5 Membrane potential

Under normal physiological conditions without exposing to the external electric field the cell plasma membrane subject to resting transmembrane voltage (electric potential difference) due to a system of ion pumps and channels [64]. For a cell at rest, the balance between the diffusion and electric force leads to an unbalance in electrical charge between the intra- and the extracellular media. This leads the membrane in a potential difference which is known as membrane potential.

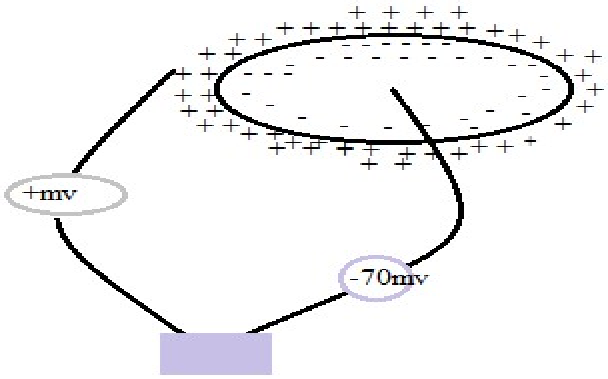

Figure 2.2 Rest potential: Intra and extra cellular potential of a cell under normal conditions [65].

Most biological cells resting potentials range between -35mV and -90 mV [65]. The negative sign is a convention used to indicate that the intracellular medium is negatively charged. Such a negative charge is the consequence of the activation at rest of much more chloride (negative) ion pumps than sodium or calcium (positive) ones [66]. As the membrane potential becomes less negative, a cell is said to be depolarized. In contrast, as the membrane potential becomes more negative a cell is said to be Hyperpolarized [65]. The changes in the value of the resting potential due to depolarization caused by variations in ions concentrations but also due to changes in the surface charge at the cell membrane [67] are responsible for the activation of so-called voltage-gated ion channels. The resulting variations in intracellular ion concentrations cause membrane polarization and channels closure. The temporary flow of ions down their concentration gradients generates the action potentials and cause variations in signaling transduction pathways

[68]. Such a variation is especially important in the case of Ca^{2+}, for which variations in the intracellular ion concentration modify cellular processes such as migration, proliferation, cell attachment, necrosis and apoptosis [69].

2.1.6 Electromagnetic interaction and Electrical properties of cells

Maxwell's equations predict the propagation of electromagnetic wave that carries energy. Energy can be transferred to objects placed in their path with the total energy density, u, carried by an electromagnetic wave is,

$$\mathbf{u} = \frac{1}{2} \in \mathbf{E}^2 + \frac{1}{2\mu}\mathbf{B}^2 \qquad 2.2.1$$

There are different types of electromagnetic wave that differs only by their frequency or wave length.

All materials contain ions and electrons experience Lorentz force when exposed to electromagnetic fields. In dielectrics, electrons are not free which is bound to nuclei. However, those bound electrons can still react to external fields, and induce microscopic current. In an oscillating field, the effective permittivity becomes frequency dependent, and electromagnetic waves in dielectrics are strongly dispersive in contrast to waves in free space.

The propagation of light in the tissue is governed by reflection, scattering, absorption and fluorescence. When light strikes the surface of a material, portion of light reflected from the interface due to the discontinuity in the real index of refraction and the rest will be transmitted into the material. The fraction of the incident power that is reflected from the surface depends on the polarization, angle of incidence of the light as well as the index of refraction of the medium (n_1) and the material (n) [70].

Most part of the laser energy penetrates into biological tissue. The penetration of laser light in biological tissue depends on optical properties of biological tissue, such as index of refraction, scattering and anisotropic factor, and also the absorption of laser light in tissue. These optical properties determine the mechanism of laser tissue interaction and the effect of these properties in the penetration of laser light.

The actions of the laser on the interaction of the tissue are categorized by the wave length of laser light. Lasers which are frequently applied in medicine are between x-ray and infrared (IR) wavelength. The molecular absorption of light depends on its wave length. These absorptions are mainly due to the presence of endogenous molecules that absorb heavily near 200nm such as DNA, genetic material and protein. The mitochondria absorbs 630nm wave length, the oxygen consumption is activate by 365nm light [70-71].

Most biological tissues are classified by strong optical scattering in 400-1100nm region. The absorption and scattering of light in tissue are both much higher in the blue region of the spectrum than the red, because in principle tissue chromophores (hemoglobin and melanin) have high absorption bands at shorter wave-lengths, tissue scattering of light is higher at shorter wavelengths, and furthermore water strongly absorbs infrared light at wavelengths greater than 1100-nm.

Chromophores are biological molecules responsible for UV and visible light absorption within tissue. Most organic molecules are strong absorption in this region, and very weak penetration. In the visible (blue, green and yellow), absorption is principally due to hemoglobin and melanin. Red and near infrared (600 to 1200 nm) wavelengths are weakly absorbed and penetrate deeply into the tissue (this penetration is, however, limited by optical scattering). Water is the absorber inside the tissue for light intensity in the infrared region [72].

Near-infrared radiation (NIR) ranges between 750 and 2,500 nm. NIR radiation exerts multiple effects on mammalian cells. NIR irradiation induces DNA double-strand breaks and apoptosis of cancer cells. Irradiation of pancreatic cancer cells using a 915-nm laser light significantly induces caspase-3 activation and apoptosis. In addition, the combination of gemcitabine treatment and a 915-nm laser synergistically increased the number of apoptotic cells which indicate the use of infrared irradiation and chemotherapy may be a possible therapy for the treatment of cancer [73].

2.1.7 Electroporation

When strong external electric field creates sufficiently strong polarization the cell membrane can be destabilized and transmembrane voltage induced. This induced voltage superimposed to the resting transmembrane potential makes structural change involving rearrangement of the phosphor-lipid bi-layer [74-76]. The membrane rearrangement induces formation of aqueous pores which lead to a very significant increase the membrane permeability. Poration increases the conductivity of the membrane and its permeability to water-soluble molecules, otherwise membrane transport mechanism would be deprived [77-78]. If the laser light switches of, the membrane can return to its initial state. The phenomenon is known as reversible dielectric breakdown or electroporation and also said to be electro permeabilization [79]. The main thing electroporation is to induce the transmembrane voltage generated by external electric field due to the difference of the electrical property of the membrane and the external medium. Nevertheless, if the exposure to electric field is too long and the strength of the electric field is too high, the membrane does rupture and not reseal, the breakdown will be irreversible [80-81]. .

2.1.8 Sickle cell Anemia and Sickle cell Trait blood cells

A person with sickle cell trait (SCT) has A and S gene and can pass either HbA or HbS to a child. Sickle cell hemoglobin genes from sickle cell trait and normal parents have 50% chance to give birth to sickle cell trait offspring as shown in Figure 2.3 (b). If both parents have sickle cell trait, they can pass sickle cell gene to the offspring with 25% SCA, 50% SCT or 25% normal chances as shown in Figure 2.3 (a). Two SCA (SCD) parents always pass S genes from the normal and SCA parent all the offspring are SCT.

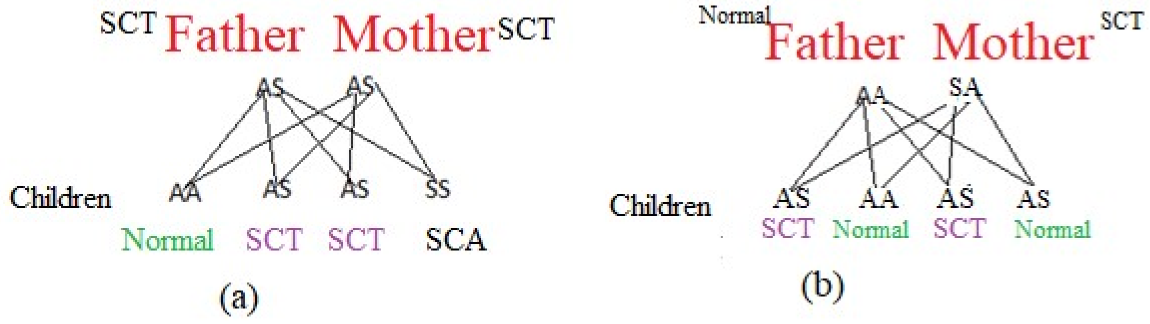

Figure 2.3 Sickle-cell disease is inherited from the recessive pattern.

People with SCT usually do not have any of the symptoms of sickle cell anemia (SCA) and live a normal life. In SCA, the red blood cells become hard and sticky and look like a C-shaped farm tool called a sickle. The sickle cells die early, which causes a constant shortage of red blood cells. Also, when they travel through small blood vessels, they get stuck and clog the blood flow. These can cause pain and other serious problems. It is inherited when a child receives two sickle cell genes from both parents. A person with SCA can pass the disease or SCT on to his or her children.

The disorders of RBCs such as sickle cell anemia (SCA) drastically change their shape and elastic deformability in the micro circulation [82]. The Deformation and orientation of red blood cells are governed by the cellular rheological properties, such as internal viscosity and cytoskeleton elasticity. Rheology is altered genetically by diseases, parasitic invasion or by change in microenvironment [83]. Erythrocytes referred to the red blood cells (RBC), are made up of hemoglobin iron containing molecule. The biconcave discocyte RBC has a flexible membrane with a high surface-to-volume ratio that facilitates large reverse elastic deformation of the RBC as it repeatedly passes through small capillaries during microcirculation. Pathological conditions affecting RBCs can lead to significant alterations to the discocyte shape. This genetically disorders of RBCs such as sickle cell anemia (SCA) drastically change their shape and elastic deformability in the microcirculation [82]. Hemoglobin (Hb) is contained in red blood cells and it is composed of heme which contains iron and globin made up of protein, referred to us alpha (α) and non-alpha such as beta (β), gamma (γ) and delta (δ) chain. HbA ($\alpha 2; \beta 2$) is normal adult hemoglobin that is chain of alpha ($\alpha 2$) and beta ($\beta 2$) (82). Sickle cell disease is a genetically inherited abnormality of hemoglobin in which amino acid replaces glutamine at the sixth position on the beta chains of the hemoglobin molecule [84-85]. This hemoglobin is termed Hemoglobin S (usually written HbS). Two types of sickle cell illness are described depending on the genetic make-up. Everyone has 2 genes responsible for hemoglobin synthesis. A person who has sickle cell anemia, both their hemoglobin is composed of HbS and forms homozygotes (HbSS) but sickle cell trait person whose hemoglobin is formed from one HbA and HbS genes and which can be written as HbAS (heterozygotes [86].

2.1.9 Laser Trapping Technique

James Maxwell proposed that light can exert force on matter by scattering, absorption and emission of light and this force was demonstrated experimentally by Ashkin in 1986, after the invention of laser. The study of the interaction between light and matter has been extremely prolific, leading to the invention of serendipitous techniques that have had a profound impact in many different fields [87]. The optical trap was created using gradient force radiation pressure from a single laser beam [88]. The novel method would lead to an entirely new technique for manipulating microscopic and sub-microscopic particles and individual atoms. Due to their ability to precisely manipulate microscopic particles, laser tweezers lend themselves to a wide array of different applications in experimental physics, biophysics, experimental statistical physics and nanotechnology [88]. Optical traps use light to manipulate microscopic objects as small as 10 nm using the radiation pressure from a focused laser beam. In addition, measurement of the light deflection yields information about the position of the object in the laser focus. Potential energy well in which the particle is trapped can be well characterized by measuring the force that is on the order of Pico-Newton. These two abilities, manipulation and force measurement, can be used to accomplish many novel procedures.

The measurement of the force in Pico-Newton and nanometer ranges and the distance accessible to optical traps make them particularly useful for studying biological systems [89]. Optical forces have been used to investigate structural properties of biological polymers such as DNA, molecular motors, membrane and whole cells [90]. Micro-rheological properties of these objects can be probed through the application of forces either to the object itself, or to a small dielectric sphere, or bead, to which the object is attached [91]. .

The gradient force is attractive when the refractive index of the particle is greater than the surrounding medium. This force pulls dielectric particle to the center of the trap with the strength proportional to applied electric field. The gradient force pushes the particle if the refractive index of the particle is less than that of the medium.

The regimes of optical trapping are the ray optics ($R>>\lambda$) and Rayleigh regime ($R<<\lambda$). Ray optics regime can only describe the limiting regime of particles that are much large compared to the wavelength of the light field ($R>>\lambda$). And the Rayleigh regime is used when the particle is very small compared to the wave length of light ($R<<\lambda$) [92].

The optical rays have a different direction after the interaction; part of their photon momentum (h/λ) is transferred to the object. For a focused Gaussian beam, the net optical force is directed such that it counteracts a displacement of the bead from its equilibrium position in the center of the trapping beam [93].

2.2 Review literature

2.2.1 NIR laser irradiation of cancer cells and chemotherapy

In the previous study carried out in middle Tennessee state University on 2-dodecyl-6-methoxycyclohexa-2,5-diene- 1,4-dione (DMDD) which inhibited the growth of human breast cancer cells with little toxicity. The toxicity and efficacy of DMDD were also, investigated to treat metastatic breast tumors using an in vivo mouse model of the 4T1 mammary carcinoma. DMDD caused no observable toxicity and significantly extended the survival of 4T1 tumor-bearing mice. DMDD effectively inhibited the growth of 4T1 cells in vitro, and suppressed the growth and metastasis of mammary tumor in vivo. DMDD inhibits cytokine production in the tumor cells in mice, which leads to deactivation of NF-κB (nuclear factor kappa-light-chain-enhancer of activated B cells) pathway, and consequently inhibits the expression of many anti-apoptosis and metastasis-promoting genes, such as Bcl-2 and MMPs. Collectively, the results demonstrate the potential of DMDD as a safe and effective antitumor agent in the treatment of late-stage breast cancer [94].

In in vitro study, five kinds of cultured cancer cell lines (MCF7 breast cancer, HeLa uterine cervical cancer, NUGC-4 gastric cancer, B16F0 melanoma, and MDA-MB435 melanoma) were irradiated using the infrared irradiation, and then the cell proliferation activity was evaluated by 3-(4,5-dimethylthiazol-2-yl)-5-(3-carboxymethoxyphenyl)-2-(4-sulfophenyl)-2H-tetrazolium

(MTS) assay. The proliferation of all cancer cell lines was significantly suppressed by infrared laser irradiation.

Using high power NIR laser (0.8W/cm^2) induced photo-thermal therapy (PTT) through near-infrared agents has demonstrated the great potential in solid tumor ablation. However, the non uniform heat distribution over tumors from PTT makes it insufficient to kill all tumor cells, resulting in tumor recurrence and inferior outcomes. To improve the tumor treatment efficacy, it is highly desirable to develop the combinational treatment of PTT with other modalities, especially with chemotherapeutic agents. It was reported that a smart DOX/IR-780-loaded temperature-sensitive-liposome (DITSL) which can achieve NIR-laser-controlled drug release for chemo-photo-thermal synergistic tumor therapy. In this system, the liposoluble IR-780 was incorporated into the temperature sensitive lipid bi-layer and the soluble chemotherapeutic doxorubicin (DOX) was encapsulated in the hydrophilic core. The resulting DITSL is proved to be physiologically stable and can provide a fast and laser irradiation-controllable DOX release in the PBS and cellular conditions. This research further employed nanoparticle for tumor treatment, demonstrating significantly higher tumor inhibition efficacy than that of DOX-loaded temperature-sensitive-liposome (DTSL) or IR780-loaded temperature-sensitive-liposome (ITSL) in the in vitro cells and in vivo animals [95].

B16F10 cells were irradiated a total of three times (once a day for three consecutive days) in a 96 well culture plate for the MTT method and in a 12 well plate for Trypan blue and cytometric assays. Irradiation was performed with a 660 nm, 50 mW Continuous Wave (CW) laser, beam spot size 2 mm^2, irradiance 2.5 W/cm^2. The seeded wells were spaced 5 cm apart in all directions and a thin aluminum sheet was placed halfway (2.5 cm) between them to prevent unintentional light scattering between the wells. The wells were randomly divided into a control group which received no irradiation, and a treatment group which received an LLLT dose of 150 J/cm^2 with an irradiance of 2.5 W/cm^2 for 60 seconds (3J), while a second group received sessions with an LLLT dose of 1050 J/cm^2 with an irradiance of 2.5 W/cm^2 for 420 seconds (21J). Total energy delivered after all three sessions was 9J and 63J respectively in the irradiated groups. The Trypan Blue dye and MTT colorimetric exclusion test showed no statistical differences in proliferation or cell death numbers among irradiated groups and control group in the different times analyzed. Cell cycle analysis in B16F10 cells showed no statistically significant differences in the cell numbers at 24 h, 48 h and 72 h among irradiated groups and control group. There was statistically a significant difference ($p < 0.05$) in hypodiploid cells (possible cell death) at 72 h between the irradiated and control groups (8.48 ± 1.40% and 4.26 ± 0.60%). The increase in apoptosis was most prominent in the low dose 150 J/cm^2 groups [96].

Proliferation of all the cancer cell lines was significantly suppressed by infrared irradiation. Total infrared output appeared to be correlated with cell survival. Increased temperature during infrared irradiation appeared not to play a role in cell survival. The maximum temperature elevation in the wells after each shot in the 20 and 40 J⁄cm^2 culture was 3.8 ^{o}C and 6.9 ^{o}C, respectively [97].

The study no BT20 breast carcinoma cells cultured and harvested and a total of 50 cells, was trapped and ionized by a high intensity infrared laser at 1064 nm at single cell level. The threshold radiation dose and the resultant charge from the ionization for each cell were determined. With the laser trap serving as a radiation source, the cell underwent dielectric breakdown of the membrane. When this process occurs, the cell becomes highly charged and its dielectric susceptibility changes. The charge creates an increasing electrostatic force while the changing dielectric susceptibility diminishes the strength of the trapping force [23]. Hemoglobin

(Hb) of normal (HbAA) and trait (HbAC) cells were identified by the amount of ionization energy and the charge developed using laser trapping technique. RBCs from the blood sample with HbC have higher ionization energy and charge than those RBCs from a normal blood sample HbA [24].

2.2.2 Elastic property of RBC

A number of explorations carried out on the deformability of sickle cell red blood cells. Such investigations were studied elasticity of sickle cell disease (SCD) by comparing with the normal RBC.

Sickle cell patients were divided into two groups depending on whether they were receiving Hydroxyurea (HU) (39 patients) or not (43 patients). They were matched with 50 healthy individuals (control) regarding age and gender. The deformability of HU group was better and closure to the healthy red blood cells. Such LT techniques with optimal power are effective to study the RBC characteristics and deformability [98]. One study shows the elastic property of sickle cell trait (SCT) and sickle cell anemia (SCA), in SCA, the red blood cells (RBCs) fail to change its shape and deformability normally under deoxygenating conditions resulting in occluding the blood vessels in the microcirculation. By manipulating the RBCs using LT studies have been made on the mechanical properties differences of RBCs with different types of Hemoglobin [SCT (HbAS), SCA (HbSS), normal adult (HbAA), and normal infant (HbFF)] [99].

Direct stretching experiments involving optical tweezers of normal red blood cells and cells infested in a controlled manner with malaria parasites have revealed quantitative correlations between loss of membrane deformability and exposure to the parasite, at force resolutions on the order of tens of picoNewtons. Such results offer appealing possibilities for further extensions of the present work for diagnostics and drug treatment of diseases [100]. In dual optical tweezers stretching, the targets investigation RBCs were taken from patients with type 2 diabetes mellitus (T2DM) who exhibit diabetic retinopathy (DR), and from patients with birdshot chorioretinopathy (BCR). Statistically significant change was found in the deformability for RBCs from DR patients compared to a control group, but no significant change for BCR patients [101].

The drag force on RBC was much larger than the optical gradient force to result in a poor trapping efficiency. At an optimal flow rate of 100~170 μm/s and the highest optical trapping efficiency with the Bessel-like beam power of ~40 mW. By measuring the drag force on a RBC [102], the equilibrium gradient force (F_{grad}) acting on the RBC was estimated to be 3.55~6.03 pN at an optimal flow rate of 100~170 μm/s [102].

Chapter Three

3 Materials and Methodology

In this chapter we will discuss the experimental for cancer cells and red blood cells. The experimental set up, materials and mechanism of membrane breakdown also will be explained.

3.1 4T1 breast cancer cell culture and treatment

The sample was cultured and treated in the International Ginseng Institute, Tennessee Center for Botanical Medicine Research and laser trapping experiment was done in the department of Physics and Astronomy, Middle Tennessee State University.

4T1 cancer cells were cultured in RPMI1640 medium with 10% fetal bovine serum (FBS) in a 5% CO_2 and 37 °C incubators. Cells were trypsinized i.e the process of cell dissociation using trypsin from the vessel (container) in which they are being cultcured. The passaged (a subculture is a new cell culture made by transferring some or all cells from a previous culture to fresh growth medium) every 2-3 days. After 4T1 cells were trypsinized, they were diluted with RPMI1640 medium, and seeded in a 96-well plate with an intensity of 5,000-7,000 cells per well (100 µL/well). After the cells were attached to the bottom of the wells for 24 h, cells were treated with DMDD at 100 µMol for 2 or 24 h. Each of the untreated group, 2-h treatment group, and 24-h treatment group had six replicate wells. Following treatment, the culture medium in each well was transferred to an Eppendorf tube. Subsequently, wells were rinsed with PBS and 50µL trypsin was added to each well, the detached cells were transferred to the same Eppendorf tube.

3.2 SCT and SCA red blood cells

The blood samples from individuals with a person HbAS and HbSS patients were obtained from the Meharry Sickle Cell Center (MSCC) in an Ethylene Diaminet Tracetic Acid (EDTA) tube which had anticoagulant properties to prevent blood clotting. All samples used in the study were stored at 2 ^{o}C at the MSCC. The blood sample of SCT and SCA were diluted in FBS. The FBS provided a suitable environment for the cells to be suspended in while the dilution provided a large concentration of cells in the viewing range of the microscope.

3.3 Experimental setup and materials

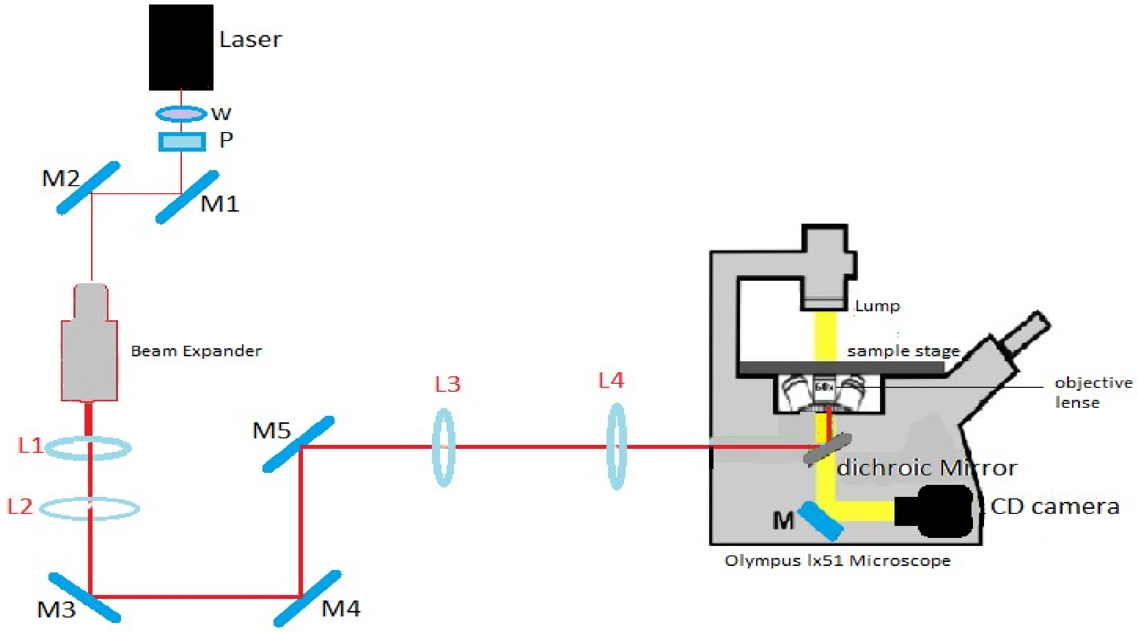

Figure 3.1 A Schematic of the laser trap experimental set-up.

For experiment conducted in trapping and ionizing a cell, the power was measured at two positions. One is before the beam is incident at the get of the microscope after L4 (~4.34W) and at the trap point after exiting the objective lens (as shown Figure. 3.1) (~0.806W).

3.3.1 Laser

The Nd:YVO4 diode laser has a maximum power output of 8 W.

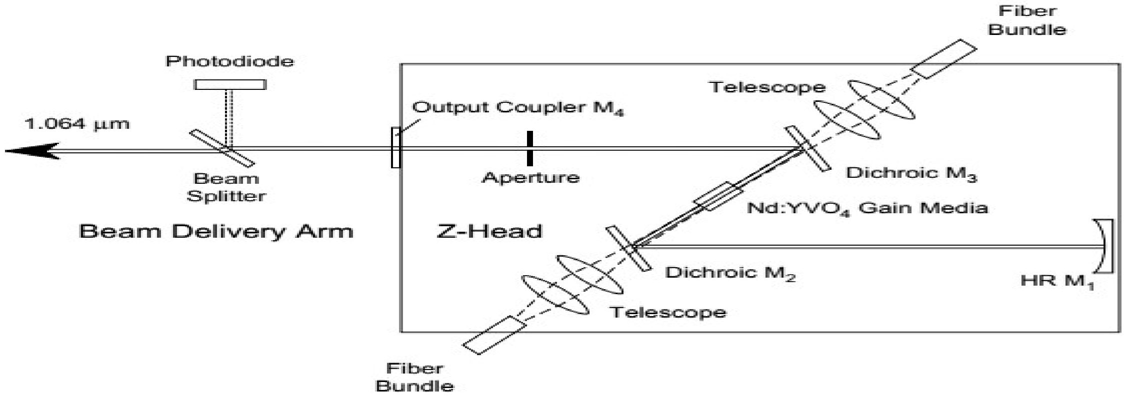

Figure 3.2 Schematic of the Millennia IR Laser Head from [103]

In the diode-pumped laser neodymium yttrium vanadate (NdYVO4) is gain medium as shown in Figure 3.4. Telescopes are used to focus the pump light through dichroic fold mirrors M_2 and M_3 and into the laser crystal where 1064 nm infrared intra cavity light is generated. M_2 and M_3 are highly trans-missive at the diode pump wavelength and highly reflective at 1064 nm. High reflector mirror M_1 and output coupler M_4 define the cavity. The aperture maintains the beam at a size that is optimal for beam overlap in the Nd:YVO4 crystal, thus ensuring efficient cavity light generation in the TEM_{00} mode. Virtually all the 1064 nm infrared light is transmitted by the output coupler and directed out of the Z-head. A beam splitter is used to sample the output and a photodiode provides feedback to the pump diode drivers to provide a constant output in power mode.

3.3.2 Polarizer

When linearly polarized light pass through polarizer as shown in the Figure 3.3, the inensity is given by $I = I_o cos^2\theta$, where I_o is the input intensity and θ is the angle between the beam's initial direction of polarization and the axis of the polarizer. The combination of the polarizer and half-waveplate is shown in the Figure 3.1, and can control the attenuation by varying the angle θ. Rotation of the ½ wave-plate by an angle of ϕ results in a polarization rotation by an angle of 2ϕ, thus the intensity at the output of the attenuator is given by, $I = I_o cos^2 2\emptyset$. If the ½ wave plate rotated by 45^o the polarization plane changes by 90^o.

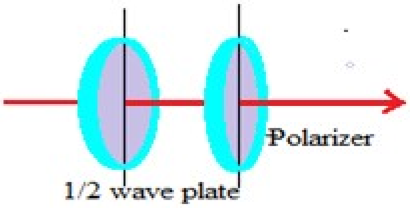

Figure 3.3 The combination of ½ wave plate and polarizer.

3.3.3 Beam expander

Beam expansion or reduction is a common application requirement in most labs using lasers or light sources and optics.

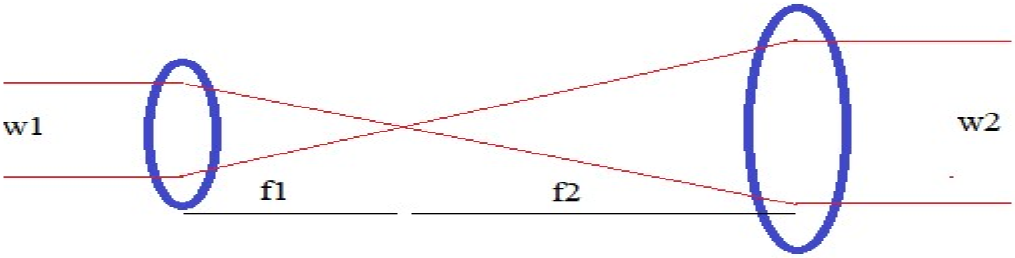

Figure 3.4 Beam expander

In two lens beam expander, the focal length and aperture of the first lens is smaller than the second lens. The first lens should have a diameter larger than the maximum expected input diameter of the beam. For a 20x beam expander the original input beam size 4mm diameter becomes 8cm beam diameter out of the expander. The output beam from the beam expander was resized by lenses L1 and L2 to 2cm as shown in Figure. 3.1.

3.3.4 Lenses and Mirrors

The output beam size of the expander resized to 2cm by the two lenses L1 and L2. separated by distance of the sum of the focal length of the two lenses 25cm. The lens L_1 focuses the beam at the focus of L_1 which is the focus of L_2, hence the beam will emerge as a parallel beam [Figure 3.5 A] and similarly for $L_3$and L_4 [Figure 3.5B].

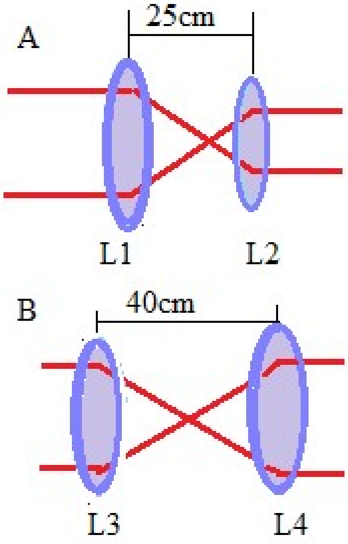

Figure 3.5 Setup of lens to keep the beam target

Mirrors M1 and M2 [Figure. 3.1] direct the beam to the 20X beam expander. The position of M5 was 20 cm away from the third converging lens L3 that is positioned from another converging lens L4 (with the same focal lengths of 20 cm) that was placed 20cm from the back of the objective lens

The Beam steering collimates the beam at the back aperture of the objective lens. The beam steering has two mirrors; each of them can be rotated in both x and y direction perpendicular to the optical axis. The beam propagates in the z-direction, each mirror provides vertical and lateral adjustment. During the alignment, Mirror M4 is used to adjust height of the optical axis to the desired point at the surface of mirror M5. Mirror M5 is used to point the beam in the required direction. The alignment precision was done by measuring the power after L4 and at the tip of the objective lens.

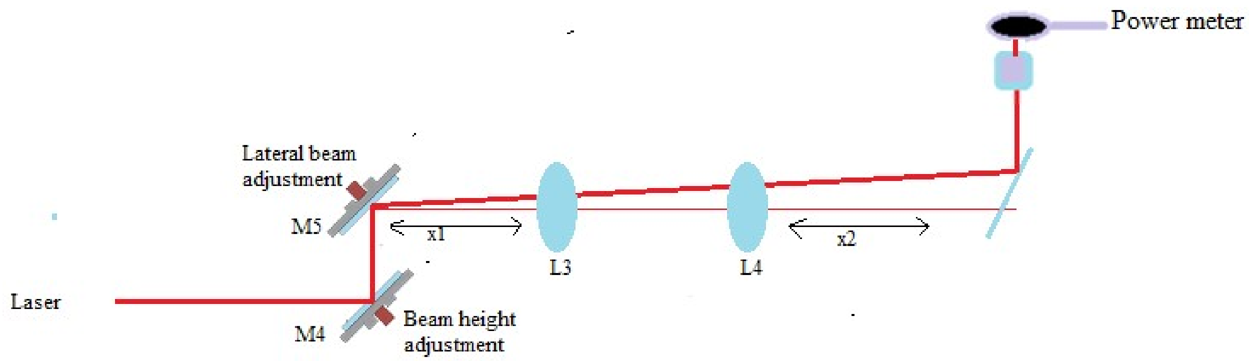

Figure 3.6 Beam steering mirror and lens position

The two lenses have the same focal length of 20cm separated by 2f=40cm from each other. x1 is the distance between mirror M5 and lens L3 and x2 is between lens L4 and the objective lens.

3.3.5 Dichroic mirror

Dichroic mirror is a mirror with significantly different reflection or transmission properties at two different wavelengths. It allows light of certain wavelength to pass through while other wavelengths are reflected. Laser beam coming to dichroic mirror was reflected to the objective lens by arranging 45° from its propagation direction; however, it transmits the lump light passing through the specimen which propagates towards the camera.

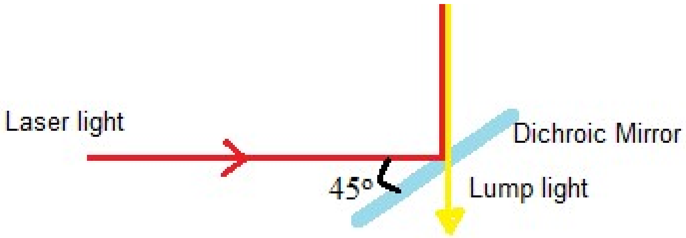

Figure 3.7 Function of dichroic Mirror

3.3.6 Numerical aperture (N.A)

The numerical aperture of a microscope objective is the measure of its ability to gather light and to resolve fine specimen details while working at a fixed object (or specimen) distance. Numerical aperture can be calculated as N.A =n.sinα, Where n is refractive index of immersion medium used between objective lens and cover slip (n=1.51 for oil) and (α=55.87°) as shown in the Figure.3.8.

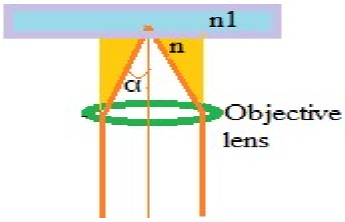

Figure 3.8 Numerical aperture of the objective lens.

3.4 How the trap works?

After the laser pass through the objective lens it focuses at the focal point. The bead suspended in water and the laser attracts at its focus. When the index of refraction of the bead is greater than the refractive index of medium direction the force is intensity gradient. If the particle is displaced axially below the focus (f) rays ‘a’ and ‘b’ are refracted and the new focus is formed below the focus f and is more convergent on the bead. The refocusing of the laser pulls the bead upward to f which is shown in Figure 3.9A. Although, when the particle is above the focus and the ray becomes more divergent, the gradient force pushes the bead downwards and refocuses it at the center of mass [105].

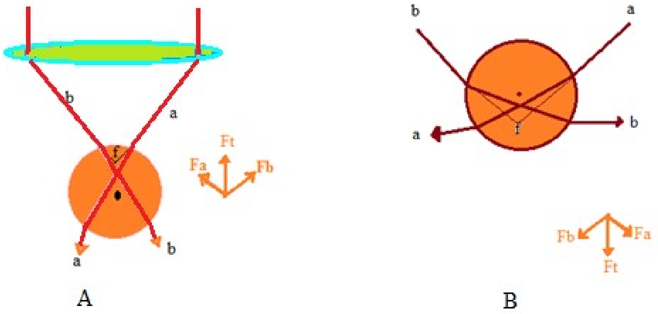

Figure 3.9 The axial displacement of the bead in an optical trap.

Axial displacements of a bead in an optical trap change the relative amount of divergence of the focused laser light. In the absence of the bead, two rays are focused through the objective lens to position of laser focus f, the true laser focus. [Figure 3.9A] Refraction through the bead, which is displaced below the laser focus, causes the new focus to lie below f. Rays ‘a’ and ‘b’ on the bead are more convergent and bend down to the right for ‘a’ and to the left for ‘b’. F_a and F_b are the forces on the bead by the ray ‘a’ and ‘b’, the resultant force of ‘a’ and ‘b’ is Ft directed upward. [Figure 3.9B]When the bead is displaced above the laser focus, the deflected rays ‘a’ and ‘b’ are more divergent, and the resultant force points downward [105].

3.5 Mechanism of Membrane breakdown

External electric fields can induce formation of pores in membranes, and can move cells by dielectrophoresis. The polarization of a membrane material results from the fundamental interaction of electric field with charges. Electric fields exert forces on charges which can either move if they are free to do so or accumulate if they are limited in their motion. The free motion of charges depends on the conductivity of the material while the charge redistribution in a limited space is characterized by its polarizability. Figure 3.10 shows how cells can be polarized due to the restricted motion of ions imposed by the plasma membranes.

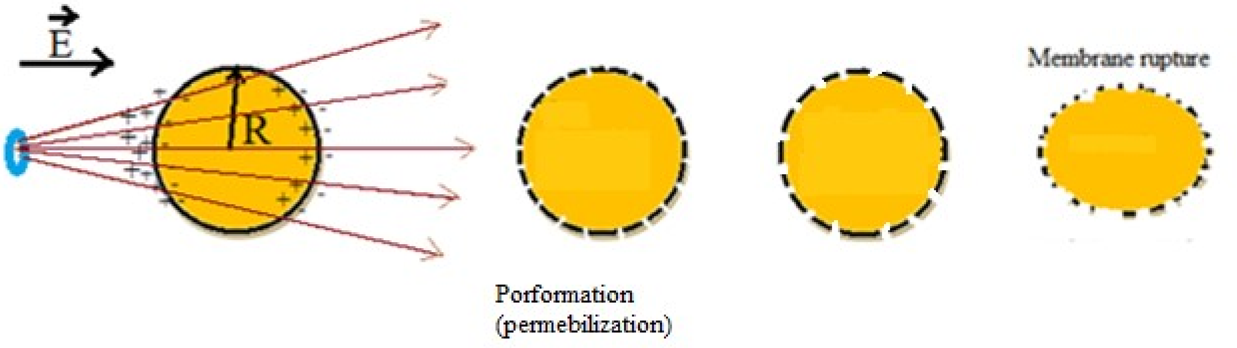

Figure 3.10 Polarization of cell by external electric field.

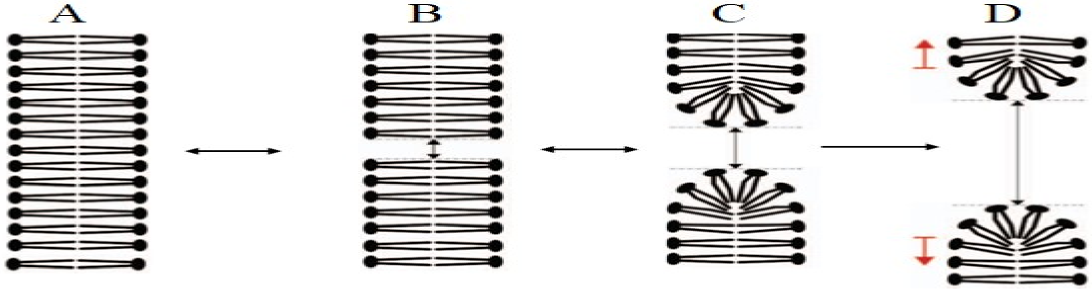

Figure 3.11 (A) Bilayer without pores, (B) with a hydrophobic pore, (C) its reversible transition into a metastable hydrophilic pore, and (D) its irreversible transition into an unstable self-expanding hydrophilic pore [106].

The interaction of the external electric fields with the polarized material results in forces which can then induce motions inside cell or motion of the cell as whole. The motion of ions inside the membrane can result in structural rearrangements or even mechanical fracture in the membrane, can subsequently lead to electroporation. The motion of the cell as a whole can occur even in the absence of a net charge, but only in non-uniform electric fields. It is a consequence of the interaction of the redistributed charges which have zero net charge but locally interact with electric fields of different strengths, which leads to a net force exerted on the cell. This phenomenon is termed dielectrophoresis [107-108]. Dielectrophoresis can also occur in homogeneous external fields as shown in (Figure 3.12) if there are other cells yielding local non-uniform electric field. This leads to mutual attraction of the cells, to their approach and eventually to adhesion [108].

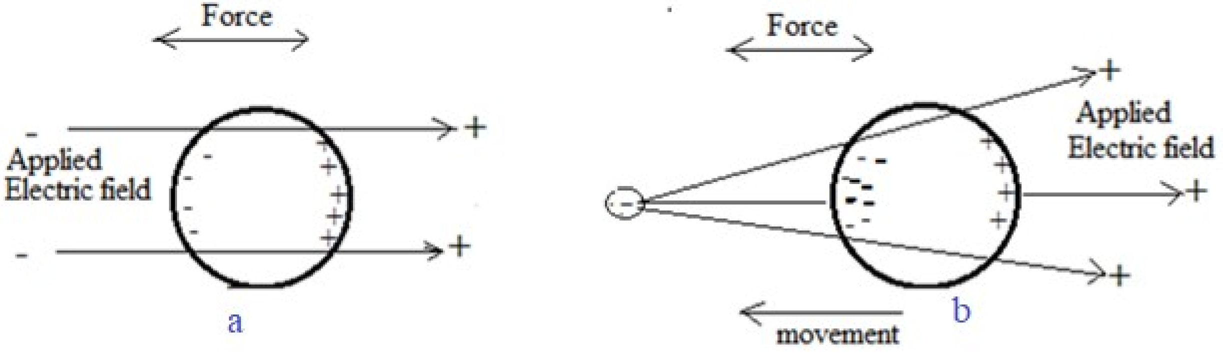

Figure 3.12 (A) homogeneous and (B) inhomogeneous electric field [107].

The magnitude and the type of motion depend on the electric field, the nature and geometry of the cell. Cell membranes have low polarizability and conductivity surrounded by a medium of high conductivity.

4T1 breast cancer cells membrane first damaged by the drug treatment to some extent. The importance of the treatment is to decrease the irradiation energy that breakdown the membrane. After the treatment the cell was exposed to the high-power laser irradiation by trapping technique. The high intense electric field at the focus point breakdown the membrane.

Chapter Four

4 Single and multiple 4T1 cells ionization and post ionization dynamics

The 4T1 cancer cell sample culture which we have discussed in section 3.1 was further diluted with fetal bovine serum ratio to ratio 1:20. The diluted sample of untreated (control), the 2-h and 24-h treated groups were then put on the slide and was covered with cover slit and was mounted on the micro-driven mechanical stage of the microscope. Using the digital camera, we took an image of the cell when free and lying on the bottom of the slide. We then opened the gate at the laser port of the microscope to trap the cell. Successive images of the cell were taken by the digital camera at a fixed frame grabbing rate of 8 frames until the cell is fully ionized and ejected from the trap and disappeared from the field of view of camera. Real live successive images illustrating this process are shown in Figure 4.1 a & b for untreated, Figure 2 c & d for 2-h treated, and Figure 2 f & g for 24-h treated. Our objectives were to study the radiation sensitivity of the 2-h and 24-h treated in comparison with the untreated control group by calculating and analyzing the threshold radiation dose (TRD) for the 4T1 cells. The TRD depends on the corresponding mass and the average radiation energy absorbed by each cell and then the membrane breakdown due this absorption. As shown in the Fig. 4.1(a), (c) and (f) the membrane damaged in different levels. Figure 4.1 (f) were more damaged than Fig. 4.1 (c) and Fig. 4.1 (a) looks normal.

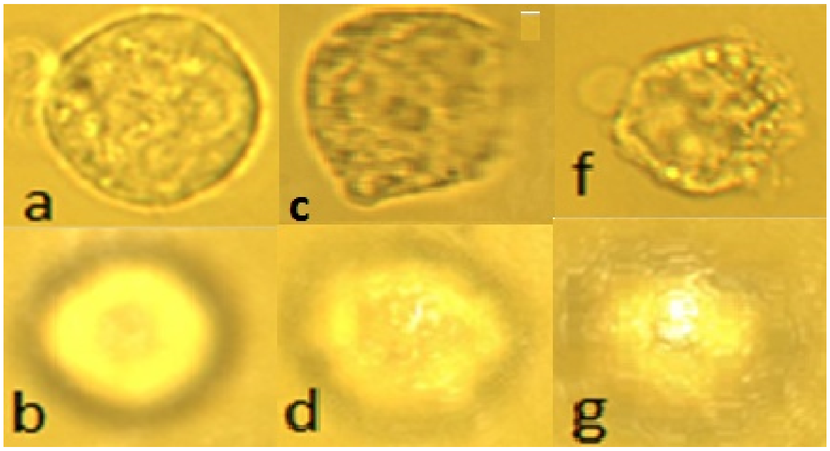

Figure 4.1. The images captured for 4T1 breast cancer cells before and after trapping (a) and (b) for the untreated control, (c) and (d) for 2h treated, (f) and (g) for24h treated

4.1 Threshold ionization energy and radiation dose

Spherical models for 4T1 cells in all the three groups were considered and the diameters, area, time of ionization, displacement were measured, and velocity and acceleration of each cell were calculated using the software Image Proplus6 in pixels [www.imagepro-office.com]. A conversion factor of $7.27\times10^{-8} meter / pixel$, was found using a 3.1μm silicon beads. This conversion factor was used to determine the cross-sectional area, A_{cell}, and the volume for each cell, V_{cell}. The mass of each cell is given by,

$$M_{cell} = \rho V_{cell} \qquad \textbf{4.1}$$

was determined by using the widely accepted density of cancer cells, $\rho =$ 1081 kg/m^3 [109-111].

TRD was determined using the mass calculated for each cell and the average radiation energy absorbed. The average power [P_I=0.806W] incident on the cell was kept constant throughout the ionization of each cell, and the average transmitted power was found to be, P_T=0.64W. In order to measure the transmitted power, we had to cover the slide with a power meter, which blocked the imaging light while the cell was trapped. We then determined the average threshold ionization energy for each cell, disturb cooperation

$$TIE = \frac{A_{cell}}{A_{beam}} \left(P_I - P_T\right) T \qquad 4.2$$

where T is the ionization period which was determined using the digital camera image grabbing rate and the number of images captured during the time from the instant each cell entered and the instant it got ejected from the trap. A_{beam} is the beam size determined at the trap location using the numerical aperture of the objective lens [112]. The TRD was then calculated for each 4T1 cells using

$$TRD = TIE / M_{cell} \qquad 4.3$$

Here the TIE is the minimum radiation energy absorbed by the cell that creates a significant amount of charge through ionization that leads to irreversible damage to the cell. When the cell riches to this threshold charge it experiences a stronger electrostatic force than the trapping force that results in the ejection of the cell from the trap [23-25].

4.1.1 Results and discussion

4.1.1.1 Single cell ionization

A total of 89, 86, and 128 4T1 cells for the control untreated, 2h, and 24h treated groups were studied, respectively. For each of these groups, the basic statistical parameters for the average ionization time ($\overline{T}$), cross-sectional area $(\overline{A}_{cell})$, volume $(\overline{V}_{cell})$, mass $(\overline{M}_{cell})$, , TIE, and TRD are given in Table 4.1. The values for the average ionization time calculated in Table 1 clearly show that as treatment period increases the ionization time decreases. On the other hand, the average cross-sectional area and the volume calculated using a spherical model do not display significant differences. This also results in similar values for the calculated average masses in the three groups. These close values indicate any variations in response to radiation for the three groups primarily affected by inherent biochemical structural differences caused by the dose and period of treatment by DMDD.

Untreated 4T1 control group (89 Cells)		
Quantities	Mean	SD
T (sec)	341.2	145.8
A_{cell} $(\mu m)^2$	204.2	72.1
M_{cell} (ng)	2.3	1.3
V_{cell} $(\mu m)^3$	2291.6	1290.5
TIE (mJ)	81.3	63.5
TRD (J/μg)	32.6	14.8
2-h treated 4T1 group (86 Cells)		
Quantities	Mean	Std. Dev.
T (sec)	225.4	112.3
A_{cell} $(\mu m)^2$	193.6	76.0
M_{cell} (ng)	2.1	1.2
V_{cell} $(\mu m)^3$	2142.1	1239.5
TIE (mJ)	48.8	37.7
TRD (J/μg)	22.4	11.4
24-h treated 4T1 group (128 Cells)		
Quantities	Mean	Std. Dev.
T (sec)	102.5	70.0
A_{cell} $(\mu m)^2$	209.8	68.5
M_{cell} (ng)	2.4	1.1
V_{cell} $(\mu m)^3$	2377.0	1144.1
TIE (mJ)	23.8	20.4
TRD (J/μg)	9.4	6.4

Table 4.1 Basic statistical parameters for the measured and calculated quantities: Area, Mass, TIE, and TRD.

Using the ionization time, the area of each cell and the beam at the trap location, the power incident and power transmitted, we have calculated the absorbed threshold ionization energy using Eq. (4.2). The average values, for the untreated control, 2h, and 24h treated groups, the average absorbed threshold ionization energy, were found to be, $TIE = 81.3 \pm 63.5\ mJ$, $48.8 \pm 37.7\ mJ$, and $23.8 \pm 20.4\ mJ$, respectively. The higher standard deviation for the three groups is due to the wide range of the size of the cells that is one of the factors affecting the magnitude of the ionization energy. The statistical distributions for TIE for all cells in each group are displayed using pie-charts, box plot and histograms in Figure 4.2 (a)-(c). In each graph the data coded red represents the untreated control, green is for the 2h treated, and blue is for 24h treated 4T1 cells. From these distribution graphs and the calculated average values, we can clearly see that the TIE for the treated groups is less than the untreated control group. This effect is amplified with increase in the duration of treatment as we can see from the lower TIE for the 24 h treated than the 2 h treated as shown in Figure 4.2 (b). The comparison of TIE in the three groups and TRD was also explained by using pie chart. In the pie chart in Figure 4.2 (c) the TIE for untreated 4T1cells makes up 52.9% of the pie, while for 2 h and 24 h treated 4T1 cells covers 31.9% and 15.2%, respectively, as we have used different number of cells in each group. The absorbed TRD for each cell in each group is calculated using the masses in Eq. (4.1) and the TIE in Eq. (4.2). The results for each group, using the same color coding, are also displayed in Figure 4.3 (a)-(c). For the untreated control, the 2-h treated, and 24-h treated groups, the average absorbed TRD were found to be, $TRD = 32.6 \pm 14.8 J / \mu g$, $22.4 \pm 11.4 \ J / \mu g$, and $9.4 \pm 6.4 \ J / \mu g$, with 50.7%, 34.8% and 14.5% making up the pie chart as shown in Fig. 4.3 (c), respectively. This also shows lower radiation dose in the 4T1 cells treated with DMDD than the control group and this effect is also amplified with treatment period increase as shown in Figure 4.3 (b).

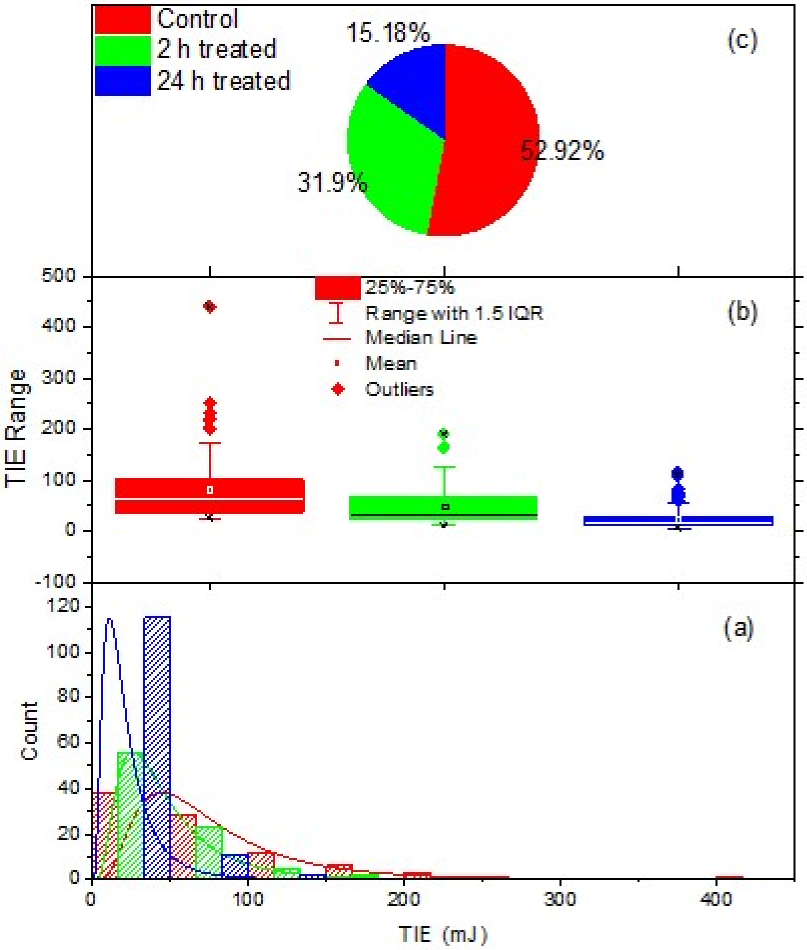

Figure 4.2 The statistical distributions for the TIE for untreated control group (red), 2h treated group (green), and 24h treated group (blue) 4T1cells**.**

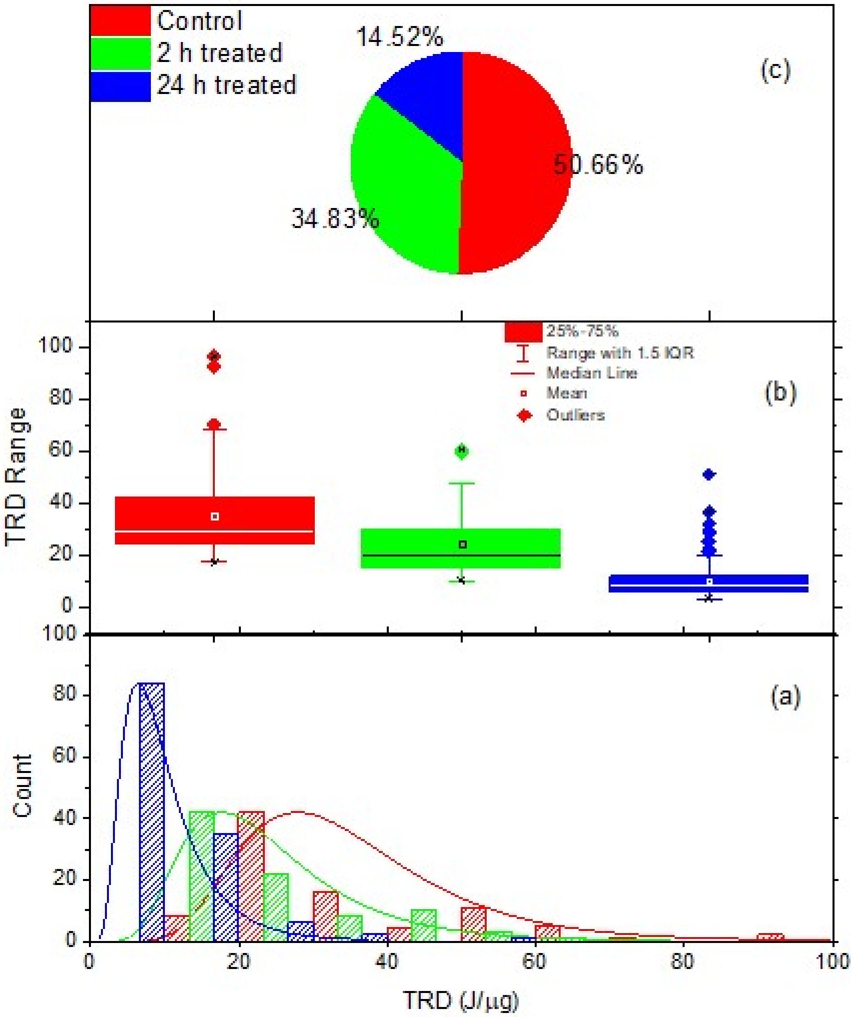

Figure 4.3. The statistical distributions for the TRD for untreated control group (red), 2h treated group (green), and 24h treated group (blue) 4T1cells.

Further validity of the results obtained for TIE and TRD is also confirmed using independent two-sample t-statistical analyses using Origin2018 [www.originlab.com] software. Generally, in t-statistics the t-Test procedure automatically provides two sample tests of the mean difference. One is based on the assumption that the variances of the two samples are equal and the other is not. These tests are often referred to as "unpaired" or "independent samples" t-tests, as they are typically applied when the statistical units underlying the two samples being compared are non-overlapping which is the case for the results obtained for both the TIE and TRD. The results for t-test statistics for the TIE and TRD are given in Table 4.2. These results show that there was a significant difference between the control group and the 2-h treated, the control group and the

24-h treated and also the 2-h treated and 24-h treated groups. At 0.01significant level (99% confidence), in all the three independent two-sample t-test for both equal and not equal variance assumptions the mean values for both TIE and TRD in the two-samples are significantly different. This is, in fact, supported by the significantly smaller p-values than our 0.01significant level and the t value that confirms the significant difference between the three samples. In fact, from the results in Table 4.1 for the mean TIE and TRD differences for the lower and upper limits in the two-sample for the three confidence levels, we can conclude that both the mean TIE and TRD for 24-h treated significantly less than 2-h treated which has a smaller value than the control group. Therefore, t-test statistics analyses further confirms the treatment has significantly increased the radio-sensitivity of the 4T1 cells.

Control group vs 2h treated group						
	TIE			TRD		
	t Stat.	DF	Prob>|t|	t Stat.	DF	Prob>|t|
Equal Variance	4.12	173.0	4.9E-05	5.1	173.0	9.4E-07
NOT Equal Variance	4.2	136.1	4.7E-05	5.1	165.0	8.9E-07
	Two-sample mean values difference					
Confidence level	M.Dif	L. Limits	U. Limit	M.Dif	L. Limit	U. Limit
99%	32.3	12.1	52.5	11.1	5.4	16.7
Control group vs 24h treated group						
Equal Variance	9.7	215.0	1.5E-18	15.8	215.0	7.7E-38
NOT Equal Variance	8.3	100.4	4.4E-13	14.0	111.0	3.6E-26
	Two-sample mean values difference					
Confidence level	M.Dif	L. Limits	U. Limit	M.Dif	L. Limit	U. Limit
99%	58.0	42.4	73.6	25.3	21.1	29.4
2h treated group vs 24h treated group						
Equal Variance	6.9	212.0	5.9E-11	10.7	212.0	1.3E-21
NOT Equal Variance	6.3	124.8	5.4E-09	9.6	120.9	1.2E-16
	Two-sample mean values difference					
Confidence level	M.Dif	L. Limits	U. Limit	M.Dif	L. Limit	U. Limit
99%	25.7	16.0	35.4	14.2	10.7	17.6

Table 4.2. Hypothesis testing by two-sample t-test

In order to study the relationship between the ionization radiation energy and mass of the 4T1 cells, we have analyzed the TIE and TRD as the function of the mass of the individual cells. The results in Figure 4.4 (c) and (f) displays the TIE and TRD versus mass for all 4T1 cells in the untreated control (red), 2-h treated (green), and 24-h treated (blue) groups. In order to establish a clear relationship between the TIE and TRD with the mass of the cells, we have made statistically valid data reduction using graphical data analysis program software, Origin 2018[www.originlab.com]. The reduced data is shown in Figure 4.4 (a) and (b) for the TIE and in Figure 4.4 (d) and (e) for the TRD. In this statistical reduction method, we first sort each data by the TIE or TRD in ascending order and eliminated the two minimum and the two maximum values from each of the three groups. We then made another sorting by mass in ascending order and eliminated the two minima and the two maxima values. The reduced data obtained following this procedure is shown in Figure 4.4 (b) for the TIE and in Figure 4.4 (e) for the TRD. Further reduction was made by sub-grouping the data in Figure 4.4 (b) and (e) with 0.2 ng mass increment and calculating the average mass, TIE, and TRD for each subgroup. These results are shown in Figure 4.4 (a) and (d) for TIE and TRD, respectively. Figure 4.4 (a) predicts an increase in TIE with the increase of the mass of the cells for all the three groups. It also consistently reconfirms the reduced TIE for the treated 4T1cells with the lowest for the 24-h treated group. On the other hand, although the TRD vs mass in Figure 4.4 (d) consistently confirms the low TRD for the treated group of cells, it predicts an inverse relationship between the TRD and the mass of the 4T1 cells in all three groups.

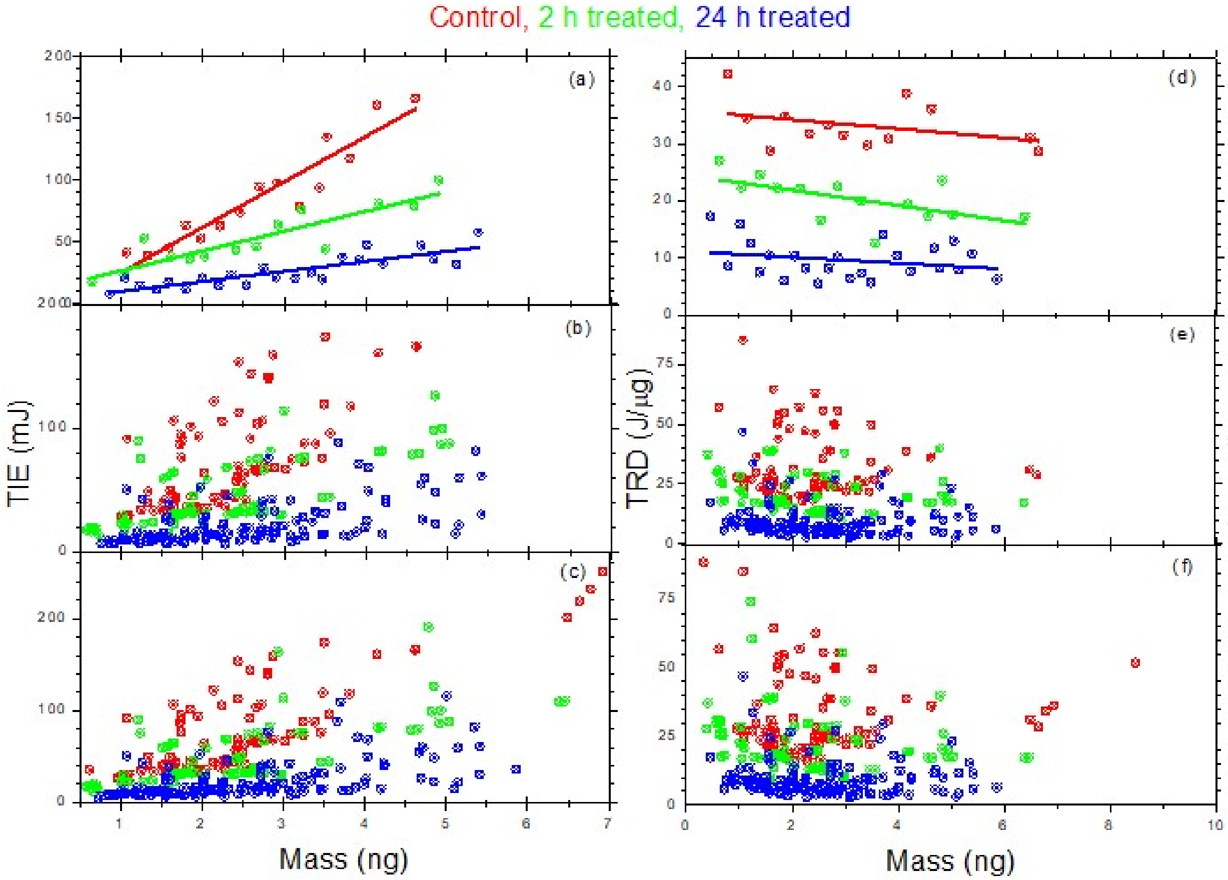

Figure 4.4. The TIE (a-c) and TRD (d-f) vs mass for untreated control (red), 2h treated (green) and 24h treated (blue) 4T1 breast cancer cells: (c) and (f) for all cells (b) and (e) for the reduced data, and (a) and (d) is further reduced data with a linear fit.

4.1.1.2 Multi cell ionization

In TIE and TRD studies for single cell, during the trapping process, we had to keep the cell isolated from the other cells until it is fully ionized and ejected from the trap. This was challenging as the ionization period is relatively longer for cancer cells compared to other small cells such as RBCs [24-25]. During this period, other nearby cells are attracted by the strong gradient force and jump into the trap at different times, which results in having multiple cells in the trap. Although these cells enter at different times into the trap, all the cells eject at the same time after ionization. In this section we wish to estimate the TIE and TRD when there are multiple cells in the trap for the untreated control, 2-h and 24-h treated groups. The purpose of this analysis is to study whether the TIE and TRD are affected by the addition of one or more cells while the cell that entered first undergoes membrane breakdown and charges continue to build up due to radiation damage. To accomplish this objective, in each of the untreated control groups, the 2-h and the 24-h treated groups, we formed five subgroups based on how many cells present in the trap during the ionization period: 1-cell, 2-cells, 3-cells, 4-cells, and 5-cells. The first group (1-cell) is what we already studied in the previous section and it is included here for comparison purposes. The images displayed in Fig. 4.5 show untreated 2-cells, 3-cells, 4-cells, and 5-cells ionization. Figure 4.5 (a) is the image captured when one cell is already in the trap (T) and the second is being accelerated towards the first. Figure 4.5 (b) is the image captured when both cells are inside the trap (T). Similarly, Figure. 4.5(c) is when there are two cells in the trap and the third is moving towards; Figure. 4.5 (d) is when all three cells are in the trap (T); Figure 4.5 (e) is when there are three cells in the trap and the fourth is on its way, and Figure 4.5 (f) is when all four cells are in the trap (T). Next, Figure 4.5 (g) is when there are three cells in the trap and two cells are on their way, and Figure. 4.5 (h) is when all five cells are in the trap (T). In multiple cell ionization, as we can see from Figure 4.5, the cells do not always enter the trap at the same time, but all cells do eject from the trap at the same time. Therefore, the ionization period (T) is estimated for all subgroups using the images captured when the first cell enters the trap and the image when all cells eject from the trap. Then, the absorbed TIE is calculated using Eq. (4.2), following the same procedure we used for single cell ionization. In multiple cell ionization, the mass of the cells in the trap are also estimated using Eq. (4.1). However, because the mass of the cells in the trap is the sum of the masses of the individual cells in the trap with the same density, we replace V_{cell} by the V_{sum} which is the sum of the volume of the individual cells in the subgroups; hence, Eq. (4.1) becomes $M_{subgroup} = \rho V_{sum}$. For example, for subgroup-2 (2-cells in the trap), we have $V_{sum} = V_1 + V_2$ and $M_{subgroup} = \rho\left(V_1 + V_2\right)$ Then by replacing M_{cell} with $M_{subgroup}$, we calculated the TRD for each subgroup in the untreated control, the 2-h, and 24-h treated groups.

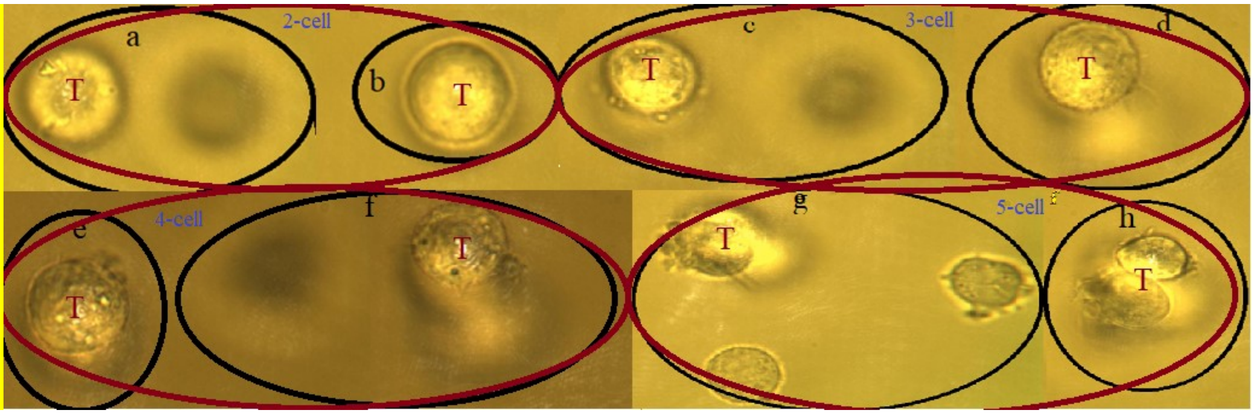

Figure 4.5 Multi cell ionization: untreated 2-cell, 3-cells, 4-cells and 5-cells ionization, the letter (T) represented the trapping point, for 2-cells (b) trapped and (a) one trapped the other is free, for the 3-cell (c) two trapped and one free (d) trapped, for 4-cell (f) three trapped and one free (e) trapped and for 5-cell (g) three rapped two free, (h) all trapped.

The results for the TIE and TRD for multiple cells along with single ionization are displayed using a histogram and the box-and-whisker plot in Fig. 4.6. The histograms on the left side of Figure 4.6 are for the TIE, whereas the right side is for the TRD. In both left and right sides of Figure 4.6, (a) is for the untreated control group, Figure 4.6 (b) is for the 2-h treated group, and Figure 4.6 (c) is for the 24-h treated group. In each of these histograms, the subgroups 1-cell, 2-cells, 3-cells, 4-cells, and 5-cells are represented by pink, yellow, orange, navy, and cyan, respectively. From the distribution curves in the left side of Figure 4.6 (a)-(c), the shift in the peak values to the right indicates that the TIE increases as the number of cells increases in the trap consistently for control, 2-h, and 24-h treated groups. This is clearly shown in the box-and- whisker plot in Figure 4.6 (d). The summary for the values for the basic statistical parameters for the TIE is given in Table 4.3. The results clearly show that the average TIE for the five subgroups (1-cell to 5-cells) increases as the number of the cells increases consistently regardless of the treatment.

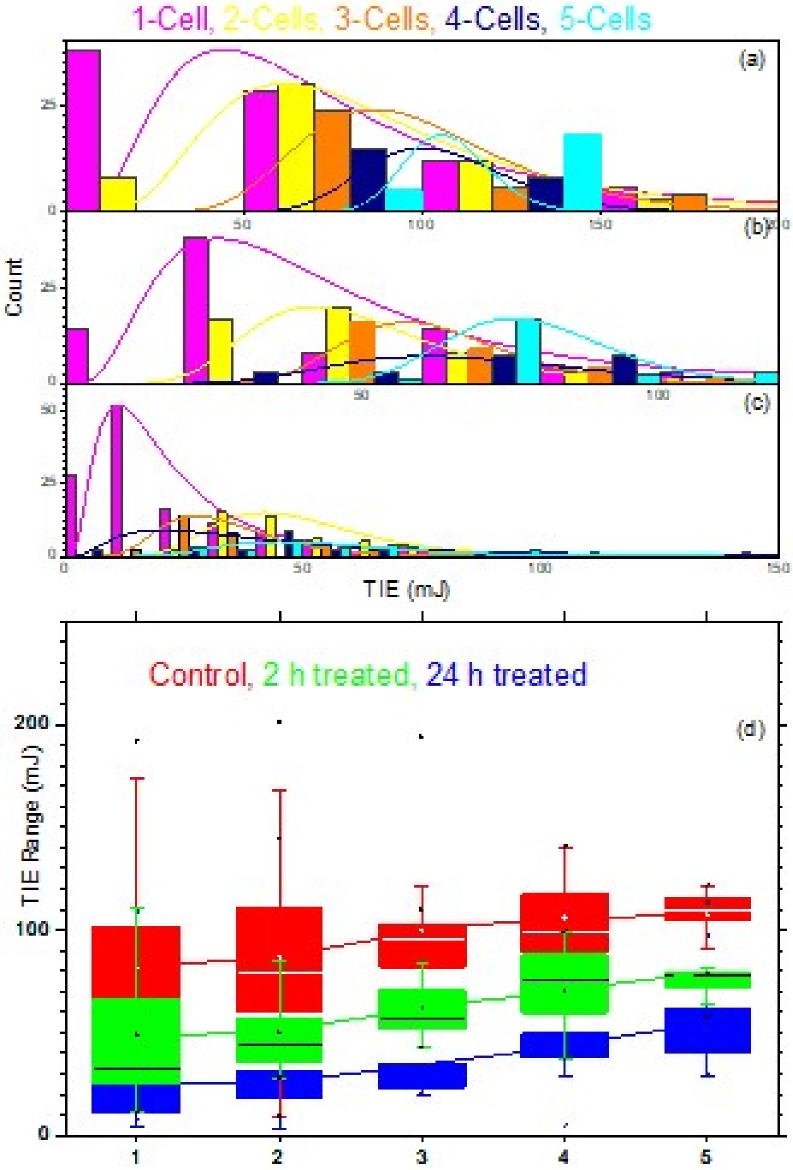

Figure 4.6. TIE in single and multiple cell ionization. The statistical distribution displayed by the Histograms (a) Untreated control group, (b) 2 h treated, and (c) 24 h treated. In each of these histograms the number of cells in the trap is represented by the color coded legend: 1-cell (magenta), 2-cells (yellow), 3-cells (orange), 4-cells (navy), and 5-cells (Cyan). (d) displays the range of the TIE in each subgroup (1, 2, 3, 4, and 5) for Control (red), 2h (green) and 24 h (blue) treated groups. The solid lines in (d) connect the average TIE for each subgroup in each group.

It is important to make a quantitative comparison within the subgroups (1-5 cells) and between the three groups by analyzing the relative TIE percentage increase. For any of the three groups, putting aside any effects resulting from intracellular electrical and thermal interactions mediated by the radiation field, theoretically we expect 200-500% relative increase in the TIE for corresponding to 2-5 cells compared to the single cell. However, the calculated values were found to be 13.4%, 20.7%, 24.0%, and 29.3% (for untreated), 15.8%, 38.1%, 46.8% and 54.3% (for 2-h treated), and 18.8%, 35.3%, 54.1% and 59.8% (for 24-h treated). Although our estimation for the TIE in multiple cells ionization is by no means perfect, the results indicate an astounding intracellular electrical and thermal effect due to the infrared radiation used to trap the cells. We have also made a relative comparison between the treated groups with that of the control group for the corresponding multiple cells (2-5 cells) TIE. The calculated results were 42.3%, 37.9%, 35.6% and 26.5% for the 2-h treated and 47.7%, 45.1, 38.8% and 30.7% for the 24-h treated group, less than the corresponding values in the control group. These results reconfirm the increase in the radio sensitivity due to the treatment by DMDD that we discussed for single cells in the previous section.

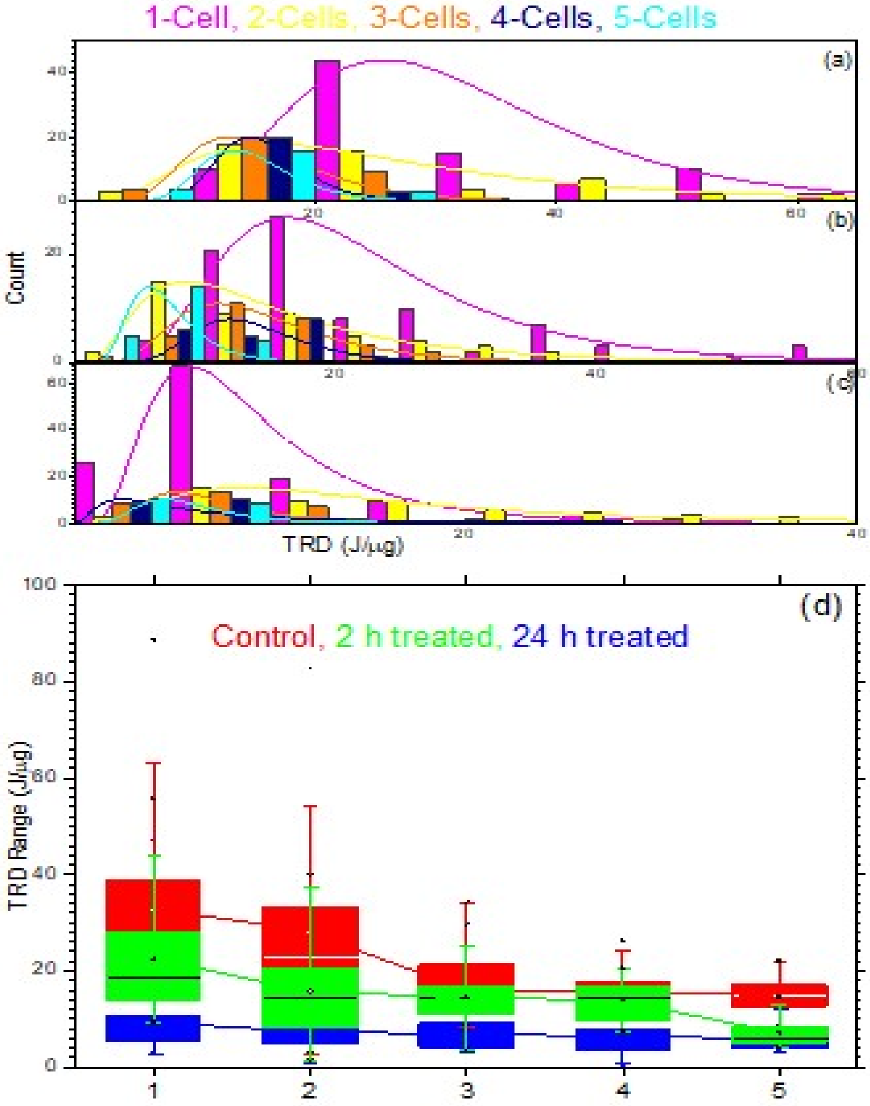

Figure 4.7. TRD in single and multiple cells ionization. The statistical distribution displayed by the Histograms (a) Untreated control group, (b) 2 h treated, and (c) 24 h treated. In each of these histograms the number of cells in the trap is represented by the color coded legend: 1-cell (magenta), 2-cells (yellow), 3-cells (orange), 4-cells (navy), and 5-cells (Cyan).. (d) displays the range of the TIE in each subgroup (1, 2, 3, 4, and 5) for Control (red), 2h (green) and 24 h (blue) treated groups. The solid lines in (d) connect the average TIE for each subgroup in each group.

The corresponding calculated TRD for multiple cells and for single cells is displayed using similar graphs and the same color coding on the right side of Fig. 4.7. Unlike the TIE, however, the distribution curves in all three groups- control (Figure 4.7 (a)), 2-h (Figure (4.7 (b)), and 24-h

(Figure 4.7 (c)) treated shifts to the left, which indicates a decrease in TRD with an increase in the number of cells in the trap. This is clearly displayed in the box-and-whisker plot in Figure 4.7 (d) for control (red), 2-h (green), and 24-h treated (blue). The values for the basic statistical parameters in the TRD are also summarized in Table 4.3. The results show that as the number of cells in the trap increases from 1-5 cells, the average value for the TRD decreases consistently: 32.6 - 14.74 J/µg for the control: 22.4 - 7.1 J/µg for the 2-h treated; and 9.4 - 6.0 J/µg for the 24-h treated group. The relative decrease in multiple (2-5) cells' average TRD as compared to single cells was found to be 13.9%, 51.1%, 51.7%, and 54.8% for untreated; 29.5 %, 35.4%, 38.4 %, and 66.7 for 2-h treated; and 20.1%, 25.9 %, 32.8%, and 35.7% for 24-h treated.

Untreated 4T1 control group							
		TIE (mJ)		Mass (ng)		TRD (J/µg)	
SG	N	Mean	SD	Mean	SD	Mean	SD
1	89	81.3	63.5	2.5	1.4	32.6	14.8
2	54	86.8	37.7	3.5	1.1	28.1	17.2
3	34	99.7	34.8	5.1	1.4	16.0	6.5
4	23	106.0	21.4	6.9	1.0	15.8	3.9
5	23	107.4	11.1	7.7	1.9	14.7	3.8
2-h treated 4T1 group							
		TIE (mJ)		Mass (ng)		TRD (J/µg)	
1	86	48.8	37.7	2.3	1.3	22.4	11.4
2	49	50.1	20.7	4.2	3.4	15.8	9.1
3	30	61.9	14.9	4.9	2.4	14.5	5.6
4	20	70.4	19.9	5.5	2.7	13.8	4.1
5	23	78.9	14.7	8.2	2.7	7.1	3.1
24-h treated 4T1 group							
		TIE (mJ)		Mass (ng)		TRD (J/µg)	
1	128	23.8	20.4	2.6	1.2	9.3	6.4
2	56	26.2	11.9	3.9	1.5	7.5	4.4
3	30	34.0	14.4	5.1	1.6	6.9	2.8
4	21	43.1	18.3	7.7	2.6	6.3	3.8
5	20	54.7	19.9	9.5	2.0	6.0	2.6

Table 4.3. The values for the basic descriptive statistical parameters for the TIE, the mass, and TRD for the five subgroups in the control untreated, 2-h treated and 24-h treated groups of 4T1 cell-line.

The results found for both the TIE and TRD multiple cells ionization (2-5 cells) in comparison with that of single cell predicts interesting physical processes that could have significant implications for radiation dosimetry, especially for combined modalities of cancer treatment that include chemo and possibly hyperthermia therapy. In order to explain these observed effects, following a similar statistically valid data reduction, we have examined how both TIE and TRD changes as a function of mass when multiple cells (2-5 cells) inter the trap. These results are shown using double-y axis graphs in Figure 4.8 for the control ((a) and (b)), 2-h ((c) and (d)) and 24-h ((e) and (f) treated. In each of these graphs the left and the right axes represent the TIE and the TRD, respectively. Furthermore, in all these graphs the data points for TIE and the TRD for the number of cells in the trap are described by same color coding (2- cells (yellow), 3-cells (orange), 4-cells (Navy), and 5-cells (Cyan)) using different symbols (rectangle, circle, triangle, and star). These symbols are filled with the corresponding color for the TIE but not for the TRD. The graphs in the bottom row (b), (d), and (f) display all the calculated data for the TIE and TRD vs mass whereas the graphs in the top row (a), (c), and (e) display the reduced data with the linear fit that is obtained following a similar procedure we used for single cell. The linear fit (TIE and TRD) to the reduced data in Figure 4.8 (a), (c), and (e), consistent to the results for the single cell in Figure 4.4, predicts an increase in the TIE and a decrease in the TRD with mass in multiple cell ionization in all three groups.

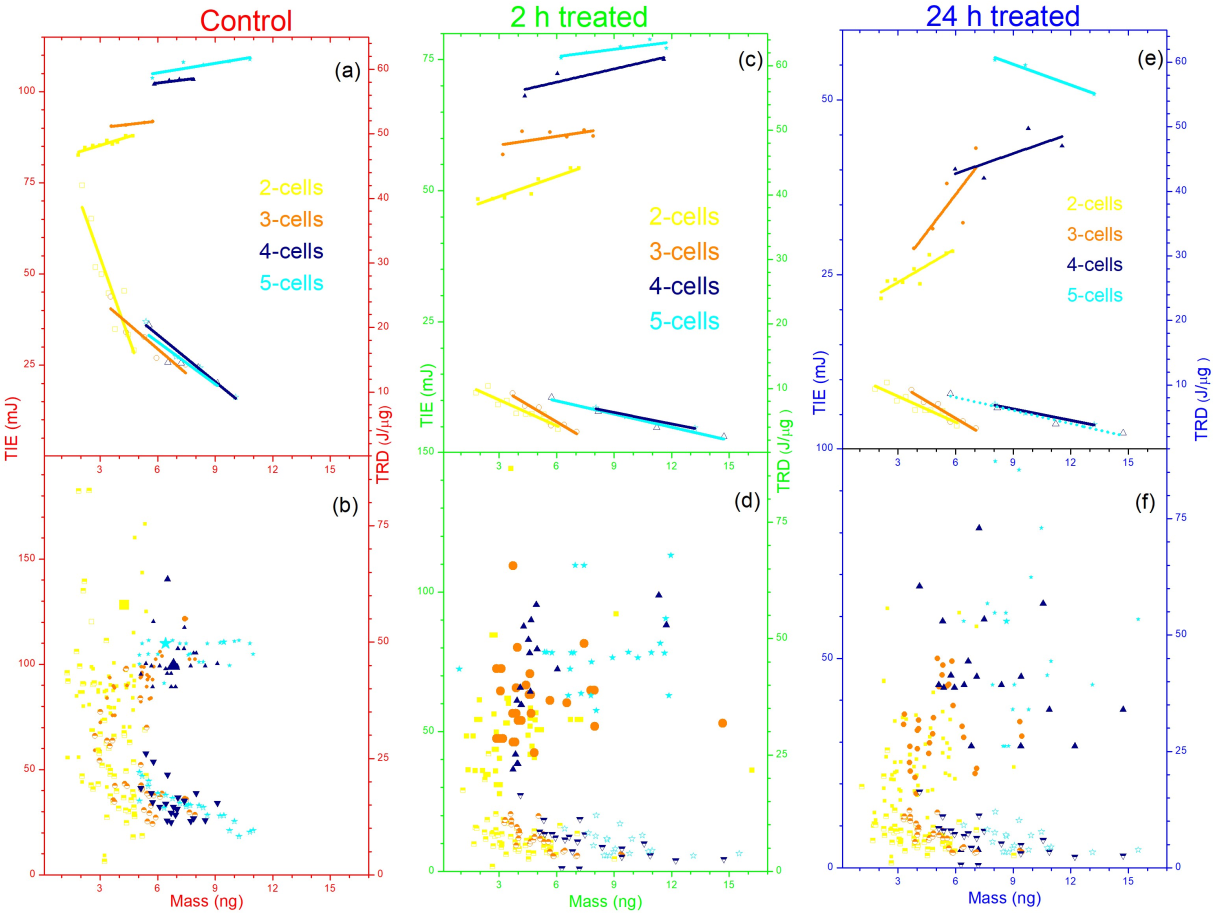

Figure 4.8. Multiple cell TIE and TRD vs mass for untreated control (left (a) & (b)), 2-h treated (middle (c) & (d)), and 24-h treated (right (e) & (f)). The number of cells in the trap is represented by the color coded legend: 2-cells (yellow), 3-cells (orange), 4-cells (navy), and 5-cells (Cyan). Each of these graphs are double-y axis graphs where the left axis represent the TIE and the right axis represent the TRD. The bottom graphs (b), (d), and (f) displays the complete data for each case of multiple cell ionization (2-cells (yellow), 3-cells (orange), 4-cells (navy), and 5-cells (Cyan)) for the TIE vs mass (Filled: : rectangle, circle, triangle, star) and the TRD vs mass (unfilled: rectangle, circle, triangle, star). The top row graphs display the corresponding reduced data with linear fit are for TIE (solid lines) and TRD (dotted line).

The low TRD we observed in multiple cell ionization could primarily be due to the gradual charging of the cell and elevated temperature resulting from the infrared laser. Laser radiation kills cancer cells by damaging their DNA. This can happen when the laser incident on the cancer cells delivers enough amount of ionization energy resulting in the dielectric breakdown. It is well known that this minimum energy (TIE) or minimum radiation dose (TRD) can be affected when it is used along with chemo or hyperthermia. In the absence of the laser radiation, a simplistic physical model of a cell (in this case, a 4T1 cell) is a dielectric sphere filled with a collection of different electric dipoles. When it is exposed to a rapidly oscillating electric field like that of the laser radiation, these various dipoles respond differently by creating a stronger oscillation that aligns with the polarization direction of the radiation field. This leads to a stronger oscillating global polarization in the cell which, otherwise, is zero in the absence of the field. When the electric field becomes strong, the dipoles with weak strength start to break and free charges begin to develop in the cell. As the cell consists of different types of molecules characterized by different dipole strength, the different types of dipoles require different energy and break at different times. Consequently, the charge buildup is a gradual, time-dependent process. Furthermore, due to the Gaussian nature of the laser beam, different parts of the cell receive different electric field strengths (with the strongest at the center of the beam waist). This field gradient also contributes to the gradual charge buildup in the cell. This process could have a significant impact in the threshold radiation dose in multiple cell ionization when cells enter the trap at different times. When the first trapped cell undergoes dielectric breakdown by the radiation and the charge continues to build, any other cells entering the trap face the electric field of the charge on the first cell in addition to the rapidly oscillating electric field from the radiation. The electric field due to these free charges on the cell(s) that is (are) already in the trap causes extra damage in multiple cell ionization. Consequently, the TRD becomes smaller as the number of the cells increases. We have seen this consistently in all three groups. For example, in the untreated control group, the TRD which is measured by the ionization energy from the radiation (the laser): 5-cells (14.7±3.8), <4-cells (15.8±3.9), <3-cells (16.0±6.5), < 2-cells (28.1±17.2), <1 cell (32.6±14.8) in J/μg.

The second major factor that could contribute to the lower TRD in multiple cell ionization is the hyperthermia effect. The laser used to trap the cells is in the infrared (1064 nm). The absorption of this wavelength by water molecules in the cell or in the surrounding suspension medium at such power could be significant and it can significantly elevate the temperature in surrounding medium and the trapped cell. Therefore, when other cell(s) enter the trap, they face this elevated temperature. Studies have shown that at elevated temperature, 42-46 ° C, cancer cells can die due to lack of glucose or the change in structure and enzymatic proteins [113].

4.2 Post ionization dynamics

Membrane breakdown build up more charges on the cell and the electrostatic force becoming stronger and stronger until it's overcomes the gradient trapping and drag forces. At this instant the ionized cell gets ejected from the trap. As we have seen in our study of threshold ionization energy in the previous section, membrane breakdown is facilitated by the DMDD treatment. The charge resulting from such membrane breakdown in the untreated vs treated is not known. In this section we wish to study the magnitude of the charge developed in the untreated, 2 hr treated and 24 hr treated by analyzing the post ionization dynamics of each individual cell. The post ionization dynamic quantities such as displacement, velocity and acceleration depend on the charge. Using two different approaches we have analyzed these quantities to determine the charge developed in each cell. In the first approach first we solve the equation of motion for r(t) and using Nonlinear curve fitting model we fit the displacement vs time data for the equation of r(t) and then the charge determined by assuming unknown electrical susceptibility for each treated or untreated cells. For the second approach we differentiate the displacement vs time data using origin pro and determined the velocity and acceleration. The trapping force calculated numerically using the refractive index calculated in the first approach, finally the charge was calculated. In this section we discuss, compare, and contrast the methods used and the results obtained using these two approaches.

4.2.1 The Forces

The cells are suspended in FBS and trapped by the laser gradient force until it becomes ionized and ejected from the trap due to an electrostatic force resulting from the charge developed. At the instant it gets ejected it also experiences a drag force. Thus the post ionization dynamics is determined by Newton's equation of motion,

$$m \frac{d^2 \vec{r}}{dt^2} = \vec{F}_e - \vec{F}_d - \vec{F}_t, \qquad 4.4$$

where *m* is the mass, $\vec{r}$ is the post-ionization position of the charged cell from the center of the trap, $\vec{F}_e, \vec{F}_d,$, and $\vec{F}_t$ are the electrostatic, the drag, and the trapping forces, respectively.

<u>**The electrostatic force**</u>: While the cell is in the trap and undergoes ionization by the electromagnetic field radiation, there is a charge buildup due to membrane breakdown. This free charge density depends on both position and time and can be represented by $\rho(\vec{r},t)$. Let the magnitude of the electric field for a laser beam polarized along $\hat{s}_o$ direction on the x-y plane and propagating along the z-direction, as shown in Figure 4.9a, be $E(\vec{r},t)$. Then the corresponding magnetic field for this laser beam is given by

$$\vec{B}(\vec{r},t) = \frac{n}{c} E(\vec{r},t)\left(\hat{z} \times \hat{s}_o\right), \qquad 4.5$$

where *n* is the refractive index of the cell and *c* is the speed of light in vacuum.

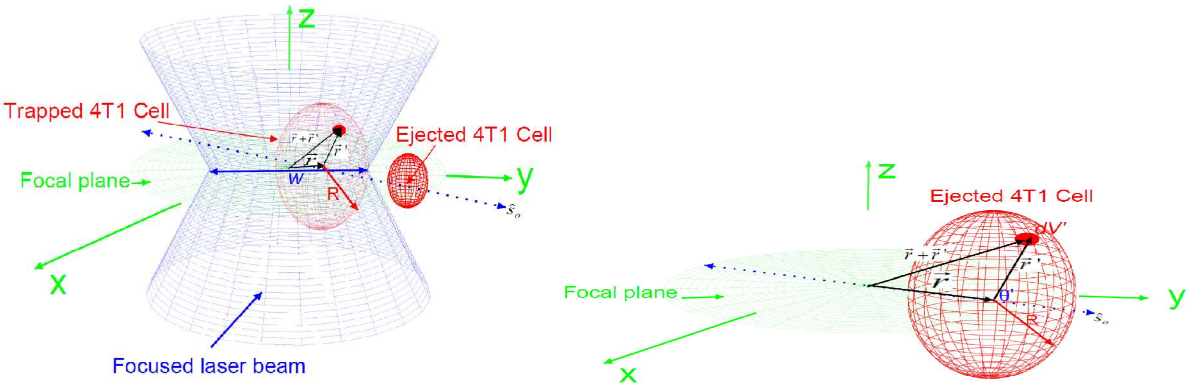

(a) (b)

Figure 4.9 (a) The blue double cone is a schematics for a focused linearly polarized laser beam along the direction $\hat{s}_o$ on the x-y plane and propagating along the z-direction. This beam has a diameter of *2w*, at the trap location. The red sphere represents a 4T1 cell before ejection (big) and after ejection (small). The vector $\vec{r}$ is the position of the center of the cell as measured from the center of the trap, $\vec{r}\,'$ is the position of an infinitesimal free charge, *dq'*, from the center of the cell. (b) A schematics for the position at a given instant of time for an ionized and ejected 4T1 cell along the direction of polarization $\hat{s}_o$, θ is the angle between the polarization direction and the vector $\vec{r}\,'$

It is important to note that the refractive index of the cell, n in Eq. (4.5) depends on time as the cell is undergoing dielectric breakdown due to the ionization taking place while the cell is in the trap. Suppose a free charge, *dq'*, has developed in an infinitesimally volume, *dV'*, of the cell which we can express in terms of the free charge density as,

$$dq' = \rho(\vec{r} + \vec{r}\,', t)dV', \qquad 4.6$$

and this charge has a velocity,

$$\vec{v}\,' = \frac{d\left(\vec{r} + \vec{r}\,'\right)}{dt} = \frac{d\vec{r}\,'}{dt} = v'\hat{r}\,'. \qquad 4.7$$

Note that we have neglected the change in position of the center of mass of the cell, $\vec{r}$, while the cell is in the trap. Then the Lorentz force on the total free charge that the cell possess can be determined using,

$$\vec{F}_e(\vec{r},t)=\int_V \rho(\vec{r}+\vec{r}\,',t)E(\vec{r}+\vec{r}\,',t)\left\{\hat{s}_o+\tfrac{nv'}{c}\left(\hat{r}'\times\hat{z}\times\hat{s}_o\right)\right\}dV'. \qquad 4.8$$

Next we shall make two physically valid approximations. First the speed of the free charge, *v'*, is negligibly small compared to the speed of light, *c*, and therefore we neglect the magnetic contribution to the Lorentz force. The second approximation that we make is for the time dependent charge density $\rho(\vec{r},t)$. suppose the time laps from the moment the cell gets trapped to the moment it got ejected is *T*. During this time significant amount of the free charge is created when the membrane is significantly ruptured and this happened at time $t=t_0$. If we neglect the free charge developed prior and after this time and represent the total charge on the cell by q_a at the position of its center of mass, $\vec{r}$, we may approximate the charge density using the Dirac-Delta function,

$$\rho(\vec{r}+\vec{r}\,',t)=q_o\delta(\vec{r}^{\,'}-\vec{r})T\delta(t-t_0). \qquad 4.9$$

Then the time average Lorentz

$$\vec{F}_e(\vec{r})=\tfrac{1}{T}\int_0^T\vec{F}(t)dt, \qquad 4.10$$

under these two approximations

$$\vec{F}_e(\vec{r})=\left(q_o\int_v\int_0^T E(\vec{r}+\vec{r}\,',t)\delta(\vec{r}\,'-\vec{r})\delta(t-t_o)dV'dt\right)\hat{s}_0, \qquad 4.11$$

becomes

$$\vec{F}_e(\vec{r})=q_oE_o\left(2\vec{r},t_0\right)\hat{s}_o. \qquad 4.12$$

For a Gaussian Electromagnetic wave propagating along the positive z-direction the electric field can be expressed as

$$E(2\vec{r},t_0)=E_o\exp\left[-\tfrac{r^2}{w^2}\right]\exp\left[-i\left(kz-\omega t_0\right)\right] \tag{4.13}$$

where w is the beam radius at the trap location. For the post-ionization dynamics, we set the initial time at $t=t_0=0$, the center of mass of the cell at this initial time be at the origin, and assume the cell remains confined to the x-y plane throughout its post-ionization motion so that, z=0. Then setting these values in Eq. (4.13) and substituting the resulting equation into Eq. (4.12), one finds for the electrostatic force

$$\vec{F}_e(\vec{r})\simeq q_oE_o\exp\left(-\tfrac{r^2}{w^2}\right)\hat{s}_o. \tag{4.14}$$

The amplitude of the electric field, E_0, can be determined from the power, P, measured at the trap location, using

$$E_o=\sqrt{\tfrac{2P}{A\epsilon_2 v}}=\sqrt{\tfrac{2Pv\mu_o}{A}}, , \tag{4.15}$$

where μ_o is the magnetic permeability of a free space, v is the speed of light in the medium that the cell is suspended in, and $A=\pi w^2$ is the beam size at the trap location determined from the beam radius at the back of the objective lens and it's numerical aperture [1.25].

The drag force: As we saw in Figure 1b, the 4T1 cancer cells are modeled spherical in shape with radius, R, and the drag force can be determined using

$$\vec{F}_d=6\pi\mu R\frac{d\vec{r}}{dt}, \tag{4.16}$$

where μ is the viscosity of the fluid that the cell is suspended in, which is FBS.

Trapping force: In estimating the trapping force on the cell, we use electromagnetic energy change in the region occupied by the cell. To this end, let's consider a cell (a dielectric sphere) with radius R. After the cell is ejected, as shown in Figure 4.9(b), let the position of the center of mass of the cell from the center of the trap, assuming the cell is confined on the x-y plane, be $\vec{r}$ which is directed along the direction of polarization of the field, $\hat{s}_o$. We consider an infinitesimal volume, *dv'*, inside this cell at a position, $\vec{r}\,'$, that makes and angle θ' as measured relative to the direction of the vector , $\hat{s}_o$ as shown in Figure 4.9 (b). Then electric field of a Gaussian laser beam propagating along the z-direction at the position of the infinitesimal volume can then be expressed as

$$\vec{E}(r, r', \theta') = E_o e^{-\left(\frac{r_h^2}{w_o^2} + \frac{z^2}{w_o^2}\right)} \hat{s}_o \qquad 4.17$$

where $r_h = r + r'\cos\theta'$

$$\vec{E}(r, r', \theta') = E_o \exp\left[-\tfrac{1}{4w^2}\left(r^2 + 2rr'\cos\theta' + r'^2\right)\right]\hat{s}_o, \qquad 4.18$$

where E_o is the amplitude of the field which was calculated from the power and w is the beam radius of the laser at the trap location.

As we stated earlier, we are interested in finding the trap force using the electromagnetic energy change in the micro space occupied by the cell. Thus, one must find the energy before and after the cell is exposed to the laser field. In the micro volume, *V,* with electrical permittivity constant, ε_b, (space which later be occupied by the cell), the electric field and the corresponding electric displacement of the laser field were $\vec{E}(r, r', \theta')$ and $\vec{D}(r, r', \theta')$, the electromagnetic energy in this volume of space, W_b, can be determined using

$$W_b = \frac{1}{2}\int \vec{E}(r, r', \theta') \bullet \vec{D}_b(r, r', \theta') dV'. \qquad 4.19$$

Similarly, the energy after the cell, with electrical permittivity constant, ε_a, occupying this same volume of space,

$$W_a = \frac{1}{2}\int \vec{E}(r,r',\theta')\bullet\vec{D}_a(r,r',\theta')dV'. \qquad 4.20$$

Then the change in electromagnetic energy in the micro volume, V, occupied by the cell is given by,

$$\Delta W = W_a - W_b = \left(\varepsilon_a - \varepsilon_b\right)\frac{1}{2}\int E^2(r,r',\theta')dV', \qquad 4.21$$

where we used, $\vec{D} = \varepsilon\vec{E}(r,r',\theta')$, for a linear medium. Then using the electric field in Eq. (4.18), one can write

$$\Delta W = \frac{1}{2}\left(\varepsilon_a - \varepsilon_b\right)E_o^{\,2}\int_0^R\int_0^\pi\int_0^{2\pi}\exp\left[-\tfrac{1}{4w^2}\left(r^2 + 2rr'\cos\theta' + r'^2\right)\right]r'^2\,dr'\sin\left(\theta'\right)d\theta' d\varphi'. \qquad 4.22$$

Upon integrating this equation, we find

$$\Delta W = \left(\varepsilon_a - \varepsilon_b\right)\pi E_o^2\frac{w^3}{2}\left[-\frac{w}{r}\left(e^{-\frac{(r_t+R)^2}{2w^2}} - e^{-\frac{(r_t-R)^2}{2w^2}}\right) + \sqrt{2\pi}\left(Erf\left[\tfrac{1}{w}\left(R+r\right)\right] + Erf\left[\tfrac{1}{w}\left(R-r\right)\right]\right)\right]. \qquad 4.23$$

The trapping force given by

$$\vec{F} = -\nabla_r\left(\Delta W\right), \qquad 4.24$$

using Eq. (20) is found to be

$$\vec{F}_T\left(r\right) = -8\left(\varepsilon_a - \varepsilon_b\right)\pi\frac{E_o^2 w^4}{r^2}e^{-\frac{\left(r^2+R^2\right)}{2w^2}}\left[\frac{Rr}{w^2}\cosh\left(\frac{Rr}{w^2}\right) - \sinh\left(\frac{Rr}{w^2}\right)\right]\hat{r}, \qquad 4.25$$

or in terms of the refractive indices of the cell ($\varepsilon_b = \varepsilon_0 n_b^{\,2}$) and the medium ($\varepsilon_a = \varepsilon_0 n_a^{\,2}$) that the cell is suspended as µ

$$\vec{F}_T\left(r\right) = -8\left(n_a^{\,2} - n_b^{\,2}\right)\varepsilon_0\pi\frac{E_o^2 w^4}{r^2}e^{-\frac{\left(r^2+R^2\right)}{2w^2}}\left[\frac{Rr}{w^2}\cosh\left(\frac{Rr}{w^2}\right) - \sinh\left(\frac{Rr}{w^2}\right)\right]\hat{r}. \qquad 4.26$$

The refractive index for the cell ($n_a=1.545$) is higher than that of the medium ($n_b=1.33$) and the trapping force is an attractive force.

4.2.2 Results and discussion

A sample of selected successive images of the cell describing the post ionization trajectory of the cell is shown in Figure 4.10. The horizontal red line connects the trapping point of the successive images. After the cell is ejected from the trap, its trajectory follows the polarization direction of the trapping laser for a perfectly aligned trap, which is shown by the green line. This trajectory is defined by the trap, the drag, and the electrical forces acting on the cell according to Eq. (4.4). For the post-ionization dynamics, we are interested in two electrical properties for the 4T1 cells in the untreated control, 2 h and 24 h treated groups. These are the net charge developed on the cell and the refractive indices change due to the dielectric breakdown resulting from the ionization of the cells. We use two different approaches to study these properties. In the first approach, we determine both the charge and the refractive indices of each cell. In the second approach, we determined only the charge based on two assumptions for the refractive indices of the cells. In the first assumption we considered negligible change for the refractive indices and in the second assumption we used the refractive indices we determined in the first approach.

Figure 4.10 The motion of the ejected cell.

4.2.2.1 First approach:

The post-ionization displacement of the 4T1 cells for the three groups as a function of time is shown in Fig. 4.11. Based on the average maximum displacement and also on the average size of the cells traveled, we shall make an approximation to the electrostatic force in Eq. (4.14) and the trapping force in Eq. (4.26). The average measured radius of the 4T1 cells is $R \simeq 8.2\mu m$ and the average measured maximum displacement is less than $r \simeq 50\mu m$ (see Figure 4.11).

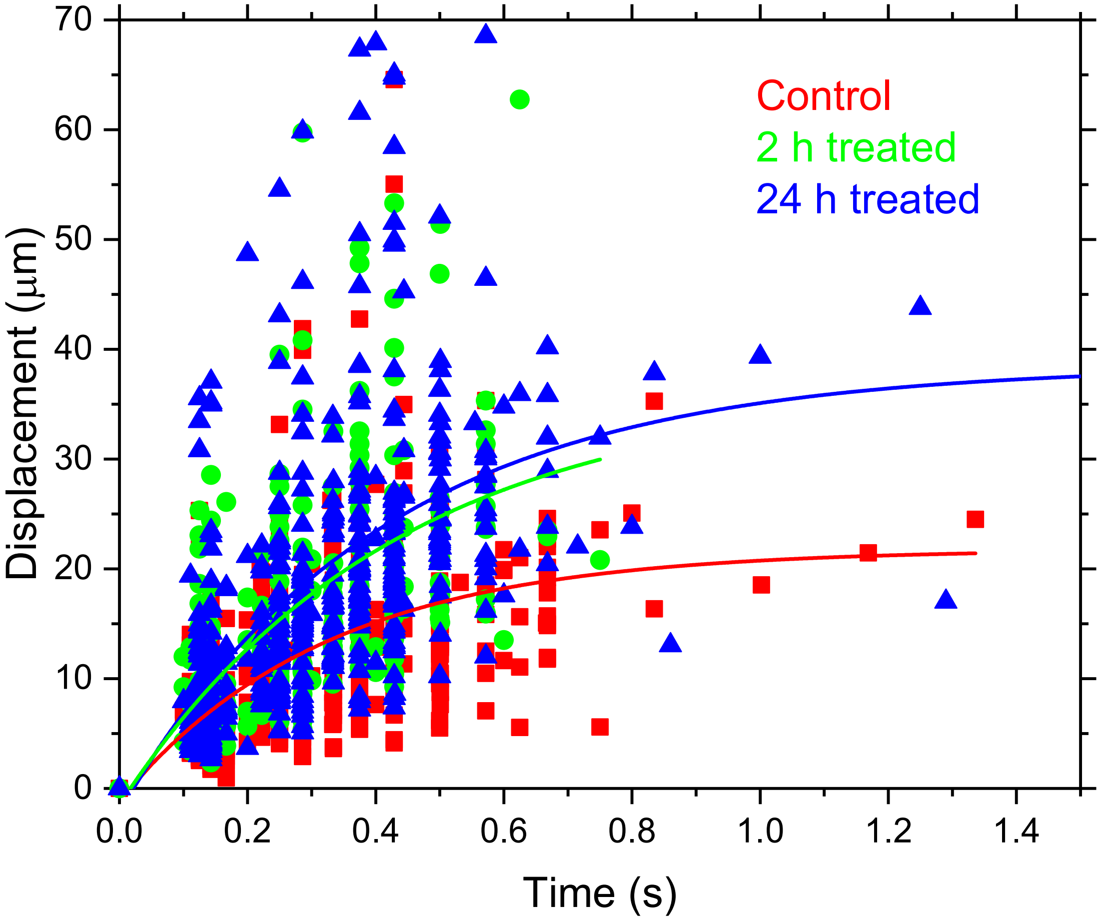

Figure 4.11. The radial displacement, r, as function of time.

On the other hand, the beam radius calculated at the trap location using this average size of the cells is $w=282.26\mu m$. Using these values we found, $r^2/w^2 \simeq 0.03$, $Rr/w^2 \simeq 0.005 << 1$, and $(r^2+R^2)/w^2 \simeq 0.03$ so that applying the series expansions

$$e^{-x} = 1 - x + \frac{1}{2}x^3...., x\cosh(x) - \sinh(x) = \frac{1}{3}x^3 + \frac{1}{30}x^5...., \qquad 4.27$$

In Eq. (4.14) and (4.26), by keeping only the first order terms, we can make the approximations for the electrostatic force

$$\vec{F}_e(\vec{r}) \simeq q_o E_o \hat{s}_o \tag{4.28}$$

and for the trapping force

$$\vec{F}_t\left(r\right) = -kr\hat{s}_0, \tag{4.29}$$

where

$$k = 8\pi R^3\left(n_a{}^2 - n^2{}_b\right)\varepsilon_o\left(E_0 / w\right)^2 / 3, \tag{4.30}$$

is a constant that depends on the electric field amplitude at the trap location (or the power), the beam radius, the radius of the cell and the difference in the refractive indices between the cell and the medium. The equation of motion for the cell in Eq. (4.4), using the results in Eq. (4.16), (4.28) and (4.29), can then be written as

$$\frac{d^2r}{dt^2} + 2\gamma\frac{dr}{dt} + \omega^2 r(t) = \frac{q_0 E_o}{m}, \tag{4.31}$$

where

$$\gamma = 3\pi\mu R / m \tag{4.32}$$

and

$$\omega = \sqrt{8\pi E_0{}^2\left(n_a{}^2 - n^2{}_b\right)R^3\varepsilon_o / 3mw^2}. \tag{4.33}$$

equation (4.31) describes an electrically driven damped harmonic oscillator. Under the approximation that the cell has no initial velocity and is positioned at the center of the trap, the solution to Eq. (4.31) is given by

$$r(t) = \left(qE_o / m\omega^2\right)\left\{1 - \exp(-\gamma t)\left[\cosh\left(\sqrt{\gamma^2 - \omega^2}\,t\right) + (\gamma / \sqrt{\gamma^2 - \omega^2})\sinh\left(\sqrt{\gamma^2 - \omega^2}\,t\right)\right]\right\}. \tag{4.34}$$

as we can see in Fig. 4.11, the post ionization trajectory of the cells must be characterized by an over damped harmonic oscillator, which therefore requires $\gamma^2 \geq \omega^2$. Due to the ionization from the radiation damage, the cell underwent a structural change that in turn caused an electrical susceptibility change. This leads to a new lower refractive index, $n < 1.545$, that must be greater than the refractive index of the surrounding medium (FBS, $n_b \simeq 1.33$). In order to find this new refractive index and the total free charge, first the maximum value, $\omega_{max} = \gamma$, was determined using the values for m and R for each cell and μ for FBS [$1.02 \mathrm{x} 10^{-3}$ Ns/m]. The electric field amplitude, $E_o = 42.72\ kV/m$, determined from the measured power and the beam radius, $w = 282.26 \mu m$ at the trap location. The numerical model fitting function NonlinearModelFit in Mathematica was used to fit Eq. (4.34) to the displacement versus time data shown in Fig. 4.11 for each cell. The NonlinearModelFit function started looking for the charge, q, and the refractive index, n, at several orders of magnitude below, n_{max}. The results for q measured by the z-number ($z = q/(1.6 \times 10^{-19}\ C)$) and n are shown in Fig. 4.12.

The average z number for control, 2h treated and 24h treated are 119.86±92.30, 149.53±111.03 and 168.05±114.60 respectively. And also the refractive index of these three groups were determined to be 1.39±0.04, 1.37±0.04 and 1.35±0.03 respectively. The average charge increase as the period of treatment increase however, the refractive index decreases as the treatment period increase since the charge and refractive index are inversely proportional. Larger period of treatment has larger charge and smallest refractive index.

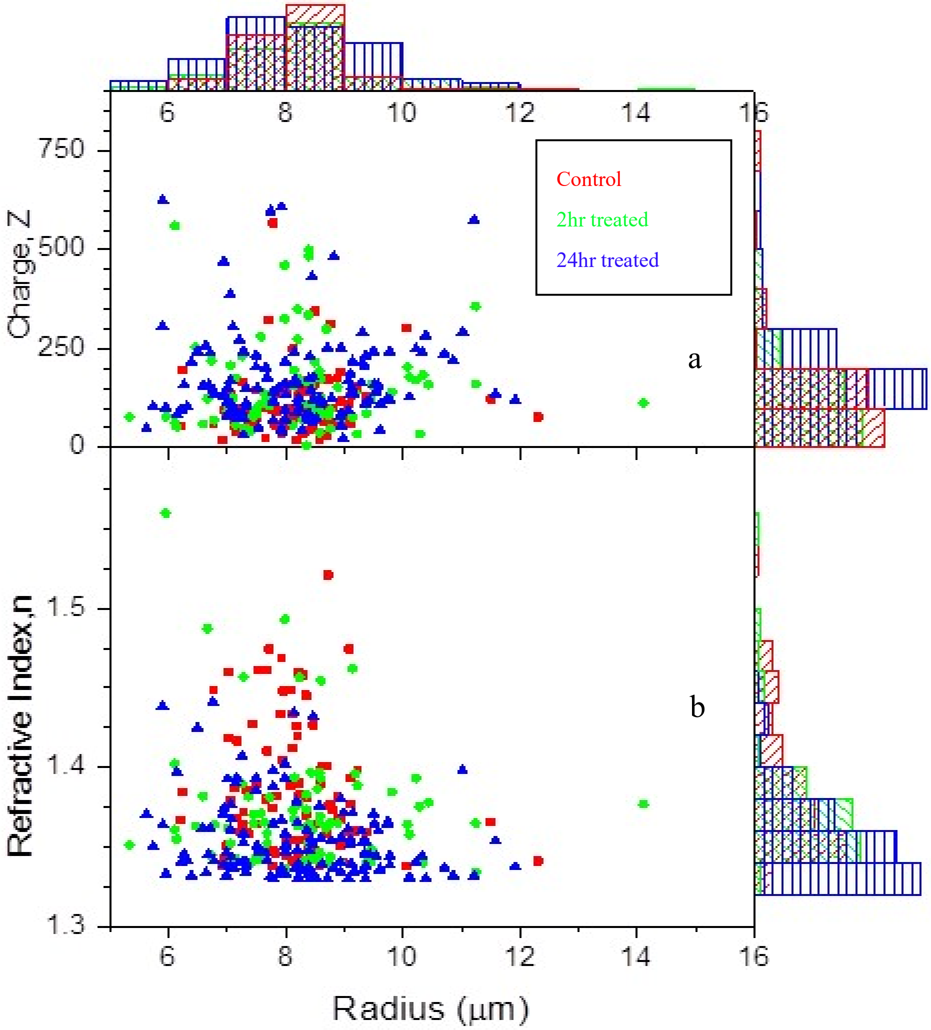

Figure 4.12. The calculated charge (a) and refractive index (b) vs size measured by the radius for each cell along with the corresponding distributions displayed using histograms: control (red), 2-h treated (green), and 24-h treated (blue). The charge is measured by the z number

Figure 4.12 shows the z-number vs radius and refractive index vs radius for the whole data of the control, 2h treated and 24h treated groups. The charge and the refractive index vs radius are not clearly show the difference between the three groups thus we use the data reduction method to explain the variance among them.

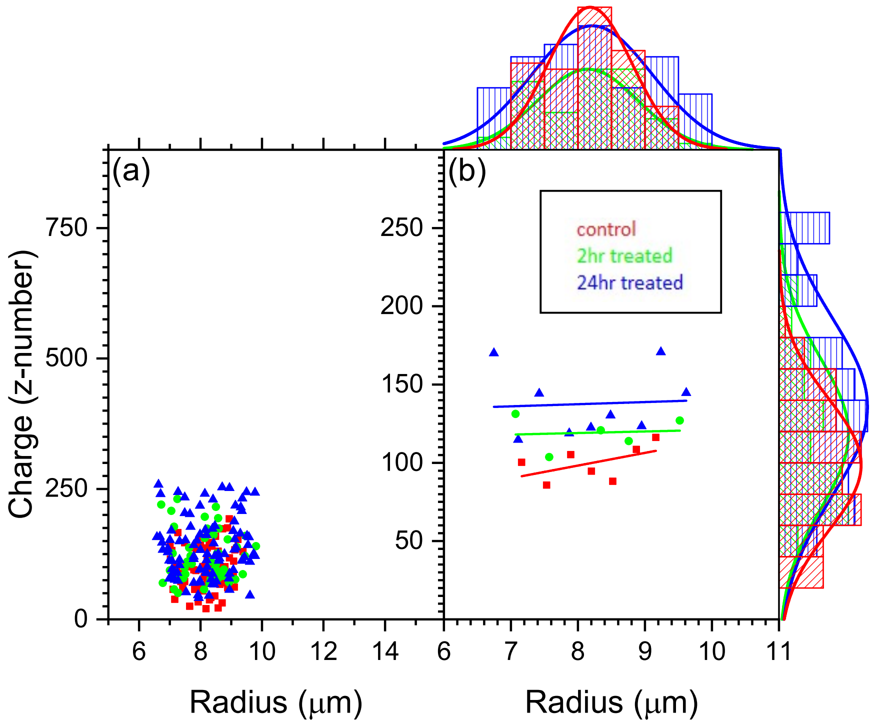

Figure 4.13. Reduced data for the charge vs R: control (red), 2-h treated (green), and 24-h treated (blue). The charge is measured by the z number.

In Figure 4.14b the charge of the three groups clearly shows that the charge of control (red) is smallest and 24h treated (blue) is largest. The treatment makes the cell sensitive to ionize and when the treatment period increases the cell becomes more sensitive. More sensitive cells developed larger charge hence the untreated cells have smaller charge than the treated one. When the breakdown of the cell membrane increases the conductivity and charge density increases. This result is in conformity with Golombeck, Penman and Hao [117-119] who have observed that the relation between the electric permittivity and conductivity of materials, when the conductivity of material increases it permittivity decreases. Stogryn, A [120] showed that when the temperature of the sodium chloride solution increased, the dielectric constant also decreased which supports our result. Finally, we confirm that the charge and refractive index has inverse relationship.

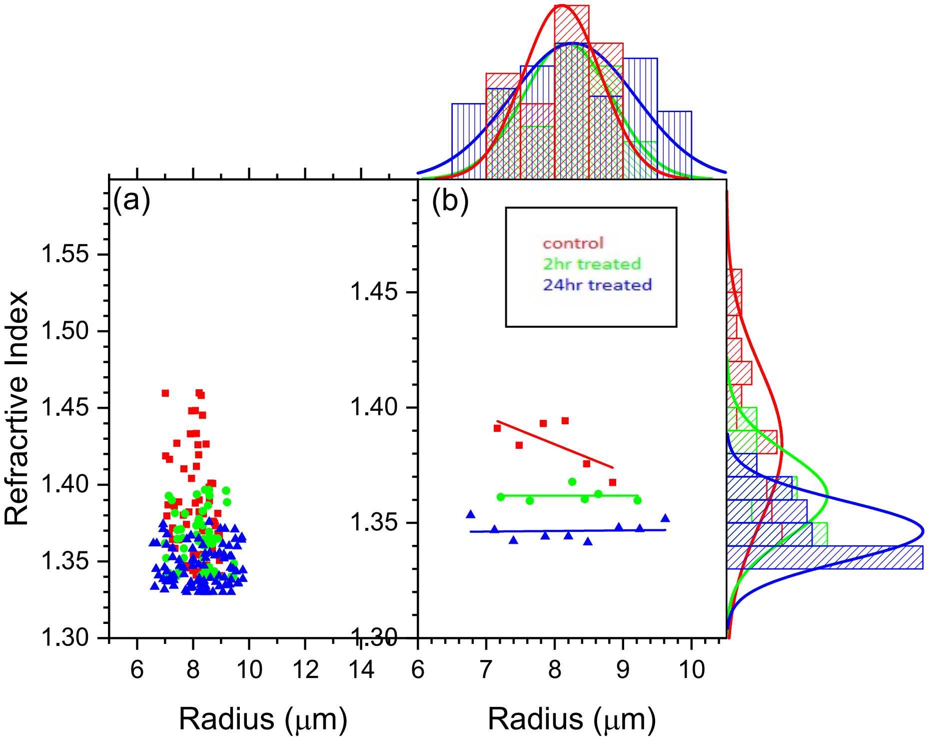

Figure 4.14. Reduced data for the refractive index vs R: control (red), 2-h treated (green), and 24-h treated (blue). The charge is measured by the z number.

The distribution of the size of the cell shown at the top axis of Figure 4.15 does not show significantly different but the distribution of the refractive index shown in the left side display the pick of the distribution shift up. This means, generally, the reduced data seams to predict the refractive index decrease with increasing period of treatment. However, the variation in the refractive index due to the variation in size of the cells seems to be negligible in particular for the treated groups.

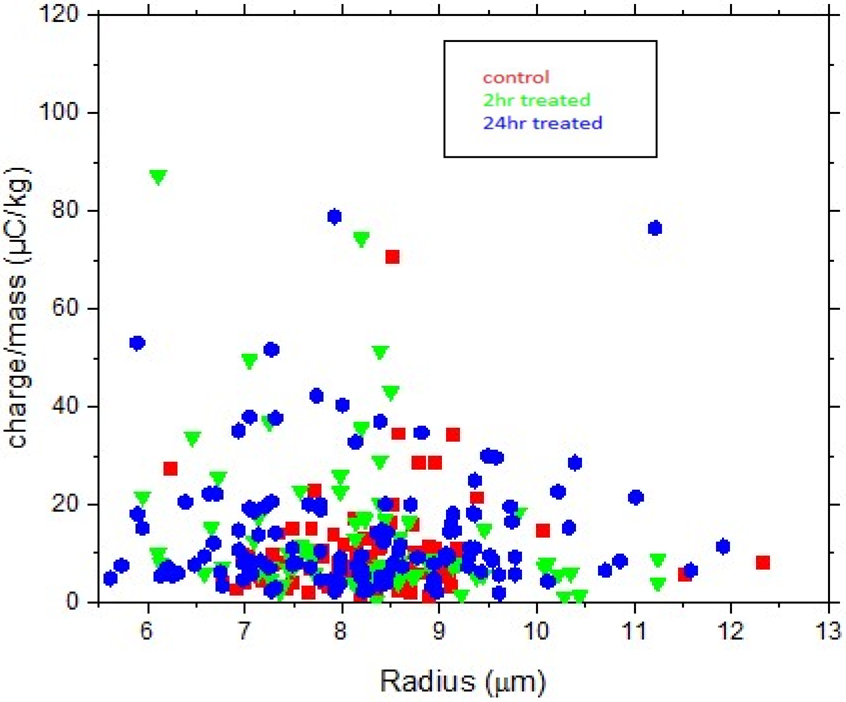

Figure 4.15. The calculated charge per unit mass vs size measured by the radius of each cells along with the corresponding distributions displayed using histograms: control (red), 2-h treated (green), and 24-h treated (blue).

The data shown in the Figure 4.15 displays the charge to mass ration ratio vs the size of each 4T1 cells in the three groups. In order to see the effect of the treatment on the charge to mass ratio, we had carried out a similar statistically valid data reduction. Figure 4.16 (a) displays the reduced data obtained from Figure 4.15 by eliminating data points which are far off from the majority of the data for the values to the charge to mass ration and to the radius. For the radius value, three form the top and three from bottom for the control group, five from the top and five from the bottom for the 2 h treated, and nine from the top and nine from the bottom for 24 h treated were eliminated. Similarly, for the charge to the mass ratio values eliminated six maxima and three minima for control groups, seven maxima and five minima for 2h treated and three maxima and three minima from 24 h treated groups. This reduced data, which is displayed in Figure 4.16 a, is then further sorted by the radius in ascending order and sub-grouped. The calculated average for the charge to mass ration and the corresponding radius for each subgroup is displayed in Figure 4.16b

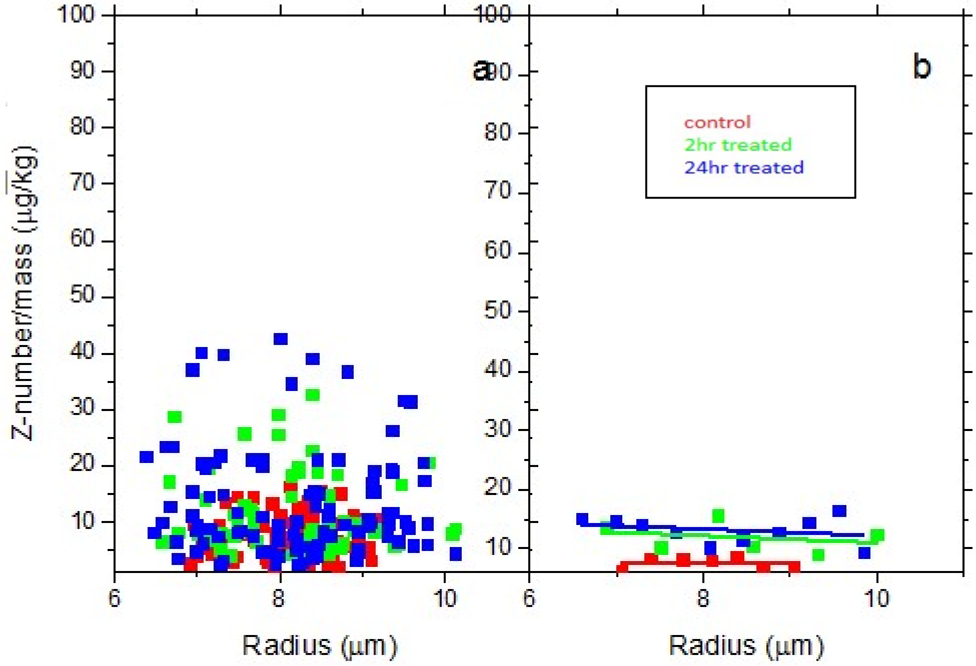

Figure 4.16. Reduced data for the charge/mass vs Radius: control (red), 2-h treated (green), and 24-h treated (blue). The charge is measured by the z number.

These results showed in Figure 4.16 (b) shows that the charge to mass ratio is higher for the treated groups as compared to the control group. However, the results seem to predict negligible change in the charge to mass ration due the change in the size of the cell.

The charge and the refractive indices determined for the three groups have also be analyzed in relation to the threshold ionization energy (TIE) and threshold radiation dose (TRD) that we have analyzed in detail in the previous section. The results are displayed in Figure 4.18.

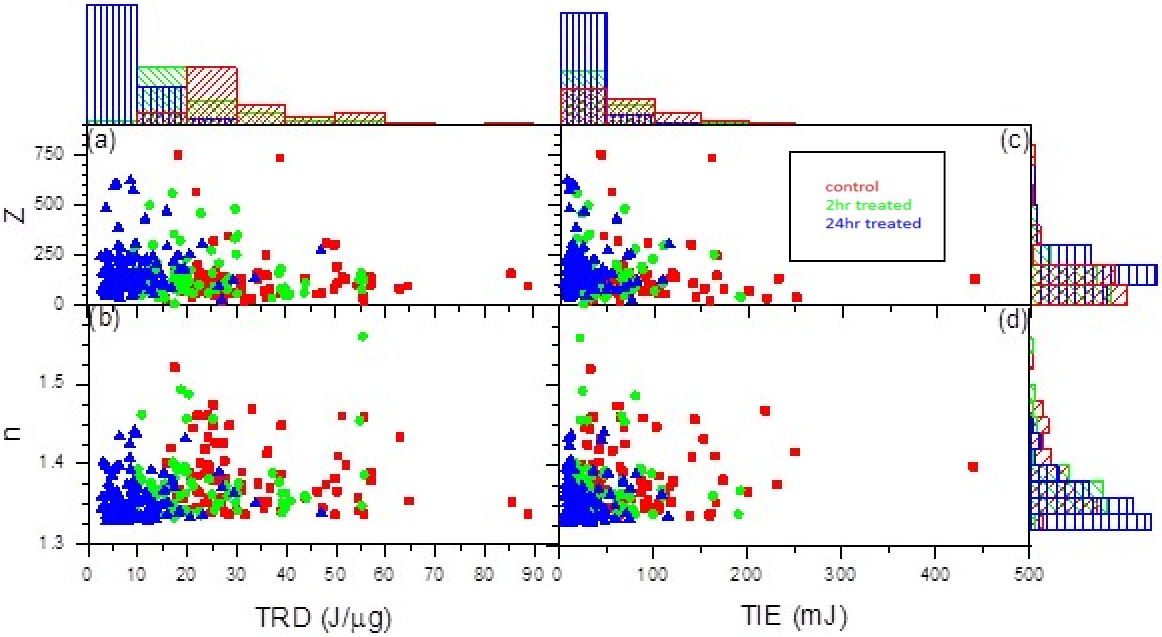

Figure 4.17 The calculated charge and refractive index vs TRD (a) & (b) vs TIE (c) and (d) along with the corresponding distributions displayed using histograms: control (red), 2-h treated (green), and 24-h treated (blue). The charge is measured by the z number.

The z number versus TIE in shown in Figure 4.17 a & b and versus TRD in Figure 4.17 c & d for the untreated, 2- treated and 24-h treated using the same color coding. Clearly these graphs show a decrease in TRD as the treatment period increases which we already discussed in details in section 4.2.1. However, it seems hard to predict the relationship between charge and TRD or refractive index and TRD. Thus, it is necessary to make further analyses by making a similar data reduction we used previously. The reduced data displayed in the Figure 4.18 (c) obtained from Figure 4.17 (a) first sorted by TRD in ascending order and eliminating the top four for the control untreated, the top six and five for the 2 h and 24 h treated, respectively. And then we sorted this reduced data by z-number in increasing order and removing seven maxima and one minima for control groups, ten maxima from 2h treated and eight maxima from 24h treated groups. Finally using origin pro the average for each subgroup were calculated and the resulting data for z vs TRD is shown in Figure 4.18 (d). According to the result in Figure 4.18 (d), the z-number is larger for longer period of treatment.

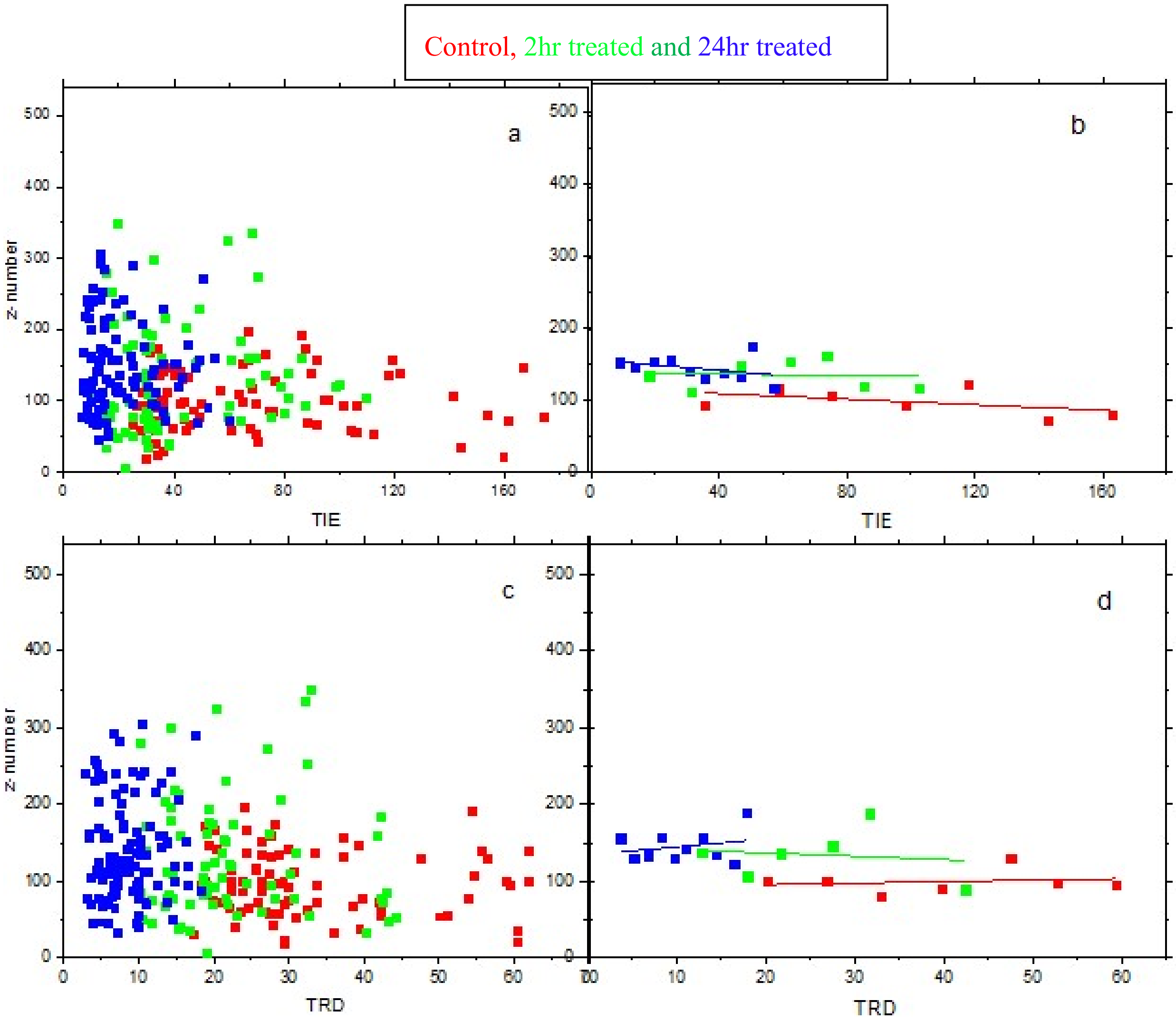

Figure 4.18 The calculated charge vs TRD (a) & (b) vs TIE (c) and (d) along with the corresponding distributions displayed using histograms: control (red), 2-h treated (green), and 24-h treated (blue). The charge is measured by the z number.

This reduced data for the z number vs the TIE displayed in Figure 4.18 (a) was obtained from the data in Figure 4.17 (c) using a similar procedure where we eliminated those data points which are far off from the majority. The resulting data were also sorted by the TIE and sub-grouped so that the averages for each sub-group were calculated. The results obtained following this procedure is shown in Figure. 4.18 (b) and it clearly indicate that the treated 4T1 cells develop higher as compared to the untreated control group.

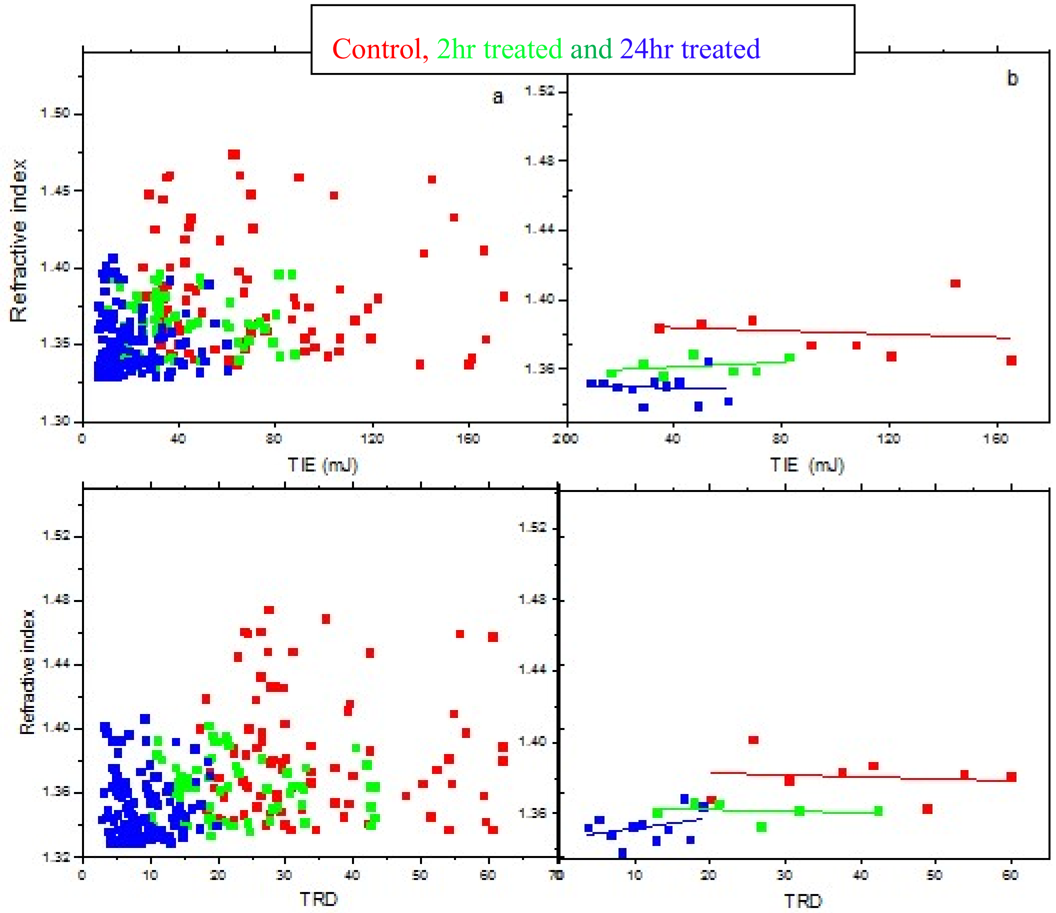

Figure 4.19. The calculated refractive index vs TRD (a) & (b) vs TIE (c) and (d) along with the corresponding distributions displayed using histograms: control (red), 2-h treated (green), and 24-h treated (blue). The charge is measured by the z number.

We have also made further analyses for the refractive index versus TIE (Figure. 4.17 (d) and TRD (Figure 4.17 (b)) for all the 4T1 for the control untreated, 2 h and 24 h treated groups that is based on a similar data reduction procedure. The results are shown in Fig. 4.19. The results, unlike the charge, the refractive indices for the treated 4T1 cells displays lower values as compared to the untreated control group. This characteristic of the refractive indices is common to both n vs TIE Figure 4.19 (b) and n vs TRD (Figure 4.19 (d)).

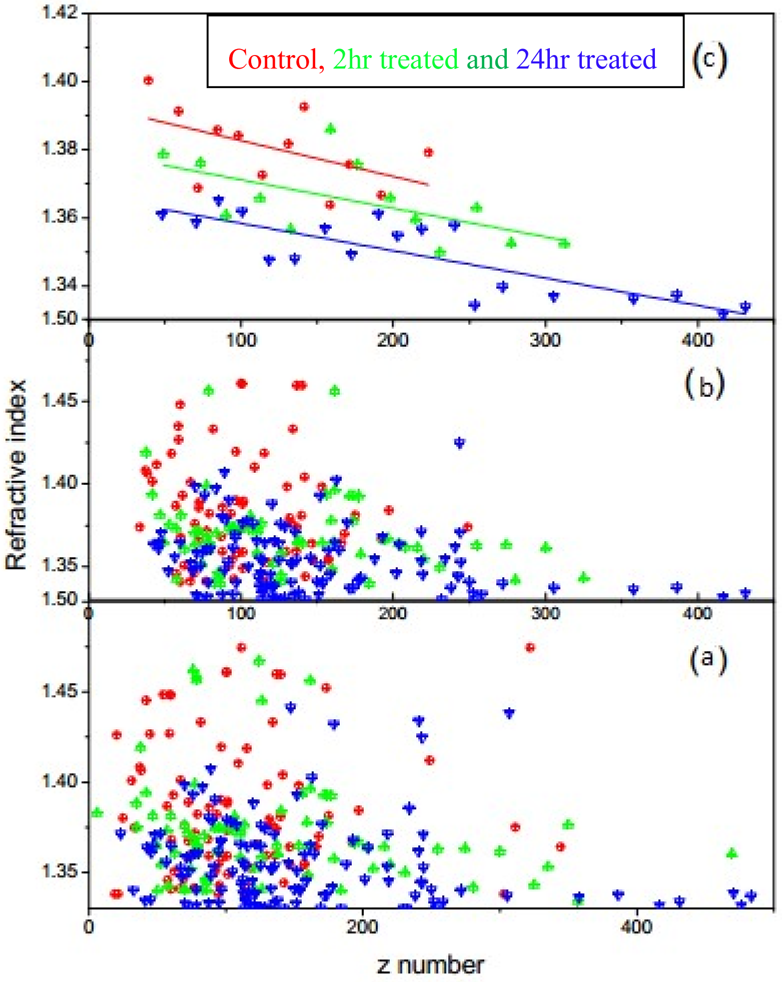

Figure 4.20. The refractive indices vs z number (a)-(c).

The charge and the refractive indices for the 4T1 cells determined from the post-ionization dynamics, whether the cells are treated or untreated, must show some correlation or dependency as both are a consequence of the membrane breakdown due to the radiation absorbed. Therefore it is worth examining the variation of the refractive indices with the charge which is displayed in Figure 4.20. Figure 4.20 (a) displays the refractive index versus charge of all 4T1 cells in the control untreated, 2 h treated and 24 h treated groups. The results in Figure 4.20 (b) and (c) displays the reduced data obtained using a similar procedure we discussed earlier. The result in Figure 4.20 (c) clearly shows the refractive index decrease as the charge on the cell increase.

4.2.2.2 Second approach

In the second method we use directly the displacement, velocity and acceleration and the refractive index of the cell (n_a) after ionization which is discussed in the first approach and the refractive index of the medium, n_b=1.33. Using these values for the trap force in Eq. (4.26), the electrostatic force in Eq. (4.14) and the drag force in Eq. (4.16), the equation of motion in Eq. (4.4) can then be written as

$$m\frac{d^2r}{dt^2} = q_o E_o \exp\left(-\frac{r^2}{w^2}\right) - 6\pi\mu R\frac{dr}{dt} - (n_a - n_b)\in_o \pi\frac{E_o^2 w^4}{r^2} e^{-\frac{\left(r^2+R^2\right)}{2w^2}}\left[\frac{Rr}{w^2}\cosh\left(\frac{Rr}{w^2}\right) - \sinh\left(\frac{Rr}{w^2}\right)\right], \quad \textbf{(4.35)}$$

The charge for the untreated samples is smaller from the treated ones. The charge determined by the NonlinearModelFit has an approximate value the charge calculated from the second approach.

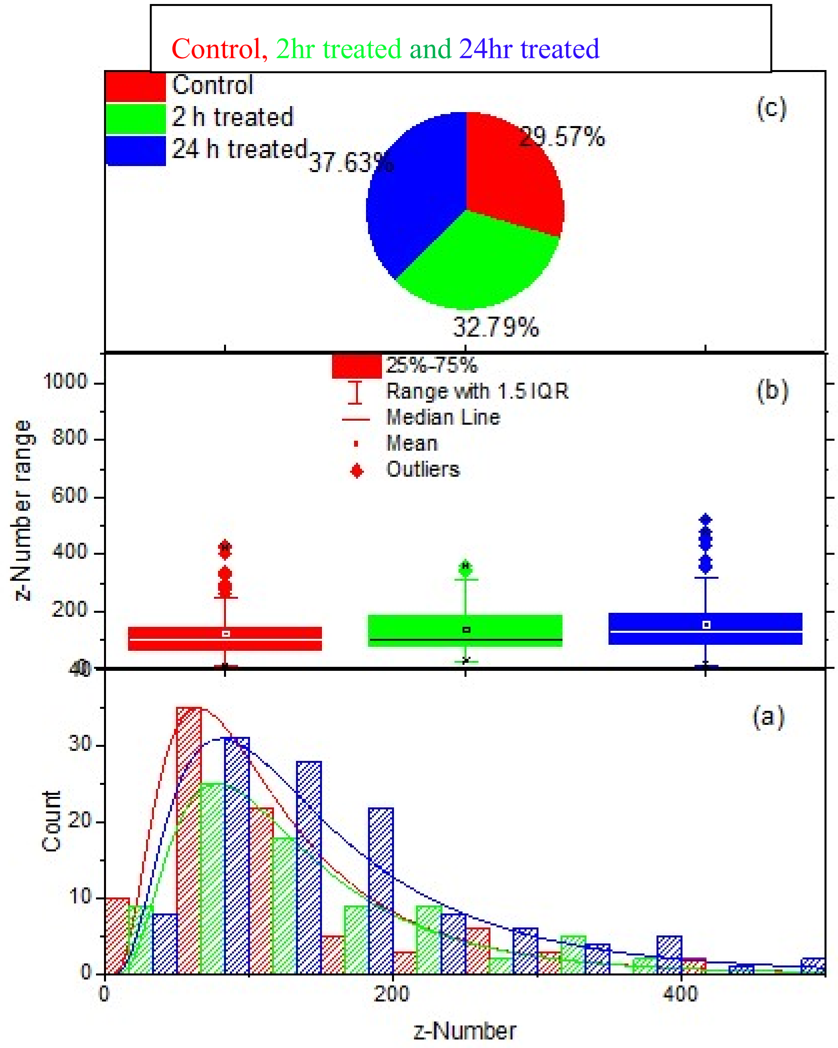

Figure 4.21 The statistical distributions for the charge measured by the z-number (a-c) and refractive index (d-f): control (red), 2-h treated (green), and 24-h treated (blue).

The charge measured in terms of z number by dividing the charge developed on the cell to the electron charge. The average charge in z-number calculated using Eq.4.35 was 124.4±88.55, 137.97± 86.29, 158.35± 101.80. The pie chart in Figure 4.21 (b) shows the charges developed on cells are 29.57 %, 32.79 %, and 37.63% for untreated, 2-h treated and 24-h treated. The histogram also shows the average values shifted to the right as the treatment period increased. The relation between the charge and treatment time for each the three groups tell the radio sensitivity of the cancer cells increase by the DMDD treatment.

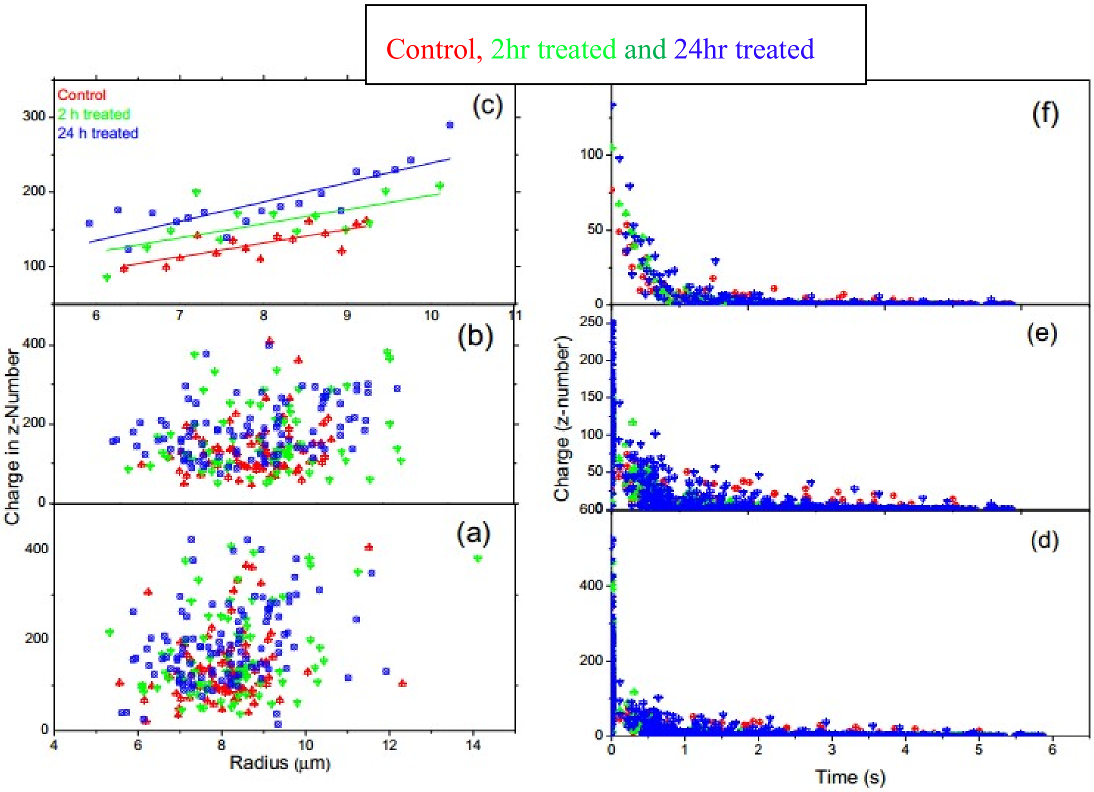

Figure 4.22. z number versus radius (a-c) and the charge of the ejected cell as function of time.

The data distribution of the whole untreated, 2- treated and 24-h treated data for the three groups Fig. 4.22 (a) displays the data reduction first sorted by radius in ascending order and eliminated three from the top and bottom and then sort by charge in increasing order and deleted three from the minimum and maximum. Finally, Figure 4.22 (c) shows the reduced data displayed in (b) resort by radius in ascending order and reduced by grouping with 0.20 x- increments by Origin Pro. As clearly shows in the Figure 4.22(c) the charge increases as the radius of the cell increases. In the Fig. 4.22 (d) display the charge as function of time for each individual cell of untreated, 2h treated and 24h treated. In the Figure 4.22 (f) we sort by charge and removed the charge of three cells from the top and bottom and then the data reduction by grouping was done by sorting in time and which is clearly shows the charge on the cell decrease after ejection as the time increase. The decreasing of charge on the cell is due to the interaction of cells with the environment outside the trap.

4.2.3 Discussion

As mentioned in chapter 3, TIE increases as the size of the cell increased since the trans-membrane voltage is proportional to the TIE. Zimmermann [121] observed that the value of induced trans-membrane voltage depends on the cell size, shape, and the position of the cell with respect to the direction of applied electric field which supports our result. M. Pasquerilla [25] found that the ionization energy (IE) calculated at 0.345W incident power for RBC had average TIE for single cell as 900+/-500 mJ which is greater than our result. It may be argued that M. Pasquerilla used incident power to calculate TIE M. Kelley [23] showed that the ionization energy has positive correlation with the size of the cell. Larger cell spends longer time in the trap than the smaller one hence TIE is larger for larger cell than the smaller cells.

The multi cell ionization energy increments were in small steps and radiation doses dropped rapidly as the number of cells increased in the trap. The decreasing effects of radiation dose were due to the mechanical and dipole-dipole interaction of nearby cells in addition to the applied field.

When two biological cell membranes approach one another they simultaneously experience many different interactions. These interactions include in large and short range separation, the long range interaction include attractive force acting on the intervening aqueous space and short-range interaction involving molecular contact between components Rand [122]. The interaction between the two membranes can contribute to their destabilization due to an increase in the intra-membrane electric field strength Dimitrov [123].

Numerical simulation result shows variations in the intracellular and extracellular electric field which is due to the cell-to-cell interactions, superposition of individual electric fields generated by equivalent dipole moments. Vanegas Acosta [124]. The experimental and numerical simulation results obtained are in agreement with our result the interaction between cells decrease the TIE and TRD.

Chapter Five

In this chapter we will study the elastic property of sickle cell trait and sickle cells anemia. Sickle cell trait is RBC gene constructed from one normal (HbAA) and one sickle cell (HbSS) genes. Sickle cell trait is person who inherited one sickle gene from one of the parents but they are carrier not sickle cell anemia patients. Sickle cell anemia patients inherit sickle genes (HbSS) from both parents. In this chapter we will study the rigidity (stiffness) of sickle cell trait (SCT) and sickle cell patients (SCA) by compressing with trapping force and stretching by drag force. This study will be used as an initial point for researchers those will investigate the treatment of SCA to increase the elasticity of it and for medical doctors to prefer medicines for SCA patient.

5 Elasticity of SCT and SCA red blood cells

To study the elasticity of red blood cells, the blood samples were taken from the persons with SCA and SCT and the samples were diluted by the fetal bovine serum (FBS) in the ratio 1:1000. The diluted sample was put in a slide and mounted it on the piezo-driven stage (PS). Three snap shots were taken before the RBC being trapped. The RBC was trapped by the LT with the power of ~30 mW at the tip of the objective lens by opening the laser port for the laser beam. The cell was subjected to different magnitudes of drag force while it was being confined by the laser trap at a fixed power. We create drag force by setting the PS moves with a given velocity to sheer the trapped RBCs. During the period of PS movement, a live image of the cell was continuously captured by the CCD camera. The exactly same procedures were carried out on seven different RBC groups for both the SCA and SCT blood samples.

5.1 Trapping force

We consider a simplified physical model for the RBCs to determine the trap force which is proportional to the magnitude of the drag force. We model a RBC as a thin cylinder with radius, *R,* and thickness, t, where $t << R$. A RBC is predominantly made of polar water molecules with inherent unusually high dipole moment by Ernest Z Truong-Son N, $p = 6.1\times10^{-30}\,C.m$. In the absence of an external electric field the dipole moment of these polar molecules is randomly oriented and the total dipole moment per unit volume, the Polarization, $\vec{P}(\vec{r},t)$ is zero. Let's consider an infinitesimal volume dv' in the cell as shown in the Figure 5.1. Let the magnitude of the polarization in this infinitesimal volume be $d\vec{P}$ and the direction is $\hat{r}'$ from the positive z-axis. Suppose a laser beam that propagates along the z-direction and linearly polarized along the x-direction is turned on as shown in the Figure 5.1. The cell is due to the electric field of the laser, $\vec{E}(\vec{r},t)$, it experiences an electrical torque given by

$$\vec{N} = \iiint \vec{P}(\vec{r}\,',t)dV'\times\vec{E}(\vec{r}\,',t). \qquad 5.1$$

Let's assume there are N molecules in the cell the magnitude of the dipole moment be p. Then we may write the net torque on the cell resulting from turning the laser on can be approximated by

$$\vec{N} \simeq \frac{NpE}{V}\int_0^{2\pi}\int_0^{R}\int_{-t/2}^{t/2}(\cos(\varphi')\hat{x}+\sin(\varphi')\hat{y}+\hat{z})\times\hat{x}dz's'ds'd\varphi', \qquad 5.2$$

which leads to

$$\vec{N} \simeq NpE\hat{y}, \qquad 5.3$$

where we used for the volume of the cell, $V = \pi R^2 t$.

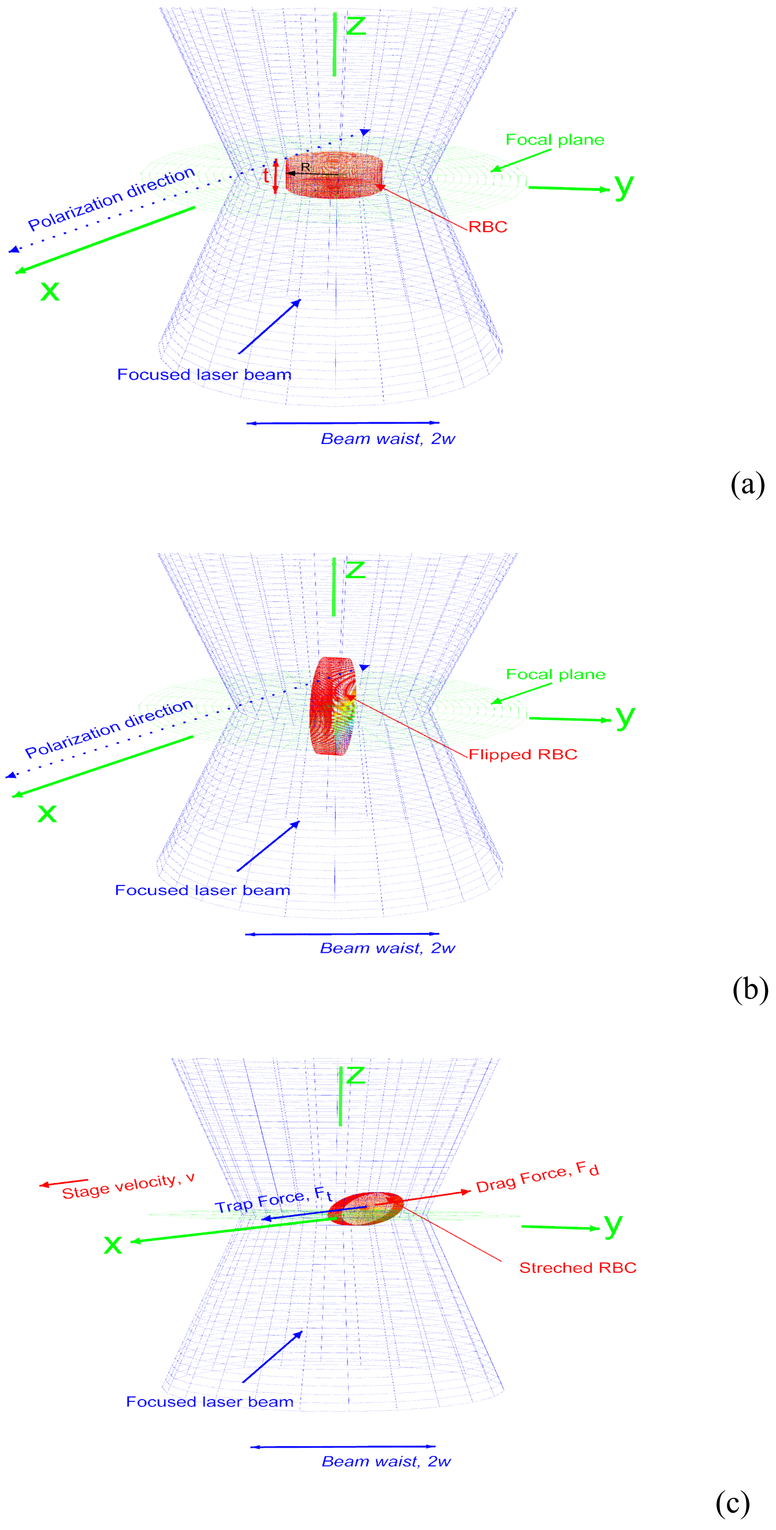

Figure 5.1 A simplified thin-cylinder model for a RBC; (a) before exposed to before the laser beam turned on; (b) when a linearly polarized laser beam propagating along the z-direction is turned on and the cell is trapped; (c) A cell acted upon by trap force and a drag force created by moving the stage with velocity v along the direction of polarization.

Because of this electrical torque, an RBC initially sitting at the bottom of the slide with its platelet side facing the x-y plane is forced to rotate about the y-axis and the cell remains trapped at a position in which its plat late side facing the x-z plane parallel to the beam propagation direction as shown in Fig. 5.1b. After the cell is trapped if one oscillates the staging with a constant velocity v along the polarization direction the cell experiences and a drag force equal in magnitude but opposite indirection to the trap force as shown in Figure 5.1 (c).

Next, we determine the trap force when the cell center of mass is moved from the center of the trap and the cell is stretched due to the two opposing drag and trap forces. To this end we note let the electric field of the laser beam be, $\vec{E}(\vec{r},t)$. Due to this electric field the polarization inside the cell be $\vec{P}(\vec{r},t)$. Then for an RBC with center of mass position at $\vec{r}$ as measured from the center of the trap located at the origin as shown in Figure 5.2, the trap force can be obtained from

$$\vec{F} = \int \left(\vec{P}(\vec{r}+\vec{r}\,') \cdot \nabla' \right) \vec{E}\,(\vec{r}+\vec{r}\,') dV' . \qquad 5.4$$

Due to the electrical toque in the bipolar water molecules, when the cell is trapped, as shown in Figure 5.1 (b), the axis of cell becomes normal to the polarization direction of the laser beam. This essentially creates a positive on one side and negative bound surface charges on the other side. This is a physically reasonable approximation comparing the beam radius, w, of the laser beam at the trap location with the average radius of a human RBCs, R. Since $R \ll w$, we can approximate a uniform electric field over the cell. A closer look at the trapped and dragged cell is shown in Figure 5. 2.

Suppose the total dipole moment due to the positive and negative bound surface charges on the two opposite sides of the cell is $\vec{p}_{Total}$ the electric field inside the cell can expressed as

$$\vec{E}_{net} = -\frac{1}{4\pi\varepsilon_0}\frac{\overrightarrow{p}_{Total}}{R^3} \tag{5.5}$$

Using the electric field inside a dielectric cylinder with an electrical permittivity ε placed in a region with electrical permittivity, ε_1 and an external electric field, $\vec{E}$

$$\vec{E}_{net} = \frac{\varepsilon - \varepsilon_1}{\varepsilon + \varepsilon_1}\vec{E} \tag{5.6}$$

one can write the total induced dipole moment as

$$\overrightarrow{p}_{Total} = -4\pi\varepsilon_0 R^3 \frac{\varepsilon - \varepsilon_1}{\varepsilon + \varepsilon_1}\vec{E} \tag{5.7}$$

and dividing this with volume of the RBC, $V=\pi\rho^2 t$, the polarization is,

$$\overrightarrow{P} = -\frac{4\varepsilon_0 R}{t}\frac{\varepsilon - \varepsilon_1}{\varepsilon + \varepsilon_1}\vec{E} \tag{5.8}$$

Introducing the refractive indices $n^2 = \varepsilon / \varepsilon_0$ and $n_1^2 = \varepsilon_1 / \varepsilon_0$ for the cell and the medium and also the parameter $m=n/n_1$, the polarization can be expressed as

$$\overrightarrow{P} = -\frac{4\varepsilon_0 R}{t}\frac{m^2 - 1}{m^2 + 1}\overrightarrow{E} \tag{5.9}$$

Now substitute Eq. (5.9) into Eq. (5.4) and yield, we find

$$\overrightarrow{F} = -\frac{4\varepsilon_0 R}{t}\frac{m^2 - 1}{m^2 + 1}\int\left(\overrightarrow{E}\cdot\nabla\right)\vec{E}\,dV \;. \tag{5.10}$$

Using the relation

$$\nabla\left(\overrightarrow{A}\cdot\overrightarrow{B}\right) = \overrightarrow{A}\times\left(\nabla\times\overrightarrow{B}\right) + \overrightarrow{B}\times\left(\nabla\times\overrightarrow{A}\right) + \overrightarrow{B}\left(\overrightarrow{A}\cdot\nabla\right) + \overrightarrow{A}\left(\overrightarrow{B}\cdot\nabla\right) \tag{5.11}$$

And noting that the electric field is irrotational, one can easily find

$$\left(\vec{E}\cdot\nabla\right)\vec{E} = \frac{1}{2}\left(\nabla\left(\vec{E}\cdot\vec{E}\right)\right) \tag{5.12}$$

and the force in Eq. (5.10) becomes

$$\vec{F} = -\frac{2\varepsilon_0 R}{t}\frac{m^2-1}{m^2+1}\int \nabla\left(E^2\right)dV \qquad 5.13$$

In terms of the intensity of the laser at the trap location

$$I = \frac{v\varepsilon_1}{2}E^2 = \frac{c\varepsilon_1}{2n_1}E^2 \Rightarrow E^2 = \frac{2In_1}{c\varepsilon_1}, \qquad 5.14$$

we may rewrite Eq. (5.13) as

$$\vec{F} = -\frac{4R}{ct}\frac{m^2-1}{m^2+1}\int\left(\nabla I\right)dV. \qquad 5.15$$

Upon taking the inner product of the force in Eq. (5.15) and the beam propagation direction $\hat{z}$, we may write

$$\vec{F}\bullet\hat{z} = -\frac{4R}{ct}\frac{m^2-1}{m^2+1}\int \nabla\bullet\left(I\,\hat{z}\right)dV \qquad 5.16$$

So that using the Divergence theorem,

$$\int \nabla\cdot\left(I\hat{z}\right)dV = \oint I\hat{z}\bullet d\vec{a} \qquad 5.17$$

Eq. (5.16) can be rewritten as

$$\vec{F}\bullet\hat{z} = -\frac{4R}{ct}\frac{m^2-1}{m^2+1}\oint I\hat{z}\bullet d\vec{a} \qquad 5.18$$

and there follows that

$$\vec{F} = -\frac{4R}{ct}\frac{m^2-1}{m^2+1}\oint I d\vec{a} = -\frac{4R}{ct}\frac{m^2-1}{m^2+1}\oint I da\,\hat{s} \qquad 5.19$$

$\hat{s}$ is the unit vector for the infinitesimal area da on the curved part of the cylinder (the RBC). There is no contribution from the platelate sides of the cell as they cancel each other.

We now proceed to evaluate the integral in Eq. (5.19). To this end, it is important to make a closer look at the stretched cell by the drag and trapping forces. This is shown in Figure. 5.2.

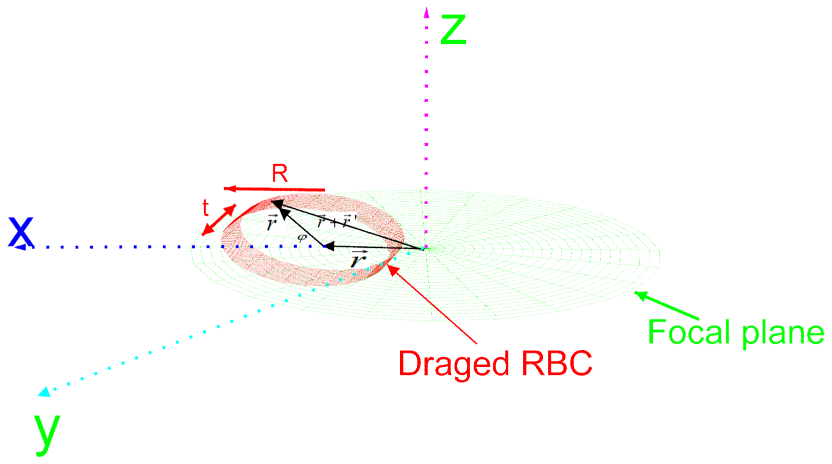

Figure 5.2 The dragged cell.

The intensity assuming to be Gaussian beam on at a point on the curved part of the cylinder can be expressed

$$I(r) = I_o \exp\left[-2\left((r+R\cos\varphi)^2 + R^2\sin^2\varphi\right)/w_o^2\right] \qquad 5.20$$

where w_o is the radius of the beam waist at z = 0. Most of the total power concentrated within in this circle (in the beam waist) one can write

$$P = \tfrac{1}{2} I_o \pi w^2 \qquad 5.21$$

so that in terms of the power one can rewrite the intensity as

$$I(r) = \frac{2P}{\pi w^2}\exp\left[-2\left((r+R\cos\varphi)^2 + R^2\sin^2\varphi\right)/w^2\right]. \qquad 5.22$$

Noting that for the unit vector normal to the curved part of the cylinder one can write

$$\hat{s} = \hat{x} + \cos\varphi\hat{x} + \sin\varphi\,\hat{z} \tag{5.23}$$

Substituting the infinitesimal area $da = Rd\varphi dy$, Eqs. (5.3) and (5.23) into Eq. (5.19), one finds

$$\vec{F} = -\frac{8P_wR^2}{ct\pi w^2}\left(\frac{m^2-1}{m^2+1}\right)\int_0^{2\pi}\int_{-t/2}^{t/2}\exp\left[-2\left(r^2+R^2+2rR\cos\varphi\right)/w^2\right] \times\left(\hat{x}+\cos\varphi\hat{x}+\sin\varphi\,\hat{z}\right)d\varphi dy \tag{5.24}$$

After the integration of dy we can write the next equation as,

$$\vec{F} = -\frac{8P_wR^2}{c\pi w^2}\left(\frac{m^2-1}{m^2+1}\right)\exp\left[-\frac{2\left(r^2+R^2\right)}{w^2}\right]\int_0^{2\pi}\exp\left[-4rR\cos\varphi/w^2\right] \times\left(\hat{x}+\cos\varphi\hat{x}+\sin\varphi\,\hat{z}\right)d\varphi \tag{5.25}$$

which results in

$$F = -\frac{16n_1P_w\rho^2}{cw_o^2}\frac{m^2-1}{m^2+1}e^{-\frac{2}{w_o^2}\left(\rho^2+r_t^2\right)}J_1\left(0,\frac{4r_t\rho}{w_o^2}\right) \tag{5.26}$$

for $\frac{4r_t\rho}{w_o^2} << 1$, the $J_1\left(0,\frac{4r_t\rho}{w_o^2}\right)\approx 1$, using this approximation the force can be written as,

$$F = -\frac{16n_1P_w\rho^2}{cw_o^2}\frac{m^2-1}{m^2+1}e^{-\frac{2}{w_o^2}\left(\rho^2+r_t^2\right)} \tag{5.27}$$

Where P_w, ρ , n_1, m, c, w_o and r_t are power, the radius of RBC, refractive index of the medium, the ratio of the refractive index of the cell to the medium, minimum spot size and the distance from the trap to the center of RBCs respectively. The trapping force in Eq. (5.27) was used to calculate the numerical data of the trapping force using the measured parameters.

5.2 Results

This study presented two types of RBC, sickle cell trait (SCT) and sickle cell anemia (SCA). Each of the two RBCs consists of 49 samples cells. In this section we will analyze and compare the elasticity property of sickle cell trait (HbAS) and sickle cell anemia (HbSS) in two different methods. The first method was studied by trapping and compressing. The trapping force calculated using Eq. (5.27) and the % difference in free radius and area versus trapped radius and area for 98 individual cells were calculated. In the second method each SCT and SCA samples divided into seven different subgroups. Individual cells in the same subgroup were stretched by moving the piezo-driven sample stage (PS) with same velocity. However, the velocities of different subgroups oscillate in different velocity. The average drug force for each subgroup was 1.48 pN, 1.26 pN, 1.10 pN, 0.853 pN, 0.635 pN, 4.31 pN and 3.23 pN. The average percent difference in stretched radius and area versus trapped radius and area was calculated.

To conduct this analysis, we used the maximum and minimum radius and area of HbAS and HbSS samples when it is free, trapped and stretched. The stiffness, relative change of free radius and relative change of free area from trapped and stretched from trapped cells were calculated. These methods of analysis presented to show the elasticity property of the HbAS and HbSS. The radius and area for the free, trapped and stretched HbAS and HbSS red blood cells was measured by Image Pro plus6 software.

Stiffness 'k' is the change of stretching force over relative change of radius for the individual HbAS and HbSS which expressed as $k = \Delta F/\Delta R$, where $\Delta R = R_{sheer} - R_{trap}$.

The radius of HbAS ranges from 3.84 μm to 5.38 μm with average of 4.67 μm was less than the average of HbSS 5.24 μm which ranges from 4.45 μm to 6.12 μm. The mean value of the trapping force 0.26pN and 0.33pN for the HbAS and HbSS respectively. While the drag force 1.20 pN for HbAS and 1.27 pN for HbSS. HbSS is stretched with higher force but it has lower relative percent difference than HbAS as shown in table 5.1.

49 HbAS Red blood cell sample					
Quantities	Mean	Std. Dev	Min	Median	Max
Radius(µm)	4.67	0.39	3.84	4.75	5.38
HbAS % difference in free radius from trapped radius	8.78	1.91	3.90	8.94	12.84
Trapping Force (pN)	0.26	0.04	0.18	0.27	0.35
Drug force (pN)	1.20	0.56	0.39	1.19	2.23
HbAS % difference in trapped radius from stretched radius	8.23	3.62	1.57	8.10	17.83
Stiffness (µN/m)	0.08	0.01	0.06	0.08	0.09
49 HbSS Red blood cell sample					
Radius (µm)	5.24	0.33	4.45	5.27	6.12
HbSS % difference in free radius from trapped radius	8.07	2.37	3.83	7.81	12.56
Trapping Force (pN)	0.33	0.04	0.24	0.33	0.45
Drug Force (pN)	1.27	0.54	0.43	1.26	2.47
HbSS % difference in trapped radius from stretched radius	6.78	5.39	0.48	5.75	32.44
Stiffness (µN/m)	0.09	0.01	0.07	0.08	0.10

Table 5.1 Statistical parameter for the HbAS and HbSS red blood sample

5.2.1 Free and trapped radius and area for SCT and SCA cells

Radius and area of the cell were measured before trapped. The relative change of can be calculated

$$\%DR = \frac{\left(R_f - R_T\right)}{R_f} \times 100 \qquad 5.28$$

Where (%DR) is percentage difference in radius. The cell shrinks when it was trapped, so the difference will be $\Delta R = R_f - R_T$. The percentage difference for both SCT and SCA was calculated using Eq. (5.44).

$$\%DA = \frac{\left(A_f - A_T\right)}{A_f} \times 100 \qquad 5.29$$

Where (%DA) is percentage difference in area.

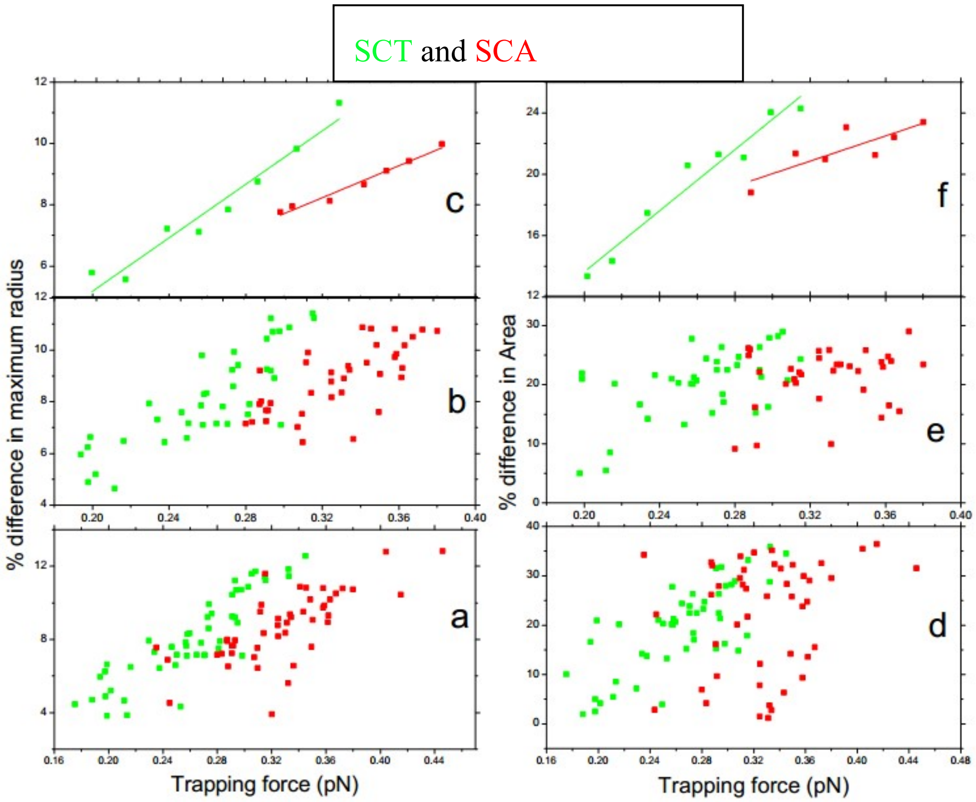

Figure 5.3 (a) –(c) for radius percent difference vs trap and (d)-(f) for area percent difference vs trapping force HbAS (green) and HbSS (red).

In Figure. 5.3 the analysis was done from the trapped radius and area relative to the free radius and area of HbAS (green) and HbSS (red)) respectively. The Figure 5.3 (a) and (d) shows the 49 HbAS (green) and 49 HbSS (red) samples, the radius percent difference versus trapping force of HbAS (green) and HbSS (red). The reduced data shown in the Figure 5.3 (b) and (e) was obtained first sorting by trapping force and deleted two from the minimum and maximum and then sorting by maximum radius or area percentage difference and removed three maximum and two minimum. Finally data displayed in the Figure 5.3 (c) and (f) were reduced using by grouping OriginPro [www.originlab.com]. The result clearly shows that the value and the slope of the HbAS samples are greater than the HbSS.

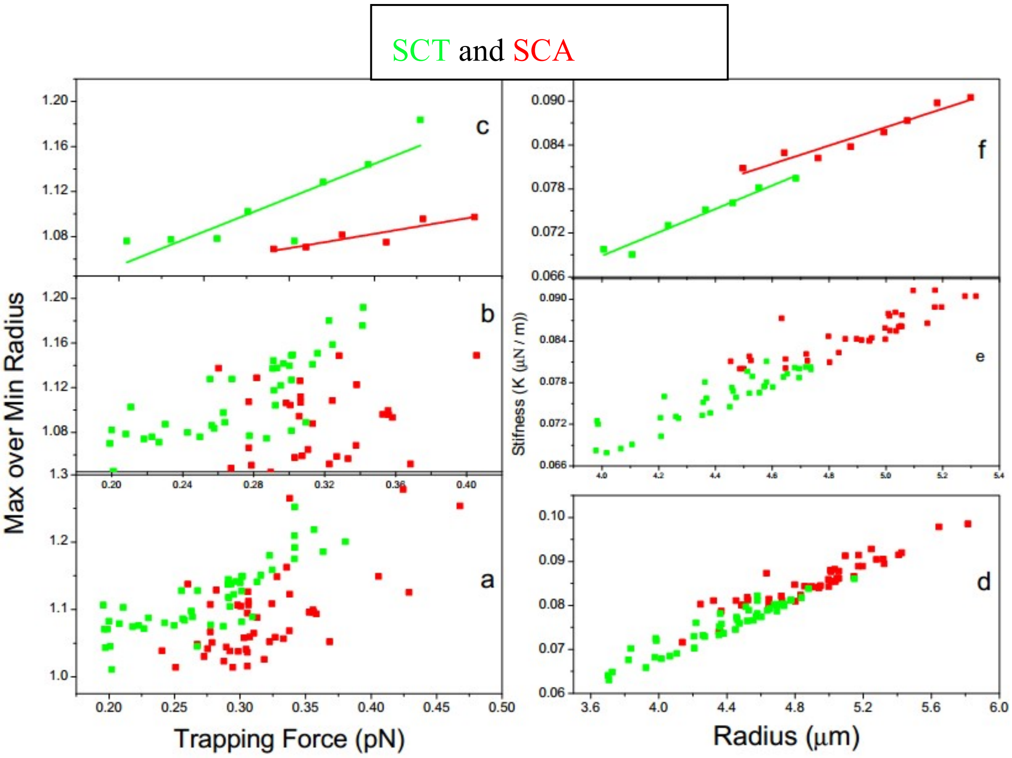

Figure 5.4 The fraction of Max radius over Min radius and stiffness versus radius for the HbAS (blue) and HbSS (red) red blood cells.

The Figure 5.4 (a)-(c) shows the ratio of maximum radius over the minimum radius versus trapping force. Figure.5.4 (a) the whole data of HbSS (red) and HbAS (green) red blood cell samples displayed. A similar procedure with (Figure 5.3) was used to manipulate the data reduction. The result displayed in Figure 5.4 (c) shows HbAS is higher magnitude than HbSS. Figure 5.4 (d)-(f) showing the data distribution for HbSS (red) and HbAS (blue) for stiffness versus force. All the data for stiffness versus stretched radius of HbAS (green) and HbSS (red) are displayed in the Fig.5.4 (d). Figure 5.4 (f) clearly shows the HbSS (red) is stiffer than HbAS (green).

5.2.2 Trapped and stretched Cells

The relative change of stretched radius from the trapped can be calculated as,

$$\%DR = \frac{(R_S - R_T)}{R_S} \times 100 \qquad 5.30$$

Where (%DR) is percentage difference in radius. The cell stretched by the drug force, so the difference will be $\Delta R = R_S - R_T$. The percent difference for both SCT and SCA has been calculated using Eq. (5.27).

$$\%DA = \frac{(A_S - A_T)}{A_S} \times 100 \qquad 5.31$$

Where (%DR) is percentage difference in area.

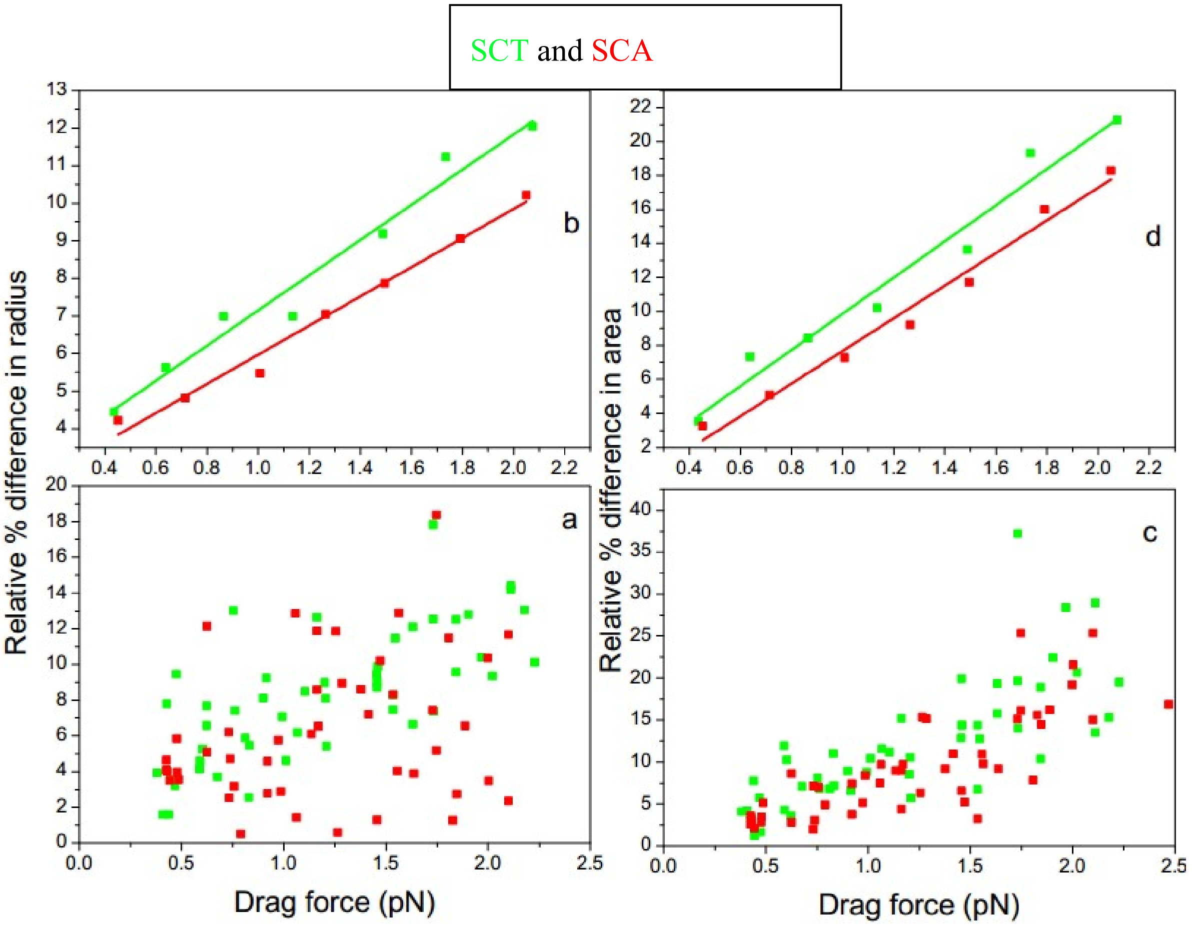

Figure 5.5 Show the relative percent difference vs drug force for HbAS (green) and HbSS (red).

The Figure 5.6 (a) and (c) have 49 HbAS and 49 HbSS sample were displayed. Each HbAS and HbSS divided in seven groups with seven different velocities. Figure 5.6 (b) and (d) show the average from the seven groups' relative percentage difference in radius and area vs drug force for HbAS and HbSS data respectively. The results confirm that the relative change of HbAS has higher value than the HbSS red blood cells.

Using independent two-sample t-statistical analyses is based on the assumption that the variances of the two samples are equal and the other is not. The results for t-test statistics for the radius percentage difference and stiffness are given in Table 5.2. These results show that there was a significant difference between the HbAS and HbSS groups. At 0.05 significant level, the percentage difference in radius (free from trapped) and (trapped from stretched) in the HbAS and HbSS. The two-sample t-test for both equal and not equal variance assumptions the mean values for both (free from trapped) radiuses and (trapped from stretched) radiuses are significantly different. The stiffness of the HbAS and HbSS are also significantly different at 0.01 level. We can conclude that the mean relative percentage difference for HbAS is significantly greater than HbSS and the mean stiffness for HbAS is significantly less than HbSS. Therefore, t-test statistics analyses further confirms HbAS has more elastic property than HbSS.

HbAS vs HbSS			
	Radius % Diff stretched vs Trap		
	t Statistic	DF	Prob>|t|
Equal Variance Assumed	-2.22	96	0.03
Equal Variance NOT Assumed	-2.22	90.68	0.03
HbAS vs HbSS			
Equal Variance Assumed	Radius % Diff Free vs Trap		
	-2.36	98	0.02
Equal Variance NOT Assumed	-2.36	94.26	0.02
HbAS vs HbSS			
Equal Variance Assumed	Stiffness		
	-3.20	96	0.0019
Equal Variance NOT Assumed	-3.20	61.40	0.0022

Table 5.2 Hypothesis testing by two sample t-test.

5.3 Discussion

The elastic property of the HbAS and HbSS RBCs was studied in laser technique in this research. In table 5.1 the value of the trapping force for HbAS was 0.26 pN with %DF in radius of (8.78%) which is less than for HbSS (0.33 pN) with %DF in radius (8.07%), and also the stretching drag force of HbAS (1.2 pN) with %DF (8.23%) is less than HbSS (1.3 pN) with %DF (6.70%). the stiffness of the HbSS has higher value (0.08μN/m) than HbAS (0.07μN/m).

Brandão [125] observed that RBC elasticity from sickle cell trait (AS) units stored for 1 day (median =0·84 × 10-3 dyn/cm), 14 days (0·81 × 10-3 dyn/cm) and 21 days (1·48 × 10-3 dyn/cm). It was significantly greater than that of normal cell (AA) cells stored for 1 day (0·58 × 10-3 dyn/cm),14 days (0·65 × 10-3 dyn/cm) and 21 days (0·66 × 10-3 dyn/cm). Since sickle cell trait RBC contain sickle cell, the normal RBC needs less force per centimeter than that of the trait. In all three different storage time sickle cell AS have larger dyn/cm than AA.

Solomon [86] showed by laser trapping method the relative changes in longitudinal (maximum) and the mean diameters when the cells are trapped or trapped and dragged by different speeds with respect to the corresponding diameters when the cells are free, appear to be higher for SCA than SCT. Byun [126] studied the optical tweezers and micropipette aspiration techniques subject the RBC directly to mechanical deformation and yield shear modulus of sickle RBCs in the range of 8–20 μN m^{-1}. Maciaszek [127] observed that AFM measurements have found that the Young's modulus of SCA RBCs is stiffer than normal RBCs with a widely distributed Young's modulus ranged from 3 kPa to 50 kPa.

All the results cited [86,129-131] are in agreement with our result explained in the first paragraph of the discussion.

Chapter Six

6 Conclusion

In this section we want to summarize, highlights, and make some important remarks about the studies we have presented in this dissertation. The studies presented in two parts focused on the application of LT technique in biomedical application. In the first part, which is actually the major component of the study, we have demonstrated a new alternative way to measure radiation dose in in vitro chemo treated 4T1 breast cancer cells. In the second part, we have shown how a LT technique were used to quantitatively demonstrate the distinct difference in elasticity of human RBCs in SCA and SCT.

In our study on 4T1 breast cancer cells, we have studied the radio-sensitivity of these cells treated by a naturally occurring antitumor compound, 2-Dodecyl-6-methoxycyclohexa-2, 5-diene-1, 4-dione (DMDD) extracted from the root of *Averrhoa carambola* L. The radio-sensitivity was studied by measuring and comparing the TIE and TRD for *in vivo* 2-h and 24-h treated groups with an untreated control group of 4T1 cells. The TIE and TRD were determined using a new approach that uses laser trapping technique for single and multiple cell ionization. The results obtained and confirmed by t-test statistical analyses show that TIE and TRD decreased as the period of treatment increased. This clearly demonstrates the increase in radio-sensitivity of the 4T1 cells due to the antitumor compound DMDD. The most interesting and significant part of the results is the TRD and its relation to the mass observed, in particular, in multiple cell ionization. These results demonstrate the significance of the effect of induced charges and hyperthermia resulting from radiation mediated electrical and thermal interactions within the cells. The results, regardless of the treatment, showed TRD decreased as the mass of the cell increased. This decrease in TRD becomes more significant in multiple cell ionization as we observed in TRD vs the number of cells entering the trap. In addition to the effect stemming from the antitumor compound used to treat the cells, the significant reduction in the TRD in multiple cell ionization is associated with the chain effect of ionization by the radiation field and the absorption by water molecules at 1064 nm.

The charge developed inside the trap which forced out the cells have been calculated. The charge developed in the time the cell in the trap for 2-h and 24-h treated were studied by comparing the charge developed in the control group. The charge developed per unit mass also studied in all the three groups using the normal distribution, pie chart and descriptive statistics. The charge and charge per unit mass increase as the period of DMDD treatment increase. The mean values of the charge for the untreated and 2-h treated and 2-h treated and 24-h treated groups were not significantly different. The charges in all the groups increase as the size of the cell increase. The acceleration also increases when the charge increases. The cell loses its charge as the displacement increases away from the trap. The charge over mass decreases as the radius of the cell increase The result obtained in the NonlinearModelFit have similar behavior as with the first model for the charge with radius relation and in both models the motion of the ejected cells are over damped. The two models developed have significant difference in the magnitude of the charge since we use unchanged electric permittivity in the first model.

It is important to point out that; generally, the results reported in this study highlighted the effect of combined modalities in radiotherapy, chemo, and hyperthermia useful only in vitro cancer treatment. However, with the recent advances made in the development of biocompatible nanoparticles for combined modalities in cancer treatment, the method used and the results reported in this study could be applied for *in vivo* cancer treatment. Based on the results reported here, it is possible to develop a theoretical/computational model that predicts the TRD for *in vivo* treatment by extrapolating the TRD determined using multiple cell ionization if we have accurate information about the size and density of the tumor. However, this requires more advanced studies that integrate prior, during, and post ionization dynamics in both single and multiple cell ionization as well as the dose and period of the treatment by the antitumor compound, DMDD. One important prospective study is an accurate measurement of the charge and the temperature elevation that occurs when the cell(s) interact with radiation after a treatment.

By developing a theoretical model for the trapping force we have also studied the elasticity of RBCs in SCT (with hemoglobin type HbAS) and in SCA (with hemoglobin type HbSS). We studied by comparison of the elasticity property using radius and area relative percent difference and stiffness versus trapping force. The validity of these results were also studied using descriptive statistics. The sizes of the RBCs in SCA were found to be larger than those in SCT. The results for the quantities describing the elasticity of the cells had consistently showed that the RBCs in the SCT display lower rigidity and higher deformability than the RBCs with SCA. This behavior, in particular, is distinctly shown by the stiffness constant versus size (measured by the radius) results. This property in elasticity is also shown in the results for the relative change of the percent difference of individual RBCs in SCT (HbAS) and SCA (HbSS). The results for the ratio of Maximum to minimum radius also show the same behavior in the elasticity of the RBCs in the two blood samples.

7 Future Prospects and Recommendations

In this study ionization energy and radiation dose measured for single and mass cells showed clear difference between untreated, 2-h treated and 24-h treated. This study reveals significant difference of TIE and TRD between control and treated groups. The recent advances made in the development of biocompatible nanoparticles for combined modalities in cancer treatment, the method used and the results reported in this study could be applied for *in vivo* cancer treatment. Based on the results reported here, it is possible to develop a theoretical/computational model that predicts the TRD for *in vivo* treatment by extrapolating the TRD determined using multiple cell ionization if we have accurate information about the size and density of the tumor. However, this requires more advanced studies that integrate prior, during, and post ionization dynamics in both single and multiple cell ionization as well as the dose and period of the treatment by the antitumor compound, DMDD. One important prospective study is an accurate measurement of the charge and the temperature elevation that occurs when the cell(s) interact with radiation after a treatment. We propose to develop the research line as above.

List of publication

1. E. Muhammed, L. Chen, Y. Gao, and D. Erenso, "Radio-sensitivity of 4T1 chemo-treated breast cancer cells measured by laser trapping," in *Frontiers in Optics + Laser Science APS/DLS*, OSA Technical Digest (Optical Society of America, 2019), paper JTu3A.96.
2. Endris Muhammed, Li Chen, Ying Gao, Daniel Erenso, Chemo treated 4T1 breast cancer cells radiation response measured by single and multiple cells ionization using infrared laser trap. Scientific Reports (nature) , *(2019) 9:17547* ,https://doi.org/10.1038/s41598-019-53821-y

Bibliography

1. Pulaski, BA; Ostrand-Rosenberg, S (May 2001). "Mouse 4T1 breast tumor odel". *Current Protocols in Immunology*. **20** (1): Unit 0.2. doi:10.1002/0471142735.im2002s39. PMID 18432775
2. Ashkin, Arthur, Applications of laser radiation pressure. 1980, Science, Vol. 210, pp. 1081-1088. 10.1126/science.210.4474.1081.
3. Ashkin, Arthur, J. M. Dziedzic, and T. Yamane. Optical trapping and manipulation of single cells using infrared laser beams. 1987, Nature, Vol. 330, pp. 769-771.
4. Ashkin.The Nobel Prize in Physics 2018 was awarded "for groundbreaking inventions in the field of laser physics" with one half to Arthur Ashkin "for the optical tweezers and their application to biologicalsystems", the other half jointly to Gérard Mourou and Don. 2018, Current Science, Vol. 115, p. 1844.
5. Brandao, M. M., A. Fontes, M. L. Barjas-Castro, L. C. Barbosa, F. F. Costa, C. L. Cesar, and S. T. O. Saad. Optical tweezers for measuring red blood cell elasticity: application to the study of drug response in sickle cell disease. 2003, European journal of haematology, Vol. 70, pp. 207-211.
6. T. L. Gustavson, A. P. Chikkatur, A. E. Leanhardt, A. Gorlitz, S. Gupta, S. Gupta, D. E. Pritchard, and W. Ketterle. Sodium Bose-Einstein condensates in the F= 2 state in a large-volume optical trap. 2002, Phys. Rev. Lett, Vol. 88.
7. Brandão, M. M., S. T. O. Saad, C. L. Cezar, A. Fontes, F. F. Costa, and M. L. Barjas-Castro. Elastic properties of stored red blood cells from sickle trait donor units. 3, 2003, Vox sanguinis, Vol. 85, pp. 213-215.
8. Bordeleau, François, Judicael Bessard, Normand Marceau, and Yunlong Sheng. Measuring integrated cellular mechanical stress response at focal adhesions by optical tweezers. 9, 2011, Journal of biomedical optics, Vol. 16, pp. 095005-095005.
9. S Rancourt-Grenier, M Wei, J Bai, A Chiou, P Bareil, P Duval and Y Sheng. Dynamic deformation of red blood cell in Dual-trap Optical Tweezers. 2010, Opt. Exp. , pp. 10462-10472.
10. Pellizzaro, Aline, Gabriel Welker, David Scott, Rance Solomon, James Cooper, Anthony Farone, Mary Farone, Robert S. Mushi, Maria del Pilar Aguinaga, and Daniel Erenso. Direct laser trapping for measuring the behavior of transfused erythrocytes in a a sickle cell anemia patient. 9, 2012, Biomedical Optics Express, Vol. 3, pp. 2190-2199.
11. R. Solomon, A. Pellizzaro, D. Devito, C. A. Brown, J. Cooper, H. Crogman, J. Revalee, A. Farone, M. Farone, Y. Gao, and D. B. Erenso. Cancerous Lung Cells Treatment by Herbal Medicines Measured by the Response to Compressional Force Induced by a a Laser Trap. 2014, Biomedical Optics.
12. Chu, Steven. Laser manipulation of atoms and particles. 1991, Science, pp. 861–866.
13. Quake, J. Meiners and S. R. Femtonewton Force Spectroscopy of Single Extended DNA Molecules. 2000, Phys Rev. Lett, Vol. 84.

14. U. Bockelmann, P. Thomen, B. Essevaz-Roulet, V. Viasnoff, and F. Heslot. Unzipping DNA with Optical tweezers: high sequence sensitivity and force flips. 2002, Biophys. J, Vol. 82.
15. C. Bustamante Z. Bryant, and S. B. Smith,, 421, 423. Ten years of tension: single-molecule DNA mechanicsNature. 2003, Nature, Vol. 421, pp. 423-427.
16. Herrick, James B. Peculiar elongated and sickle-shaped red blood corpuscles in a case of severe anemia. s.l. : 6, 1910, Archives of Internal Medicine, Vol. 5, p. 517.
17. L H Pauling, A Itano, S J Singer, and I C Wells. Sickle cell anemia, a molecular disease. 1949, Science, Vol. 110, pp. 543-548 .
18. Ingram, V. M. Gene mutations in human hemoglobin: the chemical difference between normal and sickle cell hemoglobin. 1957, Nature, Vol. 180, pp. 326-328.
19. Madigan, Catherine, and Punam Malik. Pathophysiology and therapy for haemoglobinopathies; Part I: sickle cell disease. 2006, Expert reviews in molecular medicine, Vol. 8, pp. 1-23.
20. Adams, Robert J., Kwaku Ohene-Frempong, and Winfred Wang. Sickle cell and the brain. 2001, pp. 31-46.
21. Steen, R. Grant, Mark A. Miles, Kathleen J. Helton, Susan Strawn, Winfred Wang, Xiaoping Xiong, and Raymond K. Mulhern.Cognitive impairment in children with hemoglobin SS sickle cell disease: relationship to MR imaging findings and hematocrit. 3, 2003, American Journal of Neuroradiology, Vol. 24, pp. 382-389.
22. Reid, Clarice D., Samuel Charace, and Bertram Lubin. Management and therapy of sickle cell disease. s.l. : Diane Books Publishing Company, 1995.
23. Sankaran, Vijay G. Targeted therapeutic strategies for fetal hemoglobin induction 2011, ASH Education Program Book, pp.459--465
24. M. Kelley, Y. Gao, and D. Erenso. Single cell ionization by a laser trap: a preliminary study in measuring radiation dose and charge in BT20 breast carcinoma cells. 9, 2016, Biomed. Opt. Express, Vol. 7, pp. 3438-3448.
25. M. Kelley, J. Cooper, D. Devito, R. Mushi, M. D. P. Aguinaga, and D. Erenso.Laser trap ionization for identification of human erythrocytes with variable hemoglobin quantitation, J. of Biomedical Optics. 2018, Journal of Biomedical Optics , Vol. 23, p. 055005.
26. M. Pasquerilla M. Kelley, R. Mushi, M. D. P. Aguinaga, and D. Erenso. Laser trapping ionization of single human red blood cell. 2018, Biomedical Physics & Engineering Express’, Vol. 4, pp. 045020. l

27. World Health Organization. Global Health Observatory. Geneva: World Health Organization; 2018. who.int/gho/database/en/. Accessed June 21, 2018.
28. Bray, F., et al. Global cancer statistics 2018: GLOBOCAN estimates of incidence and mortality worldwide for 36 cancers in 185 countries. 2018, CA: A Cancer Journal for Clinicians, 68, 394-424
29. Baskar R., Lee, K. A., Yeo, R. & Yeoh, K. W. 2012, Cancer and radiation therapy: current advances and future directions. Int J Med Sci. 9(3), 193–199

30. Liauw, S. L., Connell, P. P. & Weichselbaum, R. R. 2013, New paradigms and future challenges in radiation oncology: an update of biological targets and technology. Sci Transl Med. 5(173):173sr2.
31. Lane, Rodney J and Khin, Nyan Y and Pavlakis, Nick and Hugh, Thomas J and Clarke, Stephen J and Magnussen, John and Rogan, Chris and Flekser, Roger L. 2018, Challenges in chemotherapy delivery: comparison of standard chemotherapy delivery to locoregional vascular mass fluid transfer. Future Oncology Vol. 14(7), pp.647-663.
32. Wang, Li and Correa, Candace R and Zhao, Lujun and Hayman, James and Kalemkerian, Gregory P and Lyons, Susan and Cease, Kemp and Brenner, Dean and Kong, Feng-Ming. 2009, The effect of radiation dose and chemotherapy on overall survival in 237 patients with stage III non-small cell lung cancer. Int J Radiat Oncol Biol Phys Vol. 73(5), pp.1383-1390.
33. Begg, A. C., Stewart, F. A., & Vens, C. 2011, Strategies to improve radiotherapy with targeted drugs. Nat Rev Cancer. Vol. 11(4), pp. 239–53.
34. Maingon, Philippe and Govaerts, Anne-Sophie and Rivera, Sofia and Vens, Conchita and Shash, Emad and Gregoire, Vincent. 2014, New challenge of developing combined radio-drug therapy. Chinese Clinical Oncology, Vol. 3(2).
35. Yoo, Gyu Sang and Park, Won and Yu, Jeong Il and Choi, Doo Ho and Kim, Yeon-Joo and Shin, Kyung Hwan and Wee, Chan Woo and Kim, Kyubo and Park, Kyung Ran and Kim, Yong Bae and others. 2019, Comparison of Breast Conserving Surgery Followed by Radiation Therapy with Mastectomy Alone for Pathologic N1 Breast Cancer Patients in the Era of Anthracycline Plus Taxane-Based Chemotherapy: A Multicenter Retrospective Study (KROG 1418). Cancer Res Treat. Vol. 51(3), pp. 1041–1051.
36. Nguyen, P. T., Abbosh , A. & Crozier, S. Three-Dimensional Microwave Hyperthermia for Breast Cancer Treatment in a Realistic Environment Using Particle Swarm Optimization. IEEE Transactions on Biomedical Engineering, vol. 64, pp.1335-1344 (2017).
37. Ami, N., Sato, H., & Hayakawa, Y. 2018, Paclitaxel-induced hypothermia and hypoperfusion increase breast cancer metastasis and angiogenesis in mice. Oncology Letters, Vol.15, pp.2330-2334.
38. Norouzi, H., Khoshgard, K. & Akbarzadeh, F. 2018, In vitro outlook of gold nanoparticles in photo-thermal therapy: a literature review. Lasers Med Sci. Vol.33, pp.917.
39. Rastinehad, Ardeshir R and Anastos, Harry and Wajswol, Ethan and Winoker, Jared S and Sfakianos, John P and Doppalapudi, Sai K and Carrick, Michael R and Knauer, Cynthia J and Taouli, Bachir and Lewis, Sara C and others. 2019, Gold nanoshell-localized photothermal ablation of prostate tumors in a clinical pilot device study. Proc. Natl. Acad. Sci. Vol.116 (37), pp.18590-18596.
40. Zhang, H. & Chen, J. 2018, Current status and future directions of cancer immunotherapy. J Cancer Vol.9(10), pp.1773-1781.
41. Zhang P, Cui Z, Liu Y, Wang D, Liu N and Yoshikawa M. Quality evaluation of traditional Chinese drug toad venom from different origins through a simultaneous determination of

bufogenins and indole alkaloids by HPLC. Chemical and pharmaceutical bulletin, Vol. 53, pp. 1582--1586.

42. Dai LP, Wang ZM, Gao HM, Jiang X and Ding GZ. Determination of bufothionine in skin of Bufo bufo gargarizans and HCS injection. 2007 , Zhongguo Zhongyao Zazhi, Vol. 32, pp. 224-226.
43. Qin TJ, Zhao XH and Yun J. Efficacy and safety of gemcitabine- oxaliplatin combined with HCS in patients with advanced gallbladder carcinoma. 2008, World journal of gastroenterology: WJG, Vol. 14, pp. 5210-5216.
44. Ye M, Qu G, Guo H and Guo D.Specific 12 beta-hydroxylation of cinobufagin by filamentous fungi. 2004, Appl. Environ. Microbiol., Vol. 70, pp. 3521-3527.
45. Ma XC, Xin XL, Liu KX, Han J and Guo DA.Microbial transformation of cinobufagin bySyncephalastrum racemosum. 2008, Journal of natural products, Vol. 71, pp. 1268-1270.
46. Ye M, Guo H, Guo H, Han J and Guo D. Simultaneous determination of cytotoxic bufadienolides in the Chinese medicine ChanSu by high-performance liquid chromatography coupled with photodiode array and mass spectrometry detections. 2006, J Chromatogr B Analyt Technol Biomed Life Sci , pp. 86-95.
47. Meng Z, Yang P, Shen Y, Bei W, Zhang Y, Ge Y, Newman RA, Cohen L, Liu L, Thornton B, Chang DZ, Liao Z and Kurzrock R. Pilot study of HCS in patients with hepatocellular carcinoma, no-small cell lung cancer, or pancreatic cancer. 2009, Anticancer research, Vol. 31, pp. 2141-2148.
48. Yan, Sun, and Yang Tianen.A study of the radiosensitive effects on mammary carcinoma in mice by Chinese medicine (Salvia plus Astragalus) and aspirin. 1989, Chinese Journal of Cancer Research, pp. 54-59.
49. Reeve VE, Allanson M, Arun SJ, Domanski D and Painter N.Mice drinking goji berry juice (Lycium barbarum) are protected from UV radiation-induced skin damage via antioxidant pathways. 2010, Photochem Photobiol Sci, Vol. 9, pp. 601-607.
50. Yaron Fuchs and Hermann Steller. Programmed Cell Death in Animal Development and Disease. 2011, Cell, Vol. 147, pp. 742-758.
51. Vichithra R. B. Liyanage, Jessica S. Jarmasz, Nanditha Murugeshan, Marc R. Del Bigio, Mojgan Rastegar, and James R. Davie. DNA Modifications: Function and Applications in Normal and Disease States. 4, 2014, Biology (Basel), Vol. 3, pp. 670–723.
52. Jane E. Visvader and Geoffrey J. Lindeman.Cancer Stem Cells: Current Status and Evolving Complexities. 6, 2012, Cell stem cell, Vol. 10, pp. 717-728.
53. Sophia Ran, Lisa Volk, Kelly Hall, and Michael J. Flister.Lymphangiogenesis and Lymphatic Metastasis in Breast Cancer. 4, s.l. : American Cancer Society, 2009, Pathophysiology, Vol. 17, pp. 229–251.
54. Mohamed, Munazzah Rahman and Sulma.Breast cancer metastasis and the lymphatic system. 2015, Oncology Letters, pp. 1233-1239.
55. Sampaio, Kai Simons and Julio L. Membrane Organization and Lipid Rafts. 2011, Cold Spring Harbor perspectives in biology, Vol. 3, pp. a004697.

56. Richards, G. Pocock and C. The human body: An introduction for biomedical and health sciences. s.l. : Oxford University Press, 2009.
57. Henriette S. Frislev, Theresa Louise Boye, Jesper Nylandsted and Daniel Otzen. Liprotides kill cancer cells by disrupting the plasma membrane. 1, 2017, Scientific report, Vol. 7, pp. 2045-2322.
58. Nicolson, S. J. Singer and Garth L. The Fluid Mosaic Model of the Structure of Cell Membranes. California : American Association for the Advancement of Science, 1972, Science, Vol. 175, pp. 720-731.
59. Marc Eeman and Magali Deleu. From biological membranes to biomimetic model membranes. 2010 , Biotechnol. Agron. Soc. Environ, pp. 719-736.
60. Gerrit van Meer, Dennis R. Voelker, and Gerald W. Feigenson. Membrane lipids: where they are and how they behave. 2, 2008, Nature reviews Molecular cell biology, Vol. 9, pp. 112–124.
61. Griffith JK, Baker ME, Rouch DA, Page MG, Skurray RA, Paulsen.Membrane transport proteins: implications of sequence comparisons. 4, 1992, Current opinion in cell biology, Vol. 4, pp. 684-695.
62. Pardee, Arthur B. Biochemical Studies on Active Transport. 1, 1968, The Journal of general physiology, Vol. 52, pp. 279–295.
63. Xie, Hao. Activity assay of membrane transport proteins. 4, 2008, Acta biochimica et biophysica Sinica, Vol. 40, pp. 269-277.
64. Lodish H, Berk A, Zipursky SL. Transport across Cell Membranes. [book auth.] V. Unger. Molecular Cell Biology. New York : W. H. Freeman and Company, 2000.
65. 58. Alberts et. a.l, and Loadish. Molecular biology of the cell. New York : Garland Science, 2008.
66. Monsees, R. Funk and T. Effects of electromagnetic fields on cells: Physiological and therapeutical approaches and molecular mechanisms of interaction: . s.l. : A review." Cells Tissues Organs, 2006. vol.182, pp. 59–786.
67. Hill, B. Ionic chanals of excitable membranes. USA : Sinauer Associates Inc., 1992.
68. Andersen, W. Green and O. Surface charges and ion channel function. s.l. : Annual Review of Physiology, 1991. vol. 53, pp. 341–359.
69. Richards, G. Pocock and C. The human body: An introduction for biomedical and health sciences. s.l. : Oxford University Press, 2009.
70. Fritz, P. Uhlén and N. Biochemistry of calcium oscillation. s.l. : Biochemical and Biophysical Research Communications, 2010, Biochemical and biophysical research communications, Vol. 396, pp. 28–32.
71. Mohammed Ali Ansari, Ezedin Mohajerani. Mechanism of laser tissue interaction: opticale properties of tissue. 3, laser research institute : s.n., 2011, Journal of Lasers in Medical Sciences, Vol. 2, pp. 119-25.
72. RW, and Waynant. Lasers in Mediciene. s.l. : CRC press, 2001.

73. Tereza Tribulová, František Kačík, Dmitry Evtuguin And Iveta Čabalová. Assessment Of Chromophores In Chemically Treated And Aged Wood By Uv-Vis Diffuse Reflectance Spectroscopy. 2016, Cellulose Chemistry And Technology, Vol. 50, pp. 250-266.
74. Tomohiko Obayashi, Kohei Funasaka, Eizaburo Ohno, Ryoji Miyahara, Yoshiki Hirooka, Michinari Hamaguchi, Hidemi Goto And Takeshi Senga.Treatment with near-infrared radiation promotes apoptosis in pancreatic cancer cells. 3, s.l. : ONCOLOGY LETTERS , 2015, Oncology Letters, Vol. 10, pp. 1836-1840.
75. Zimmermann, U. Electric field-mediated fusion and related electrical phenomena. 3, s.l. : Acta, 1982, Biochimica et Biophysica Acta (BBA)-Reviews on Biomembranes, Vol. 694, pp. 227--277. Acta 694.
76. E. Tekle, R.D. Astumian, P.B. Chock. Electro-permeabilization of cell membranes: effect of the resting membrane potential. 1, 1990, Biochemical and biophysical research communications, Vol. 172, pp. 282– 287.
77. J. Teissie´, M.P. Rols. An experimental evaluation of the critical potential difference inducing cell membrane electropermeabilization. 1, 1993, Biophysical journal, Vol. 65, pp. 409-413.
78. J.C. Weaver, Y.A. Chizmadzhev Theory of electroporation.. 2, 1996, Bioelectrochemistry and bioenergetics, Vol. 41, pp. 135-160.
79. E. Neumann, S. Kakorin, K. Toensig. Fundamentals of eelivery of drugs and genes, Bioelectroc Fundamentals of electroporative delivery of drugs and genes. 1, s.l. : Bioenerg, 1999, Bioelectrochem Bioenerg., Vol. 48, pp. 3-16.
80. Zimmermann, U. Electric field-mediated fusion and related electrical phenomena. 3, 1982, Biochimica et Biophysica Acta (BBA)-Reviews on Biomembranes, Vol. 694, pp. 227-277.
81. R. Benz, F. Beckers, and U. Zimmermann. Reversible electrical breakdown of lipid bilayer membranes: A charge-pulse relaxation study. 1979, J. Membrane Biol, Vol. 48, pp. 181–204.
82. Zimmermann, Hans G. L. and Ulrich. The mechanism of electrical breakdown in the cell membrane of Vilonia atricularis. s.l. : Springer-Verlag New York Inc, 1975, J. Membrane Biol, Vol. 22, pp. 73-90.
83. Lukens, J. Abnormal hemoglobins, general principles. 2004, Expert Reviews in Molecular Medicine, pp. 1247-1262.
84. Jules Dupire, Marius Socol, and Annie Viallat. Full dynamics of a red blood cell in shear flow. 2012, PNAS, Vol. 109, pp. 20808–20813.
85. YongKeun Park, Catherine A. Best, Thorsten Auth, Nir S. Gov, Samuel A. Safran,GabrielPopescu, Subra Suresh, and Michael S. Felda Metabolic remodeling of the human red bloodcell membrane.. 2010, PNAS, Vol. 4, pp. 1289–1294.
86. Piety NZ, Yang X, Kanter J, Vignes SM, George A, Shevkoplyas. Validation of a Low-Cost Paper-Based Screening Test for Sickle Cell Anemia. 1, 2016, PLoS ONE, Vol. 11.
87. Rance Solomon, James Cooper, Gabriel Welker, Elaur Aguilar, Brooke Flanagan, Chelsey Pennycuff , David Scott, Anthony Farone, Mary Farone, Daniel Erenso, Robert Mushi, and

Maria del Pilar Aguinaga. Relative Deformability of Red Blood Cells in Sickle Cell Trait and Sickle Cell Anemia by Trapping and Dragging. 2013. European Conference on Biomedical Optics. p. 880307.

88. Giuseppe Pesce, Giorgio Volpe, Onofrio M. Marag, Philip H. Jones,4 Sylvain Gigan, Antonio Sasso and Giovanni Volpe A Step-by-step Guide to the Realisation of Advanced Optical Tweezers.. 5, s.l. : arXiv, 2015, physics.optic, Vol. 32, pp. B84-B98.
89. A. Ashkin, J.M. Dziedzic, J.E. Bjorkholm, and S. Chu. Observation of a single-beam gradient force optical trap for dielectric particles. Optics Letters, 11(5):288, 1986. Observation of a single-beam gradient force optical trap for dielectric particles. 5, 1986, Optics Letters, Vol. 11, pp. 288-290.
90. Block, Steven M. Nanometres and piconewtons: the macromolecular mechanics of kinesin. 4, 1995, Trends in cell Biology, Vol. 5, pp. 169--175.
91. C. Bustamante, Z. Bryant, and S. B. Smith.Ten years of tension: Single-molecule DNA mechanics. 2003, Nature, Vol. 421, pp. 423-7.
92. Stelzer, A. Rohrbach and E. H. K. Trapping forces, force constants, and potential depths for dielectric spheres in the presence of spherical aberrations. 2002, Applied Optics, Vol. 41, pp. 2494–2507.
93. Ashkin. Forces of a single-beam gradient laser trap on a dielectric sphere in the ray optics regime2, 1992, Biophysical journa, Vol. l 61, pp. 569-582.
94. Ashkin, A. Optical trapping and manipulation of neutral particles using lasers. s.l. : National Academy of Sciences, 1997. Proceedings of the National Academy of Sciences. Vol. 94, pp. 4853-4860.
95. Chunxia Chen, Zhihuan Nong, Qiuqiao Xie, Junhui He, Wene Cai, Xiuneng Tang, Xiaoyu Chen, Renbin Huang and Ying Gao. 2-Dodecyl-6-methoxycyclohexa-2, 5-diene-1, 4-dione inhibits the growth and metastasis of breast carcinoma in mice. 2017, Scientific RepoRts, Vol. 7, pp. 6704
96. Fei Yan, Wanlu Duan, Yekuo Li, Hao Wu, Yuli Zhou, Min Pan, Hongmei Liu, Xin Liu and Hairong Zheng. NIR-Laser-Controlled Drug Release from DOX IR-780-Loaded Temperature-Sensitive-Liposomes for Chemo Photothermal Synergistic Tumor therapy. 13, 2016, Theranostics, Vol. 6, pp. 2337-2351.
97. Lúcio Frigo, Juliana SS Luppi, Giovani M Favero, Durnavei A Maria, Sócrates C Penna, Jan M Bjordal, Rene J Bensadoun and Rodrigo AB Lopes-Martins.The effect of low-level laser irradiation (In-Ga-Al-AsP - 660 nm) on melanoma in vitro and in vivo. 1, s.l. : BMC Cancer, 2009, BMC cancer, Vol. 9, p. 404.
98. Yohei Tanaka, Kiyoshi Matsuo, Shunsuke Yuzuriha, Huimin Yan and Jun Nakayama. Non-thermal cytocidal effect of infrared irradiationon cultured cancer cells using specialized device. 6, 2010, Cancer Sci, Vol. 101, pp. 1396–1402.
99. Anmar A. Hussein, Haitham L. Saadon, Asaad A. Khalaf1, Muzahim M. Abdulah. Optical laser trapping for studying the deformability of sickle red blood cells in response to hydroxyurea2, 2018, Iraqi Journal of Hematology , Vol. 7. 10.4103/ijh.ijh_6_18.

100. R. Solomon, J. Cooper, E. Aguilar, G. Welker, C. Pennycuf, D. Scott and B. Flanagan, Daniel Erenso. Physical and Mechanical Properties of the Human Red Blood Cells with Different Hemoglobin Types.. s.l. : University of Wisconsin, La Crosse, WI , 2013. 2013 NCUR.
101. M. Dao, C.T. Lim, S. Suresh Mechanics of the human red blood cell deformed by optical tweezers.. 2003, Journal of the Mechanics and Physics of Solids, Vol. 51, pp. 2259–2280.
102. Thomas J. Smart, Christopher J. Richards, Rupesh Agrawal and Philip H.Jones. Stretching Red Blood Cells with Optical Tweezers. 2017, Optics in the Life Sciences, pp. OtM4E--6.
103. Sungrae Lee, Boram Joo, Pyo Jin Jeon, Seongil Im, and Kyunghwan Oh.Columnar deformation of human red blood cell by highly localized fiber optic Bessel beam stretcher. 2015, Biomedical optics express, Vol. 6, pp. 4417--4432. DOI:10.1364/BOE.6.004417.
104. Millennia IR Diode-pumped, cw Infrared Laser, User's Manual. s.l. : Spectra-Physics, 1997.
105. A J Singh, S K Sharma, P K Mukhopadhyay and S M Oak. Dual wavelength operation in diode-end-pumped hybrid vanadate laser. 5, 2010, Pramana Journal of physics, Vol. 75, pp. 929-934.
106. Shaevitz, Joshua W.. A Practical Guide to Optical Trapping. 2006, University of Washington, Vol. 138.
107. T. Kotnik, P. Kramar, G. Pucihar, D. Miklavcic and M. Tarek. Cell Membrane Electroporation Part 1: The Phenomenon. 5, Ljubljana : s.n., 2012, IEEE Electrical Insulation Magazine, Vol. 28, pp. 14-23. 10.1109/MEI.2012.6268438.
108. Pohl, H.A. Dielectrophoretic force: A comparison of theory and experiment. s.l. : Cambridge Univ. Press, London, 1978, J. BioL Phys, Vol. 6, pp. 133-160.
109. Dimitrov, D.S. Electroporation and Electrofusion of Membranes. Sofia : Elsevier Science B.V, 1995, Handbook of biological physics, Vol. 1, pp. 851-901.
110. William H. Grover, Andrea K. Bryan, Monica Diez-Silva, Subra Suresh, John M. Higgins, and Scot R Manalis. Measuring single cell density. 2011, Proceedings of the National Academy of Sciences, Vol. 108, pp. 10992-6.
111. Yuliang Zhao, Hok Sum Sam Lai, Guanglie Zhang, Gwo-Bin Lee, and Wen Jung Li. Measurement of single leukemia cell's density and mass. 2015, Biomicrofluidics, Vol. 9, p. 022406.
112. Michal Baniyash, Tamar Netanel, and Isaac P. Witz. Differences in Cell Density Associatedwith Differences in Lung-colonizing Ability of B16 Melanoma Cells. 1981, American Association for Cancer Research, Vol. 41, pp. 433-437.
113. A. Pellizzaro, G. Welker, D. Scott, R. Solomon, J. Cooper, A. Farone, M. Farone, R. Mushi, M. del Pilar Aguinaga, and D. Erenso. Direct laser trapping for measuring the behavior of transfused erythrocytes in a sickle cell anemia patient. 9, 2012, Biomedical Optics Express, Vol. 3, pp. 2190-2199. 0.1364/BOE.3.002190.

114. Norouzi, H., Khoshgard, K. & Akbarzadeh, F. In vitro outlook of gold nanoparticles in photo-thermal therapy: a literature review. . 2018, Lasers Med Sci , Vol. 33. 10.1007/s10103-018-2467-z.
115. Guan-Bo Liao, Paul B. Bareil, Yunlong Sheng, and Arthur Chiou. One-dimensional jumping optical tweezers for optical stretching of bi-concave human red blood cells. 2008, Optics Express, Vol. 16, pp. 1996-2004.
116. Jonas, Pavel Zema´nek and Alexandr. Simplified description of optical forces acting on a nanoparticle in the Gaussian standing wave. 2002, JOSA A, Vol. 19, pp. 1025-1034.
117. John Bechhoefer and scott wilson. Faster, cheaper, safer optical tweezers for the undergraduate laboratory. Canada : American Association of Physics, 2002, American Journal of Physics, Vol. 70, pp. 393-400.
118. Golombeck, M-A and Riedel, CH and Dossel, O. Calculation of the dielectric properties of biological tissue using simple models of cell patches.2002, Biomedizinische Technik/Biomedical Engineering, vol. 47, pp. 253—256
119. Peyman, A and Gabriel, C and Grant, EH. Complex permittivity of sodium chloride solutions at microwave frequencies. 2007, Bioelectromagnetics, vol.28(4), pp.264--274
120. Hao, Tian. Electrorheological fluids: the non-aqueous suspensions. 2011. Academic Press. Elsevier vol. 22.
121. Stogryn, A, Equations for calculating the dielectric constant of saline water (correspondence). 1971, IEEE transactions on microwave theory and Techniques. vol. 19(8) pp. 733—736
122. Zimmermann, U Electric field-mediated fusion and related electrical phenomena.. 1982, Biochim Biophys, pp. 227-277.
123. Rand, R. P. interacting phospholipid Bilayers: measured force and induced structural changes. 1981, Annual review of biophysics and bioengineering, Vol. 10, pp. 277-314.
124. Dimitrov, D.S., D.V. Zhelev and R.K. Jain. Stability of viscoelastic membrane systems modeled as multilayered thin films. 1985, J. Theoret. Biol, Vol. 113, pp. 353–377.
125. Vanegas Acosta, J.C. Electric fields and biological cells : numerical insight into possible interaction mechanisms. s.l. : Technische Universiteit Eindhoven, 2015.
126. M. M. Brandão, S. T. O. Saad, C. L. Cezar, A. Fontes, F. F. Costa & M. L. Barjas-Castro. Elastic properties of stored red blood cells from sickle trait donor units. 2003, Vox Sanguinis , Vol. 85, pp. 213–215.
127. Byun, H., Hillman, T.R., Higgins, J.M., Diez-Silva, M., Peng, Z., Dao, M., Dasari, R.R., Suresh, S., Park, Y. 2012, Optical measurement of biomechanical properties of individual erythrocytes from a sickle cell patient. Acta Biomater, Vol. 8, pp. 4130–4138.
128. Maciaszek, J.L., Lykotrafitis, G.,. Sickle cell trait human erythrocytes are significantly stiffer than normal. 2011, Journal of biomechanics, Vol. 44, pp. 657–661.